DEPARTAMENTO DE FISICA TEÓRICA Y DEL COSMOS

Universidad de Granada

Kinematics and Star Formation in a sample of Nearby Galaxies

Tesis Doctoral.

Mª Carmen Sánchez Gil.

Directores:

Dr. Emilio J. Alfaro Navarro
Dr. Enrique Pérez

INSTITUTO Ð ASTROFISICA Ð ANDALUCIA - CSIC
enero de 2011

Editor: Editorial de la Universidad de Granada
Autor: Mª Carmen Sánchez Gil
D.L.: GR 2434-2011
ISBN: 978-84-694-2922-8

Agradecimientos

Quiero agradecer a mi familia, y en particular a mis padres, su gran apoyo a lo largo de mi vida y en mis estudios, además de en estos cuatro años de tesis. Sin ellos no habría llegado a estar donde estoy.

Quiero agradecerle a Javi todo su apoyo y ánimos, para que yo siguiera cumpliendo mis sueños, y luchase por ellos.

Agradecerles también a mis directores de tesis, Emilio J. Alfaro Navarro y Enrique Pérez, porque son unos grandes investigadores además de muy buenos directores de tesis. Me han enseñado mucho y me han cuidado mucho también, no hubiese podido tener mejores tutores y me siento muy afortunada y agradecida por ello.

Agradecerles también a esos amigos que nacen de compartir un mismo sueño, un mismo trabajo... por quererme tal y como soy, por ofrecerme su amistad y haber estado ahí cuando lo he necesitado: Antonio, Juande, Mar, Diego, Víctor, Pablo, Geli.

Le dedico esta tesis a mi abuela Isabel.

Contents

Agradecimientos **iii**

Contents **v**

1 Introduction **1**

1.1 Spiral Galaxies and their structural evolution 3

1.1.1 Galaxy classifications 3

1.1.2 Varieties of Spirals 4

1.1.3 Creating a spiral pattern 5

1.2 Star formation in spiral galaxies 7

1.3 Observing star formation 10

1.3.1 Stellar evolution and spectra 12

1.3.2 The Interstellar Medium and the Hα line 15

1.3.3 Determining the recent history of star formation 16

1.3.4 Dust and Attenuation 16

1.4 Corrugations 17

1.5 Thesis Overview 18

2 Kinematical & Physical properties of a 700 pc large bubble in NGC 6946 21

2.1 Introduction 22

2.2 Observations and data reduction 24

2.3 Spectral Analysis: Emission - Line Fitting 28

2.4 Results 29

2.4.1 Kinematics and Geometry: Expanding bubbles 32

2.4.2 Rotation curve of NGC 6946 39

2.4.3 Size of the Hα complex 41

2.4.4 Density profile of the Hα complex 43

2.4.5 Radial expansion velocities: Timescales. 46

2.5 Diagnostic Diagrams 49

2.5.1 Computing the emission line ratios 50

2.6 Summary 51

3 Corrugated velocity pattern in spiral galaxies 57

3.1 Introduction 57

3.2 Galaxy Sample 61

3.2.1 NGC 278 61

3.2.2 NGC 1058 62

3.2.3 UGC 3574 65

3.2.4 NGC 2500 65

3.3 Observations and data reduction 65

3.4 V$_Z$ calculation. Preliminary results. 69

3.5 Diagnostic Diagrams 73
3.6 Summary 78

4 Age Patterns in a sample of spiral galaxies 81

4.1 Introduction 82
4.2 Sample and Data 84
    4.2.1 Galaxy Selection 84
    4.2.2 Data Reduction 85
    4.2.3 Age Calibration 89
4.3 Age Maps 92
    4.3.1 M74 (NGC 628) 94
    4.3.2 IC 2574 96
    4.3.3 M100 (NGC 4321) 97
    4.3.4 M94 (NGC 4736) 98
    4.3.5 M63 (NGC 5055) 100
    4.3.6 M51 (NGC 5194) 102
4.4 Reliability and Robustness 103
    4.4.1 Lowest Threshold Pixel Mass for a Fully Sampled IMF 104
    4.4.2 Spatial Binning Scale 105
    4.4.3 Metallicity and IMF Variation 107
4.5 Discussion and Summary 108

5 Reddening analysis 115

5.1 Introduction 115

5.2 Dust extinction 116

5.3 Using empirical relations 119

5.3.1 FUV extinction factor: A_{FUV} 120

5.3.2 Hα extinction factor: A(Hα) 121

5.3.3 A(Hα) versus A_{FUV} relation. 121

5.4 Using an extinction law 126

5.5 IRX-β relation 135

6 General Conclusions and Future perspectives. 141

6.1 Summary 141

6.2 Conclusiones 145

Bibliography 149

calc ++

1

Introduction

"La observación, no la vejez, trae la sabiduría."

Publio Sirio.

Contents

1.1 Spiral Galaxies and their structural evolution 3
  1.1.1 Galaxy classifications 3
  1.1.2 Varieties of Spirals 4
  1.1.3 Creating a spiral pattern 5
1.2 Star formation in spiral galaxies 7
1.3 Observing star formation 10
  1.3.1 Stellar evolution and spectra 12
  1.3.2 The Interstellar Medium and the Hα line 15
  1.3.3 Determining the recent history of star formation 16
  1.3.4 Dust and Attenuation 16
1.4 Corrugations 17
1.5 Thesis Overview 18

Las galaxias son grandes concentraciones de gas y estrellas ligadas gravitacionalmente, donde tiene lugar el proceso fundamental de la Astrofísica: el nacimiento, la evolución y muerte de las estrellas. Así pues, la estructura de estos objetos está principalmente controlada por el "feedback" (o retroalimentación) entre los procesos de formación estelar a gran escala y la dinámica galáctica.

Entre la dinámica de la galaxia y su estructura morfológica del gas, o patrones de la formación estelar, existe una relación de feedback. La dinámica galáctica redistribuyendo el potencial gravitacional del gas, y éste a su vez al cambiar afecta la dinámica del gas.

En esta tesis intentamos estudiar las relaciones existentes entre los mecanismos de la formación estelar y las estructuras tanto espaciales como cinemáticas de los discos galácticos. En particular nos centraremos en las galaxias espirales cercanas, las cuales muestran su característica estructura espiral - tan compleja como llamativa - y que están íntimamente conectadas con la creación de sus componentes estelares.

La mayoría de las galaxias son tan lejanas que aparecen casi como fuentes puntuales, por lo que muchos estudios anteriores se han ocupado de medir las tasas globales de formación estelar integrando la luz de todo el disco galáctico. La compresión de la estructura galáctica depende de la información proveniente de galaxias relativamente cercanas, donde sus estructuras son visibles. Algunas poseen una resolución suficiente como para poder realizar estudios de la variación con el radio, o distancia al centro galáctico, de propiedades estelares. Estudios de galaxias cercanas pueden extrapolarse y ser aplicados a galaxias lejanas, cuya información está bastante limitada. Obviamente dichas galaxias lejanas mostrarán o tendrán algunas propiedades distintas respecto a las galaxias cercanas, cosa que debe ser tenida en cuenta cuando se trate de aplicar resultados de estas últimas a las primeras.

Además, dentro de las galaxias tenemos que a escalas inferiores del orden del kiloparsec la distribución espacial de la formación estelar está dominada por la estructura del gas donde se ha generado. Mientras que a mayores escalas es el potencial gravitatorio de la galaxia quien domina la distribución de la formación estelar (Sánchez et al. 2010).

Por tanto, intentaremos analizar los siguientes aspectos y escalas: Patrones temporales y espaciales de formación estelar en complejos estelares, estructuras espacio-temporales de formación estelar en discos de galaxias espirales, y patrones de velocidad vertical en brazos espirales de una muestra de galaxias espirales.

Estudiamos por un lado a menores escalas los complejos estelares, en el Capítulo 2, y por otro a mayores escalas los patrones de la formación estelar en brazos espirales, Capítulo 4, y el campo de velocidades del gas a través de los discos de galaxias espirales, Capítulo 3.

Para la realización de esta tesis se han obtenido y utilizado datos espectroscópicos y fotométricos, provenientes tanto del William Herschel Telescope, en el Observatorio del Roque de los Muchachos, en La Palma, como datos de archivo del SPITZER y GALEX. Estos datos abarcan un amplio rango de longitudes de onda (el óptico, el ultravioleta y el infrarrojo), cubriendo el rango espectral desde los 1000 Åaproximadamente hasta las 160 micras. Además de presentar diferentes resoluciones espectrales.

1.1 Spiral Galaxies and their structural evolution

1.1.1 Galaxy classifications

Galaxies come in different flavours: spiral, elliptical and irregular, and there are several morphological classifications within these.

A *spiral* galaxy is relatively gas-rich and consists of a bright central bulge, a stellar disk, a baryonic halo and a halo of dark (non-luminous) matter. The stellar disk can be made up of a thick and a thin disk, with the thick disk extending beyond the thin both radially and in height. The two distinct regions have been clearly in our own Milky Way, a spiral itself. The thin disk is where most of the star formation occurs - within the spiral arms of gas and dust. It therefore contains younger stars which are richer in heavier elements and known as Population I. The central stellar bulge and the thick disk contain older generation Population II stars. The spherical baryonic halo contains minimal gas and globular clusters, each of which are spherical structures containing Population II stars. Globular clusters have masses of the order of $\sim 10^5\ M_\odot$ ($1M_\odot$ denotes one solar mass: 1.989×10^{33}g), although they are known to range from $\sim 10^3\ M_\odot$ to $5 \sim 10^6\ M_\odot$ (Meylan & Heggie, 1997). The dark halo is a recent addition to the picture of galaxies; its presence was revealed from the observed rotation curve (the graph of rotational velocities of neutral hydrogen clouds against radial distance from the galactic centre). The dark halo does not radiate, it exhibits a gravitational presence only, but extends far beyond the baryonic halo and contains the majority of the mass of the galaxy. Spiral galaxies typically have masses of the order of $10^{11}\ M_\odot$ (Salaris & Cassisi, 2005).

Elliptical galaxies, appropriately named, are elliptical in shape and resemble the nuclei of spirals. They contain gas and Population II stars, but little or no dust or young stars. Ellipticals are also classified by size and the range from dwarf to giant ellipticals with masses ranging from $\sim 10^5\ M_\odot$ to $\sim 10^{12}\ M_\odot$ (Salaris & Cassisi, 2005).

The morphological bridge between elliptical and spiral classification is the *lenticular* galaxy. Lenticular galaxies are described as either elongated ellipticals, or disk galaxies without spiral arms. *Irregular* galaxies have no apparent structure or symmetry and are relatively faint.

Active galaxies are galaxies which show strong non-thermal emission over a wide of wavelengths. The properties of their emission lend themselves to interpretation as due to the accretion of matter onto a black-hole. Some examples of active galaxies are radio-loud galaxies, Seyfert I and II galaxies, and quasars which are classified by their orientation to our line of sight. *Starburst* galaxies are mildly active galaxies in which star formation is taking place at an extremely high rate. This is a temporary phenomena as continued star formation at typical rates would exhaust the available reservoir of gas in much less than the age of the universe (a.k.a. the Hubble time) (Leitherer et al. 1995). Starbursts and active galactic nuclei (AGN) are often the result of an interaction between two galaxies.

This study is concerned with the disk (non-nuclear) regions of majority normal (non-starburst) spiral galaxies only and the formation that takes place within.

1.1.2 Varieties of Spirals

Spiral galaxies themselves come in different varieties. The most photogenic of these - the *grand-desing* spirals - have two long, well-defined spiral arms traced out by young bright stars. The arms are symmetric and long-lived. *Multiple arm* galaxies, as their name suggests, have many spiral arms and arm segments (spurs) although the arms are symmetrical in the inner disk. Finally, *flocculent* spiral galaxies have more chaotically distributed short arms.

Spiral galaxies can be described as early - or late - type galaxies. Early-type galaxies have a large bulge-to-disk ratio and have tightly wound arms, while late-type spirals have smaller bulge-to-disk ratio and the arms are looser.

About a third of all spiral galaxies are *barred spirals*, which have a bar-like structure around the bulge, made up of bright stars. The spiral arms extend out from the ends of the bars, where in normal spirals they would extend from the nucleus. The bars are thought to be recurring but temporary phenomena, appearing and decaying over the lifetime of the spiral galaxy. The characteristics used to classify normal spiral galaxies (e.g. early- or late-type) can also be applied to barred-spirals. Bar can trigger star formation in the nuclear regions of the galaxy, but do not appear to significantly affect the total star formation rate (SFR) in the disks (Kennicutt, 1998). Studies by Rozas et al. (1998) reveal a greater symmetry in the spiral arms of non-barred galaxies than barred galaxies. Similarly, studies by Knapen (1993) of the barred-spiral galaxy NGC4321 find an absence of a symmetric pattern in massive star formation efficiency (MSFE) which he suggests may be related to the presence of a bar.

1.1.3 Creating a spiral pattern

The driving forces that create these magnificent stellar spiral patterns have long been an object of study. However there is not a widely accepted theory to account for the graceful spiral patterns in disk galaxies, despite many decades of effort. Earlier theories that the spiral shape arose from the differential rotation of the galaxy had severe difficulties. The speed of the rotation would suggest that arms would wind up much more tightly than what was observed (Pikel'Ner, 1965).

Today, the most commonly accepted explanations involve density waves which triggered and maintained by mutual gravitational interactions of stars in the disk (Byrd, 1984). The waves begin as instabilities (Elmegreen, 1994; Vogel et al. 1988) that pass a critical threshold (Kennicut, 1989) and then sweep through the galaxy. However, there are two distinct theories for the different resulting spirals. The more steady, symmetric spiral arms are due to spiral wavemodes perturbations from a bar or a companion galaxy. When gas rotating around the galaxy centre moves faster than the arm, it slows down upon reaching the crest of the wave and moves radially outwards. The gas collapses in the crest, streaming out along the arm, so that stellar complexes from spaced out along the arm. Multiple arms are generated by local instabilities which evolve into large spiral waves. The resulting large scale star formation can vary from galaxy to galaxy (Elmegreen, 1994).

This more generally accepted explanation, that spiral patterns are gravitationally driven variations in surface density in the old stellar disk, is supported by photometric data (e.g. Zibetti et al. 2009) and streaming motions in high spatial resolution velocity maps (e.g. Shetty et al. 2007). There is also a general agreement that gas seems to be essential. A large fraction of spiral patterns may be accounted as been tidally driven, or the driven responses to bars, specially if orbiting dark matter clumps can excite patterns (Dubinski et al. 2008). But spirals can still develop in the absence of either trigger, as revealed in simulations.

Sellwood (2010), as well as summarize the current theories trying to explain the formation of the spiral patterns, focus on the idea that spirals are self-excited oscillations of the stellar disks, representing a great theoretical challenge.

There are two main, quite distinct, theories to explain the spiral patterns: global modes of rotationally-supported disks and recurrent transients. One idea (e.g. Bertin & Lin 1996) is that spiral features are manifestations of quasi-steady global modes of the underlying disk. Simple models of disk galaxies support many linear instabilities (e.g. Korchagin et al. 2005, Jalali 2007). The bar-forming mode is generally the fastest growing, but it has almost no spirality. These studies are therefore important to understand stability, but do not appear promising for spiral generation. The density wave theory for spiral modes, described in detail by Bertin & Lin (1996), invokes a more specific galaxy model with cool outer disk and hot inner disk. They find slowly evolving spiral modes, and they invoke shocks in the gas to limit the amplitude of the slowly growing mode, leading to a quasi-steady global spiral pattern.

The another idea is that the spiral arms are short-lived, recurrent transient patterns that originate either from shearing bits and pieces (e.g. Toomre 1990), or something more subtle (e.g Sellwood 2000). N-body simulations of cool, shearing disks always exhibit recurrent transient spiral activity, and this basic result has not changed for several decades as numerical quality has improved. Globally stable N-body simulations have manifested recurrent transient spiral patterns for many years, and the phenomenon has not changed as numerical quality has risen. The transient nature of spiral patterns receives indirect support both from the importance of the gas and secular heating of disks.

A serious barrier to progress in this area has been the absence of observational discriminants that would favor one of these radically differing viewpoints over the other. The predictions for density variations or gas responses at a single instant are essentially independent of the generating mechanism and do not depend strongly on the lifetime of the pattern.

It now seems clear that linear theory cannot yield a full description for the development of spiral patterns because N-body simulations suggest that non-linear effects manifest themselves at the relative overdensity of $\sim 2\%$, which is well below the believed spiral amplitudes in galaxies. Real galaxy disks, which contain both star clusters and molecular clouds, are not that smooth. Sellwood (2010) shows how non-linear effects could lead to a recurrent cycle of spirals, although the exact mechanism remains obscure.

1.2 Star formation in spiral galaxies

How and why do stars form in the spiral arms of these types of galaxies? There are most likely several mechanisms; one explanation, particularly for large scale star formation, is that the spiral structure is caused by gravitational instabilities, or *density waves*, within the galactic disk (Vogel et al., 1988; Elmegreen, 1994). As gas and dust in the stellar disk rotate about the galactic centre, the density waves sweep through the galaxy. Giant molecular clouds are concentrated at the wave crests, decreasing the speed of the gas and dust. The gas and dust concentrations eventually collapse to form stars, and pass through the crest of the density wave, forming the well-known visible spiral arms (Vogel et al., 1988). Interestingly, Kennicutt (1989) suggests that, in some cases, the SF may not be triggered by density waves, but may be dependent on the density of gas throughout the disk.

The galactic disk undergoes differential rotation: the stars closer to the galactic centre are moving faster than those at a greater distance. This shearing effect would destroy the spiral pattern of the galaxy, but the density waves actually stabilize the spiral structure.

Star formation in a galactic environment is controlled by physical conditions which vary over the galaxy's lifetime. The global star formation rate (SFR) in normal spiral galaxies has been found reach up to $\sim 20M_\odot\,\mathrm{yr}^{-1}$, while in starburst galaxies it can reach $\sim 1000M_\odot\,\mathrm{yr}^{-1}$. Much work is still being done in understanding what physical processes affect the star formation rate and the distribution of different stellar populations. Theories that describe star formation in spiral galaxy disks must incorporate a number of key physical factors that each have influence on star formation over the lifetime of the galaxy. These factors include gas density, metallicity, star formation history and the initial mass function (IMF) as described below.

Kennicutt (1998) took a sample of 61 normal disk, spiral galaxies and showed correlation between SFR and gas density that is largely independent of galaxy type (early or late type). The gas surface density is found to be the primary determinant of the disk SFR (star formation in the disk as opposed to the nucleus) as the *Schmidt law* (Schimdt, 1959), given below, suggested.

$$\frac{d\sigma_*}{dt} = A\sigma_g^m \tag{1.1}$$

where A is a constant, σ_g is the gas surface density and σ_* is stellar mass. m is some constant power law index.

Dopita & Ryder (1994) fit observations of nearby spiral galaxies to an adaptation of the Schmidt law that predicts the SFR based on both the total matter surface density and the gas surface density, and is applicable to present-day spiral galaxies. The form of this adaptation is given in the equation below. They describe findings that support a model in which star formation is controlled by local rather than global mechanisms.

$$\frac{d\sigma_*}{dt} = A'\sigma_T^n\sigma_g^m \tag{1.2}$$

where A' is a constant, σ_T is the total local matter surface density and σ_g and σ_* are as before. n and m are constant power law indices.

The gas density is altered by the movement of matter on various scales. Small scale disturbances occur through stellar winds; supernovae shock waves are an intermediate scale process, and galaxy mergers and spiral density waves provide larger scale movement. Spiral density waves govern the distribution of dense gas clouds, and therefore, of star forming regions in spiral disks. However, they do not affect the total SFR (Dopita & Ryder,1994). While we see clear evidence of star formation being constrained to the spiral arms, further structural information requires study of spatially resolved galaxies.

Metallicity is a term used to describe the concentration of elements heavier than helium, which in this context are referred to as metals. Stars fuse lighter elements to synthesize metals in their cores over the course of their life. The metallicity of the interstellar medium (ISM) is thus increased by the feedback of those elements through supernova explosions. Distant galaxies were formed at a time when few stars had completed their evolution and returned metallic elements to the gas reservoir. Their stars have low metallicities as a result, and this can be seen in their spectra. Nearby galaxies are observed at a more recent epoch, at a later stage of their life. Many generations of stars have lived and died and metallicity has increased over this time.

The star formation history (SFH) is the evolution of the SFR over the lifetime of the galaxy. Earlier star formation affects the availability of gas for further star formation. Low-mass stars 'lock up' gas for almost the entire lifetime of the galaxy, as do the remnants of high-mass stars (neutron stars & black holes) (Dopita & Ryder,1994). This gas is never released for further star formation.

In studies of star formation history, it is appropriate to assume the global SFR to be constant over time scales longer than $\sim 10^8$ yrs (Kennicutt, 1998). Temporary bursts of star formation (starbursts) by definition increase the star formation rate initially but models of normal spiral galaxies by Iglesias-Páramo et al. (2004) suggest that SFR returns to the original value (that expected for a normal galaxy) after $\sim 10^8$ yrs.

The IMF refers to the populations of stars over a range of stellar masses in a new star forming region. The types of stars present during a galaxy's youth can largely determine its evolution. As we've seen above, present stars can determine how much gas is available for star formation and the density of gas in the future. The IMF is a power law described by parameters such as the power law index α and the upper and lower mass cutoffs. These correspond to the highest and lowest mass stars, respectively, that are present. Evolutionary synthesis models are used to estimate the populations that emit the observed integrated spectra. They generate the spectra emitted by different stellar populations as they evolve.

Upon comparison to observed spectra, various properties such as the ages and masses of star-forming regions can be determined. This study uses one particular model, *Starburst99*, created by Leitherer et al. (1999), to determine the ages of star forming regions.

The SFR in spiral galaxy disks has a strong dependence on the mass of the galaxy therefore it is more useful to consider SFR per unit mass. It also has a strong dependence on morphological type and redshift (a measure of distance and therefore the age at which we are observing the galaxy). There is a moderate dependence on (galaxy-galaxy) tidal interactions with companion galaxies, moderate/weak dependance on cluster environment, and weak dependence if any, on the bar and spiral structure (Kennicutt, 1998). No significant difference has been found in the SFR between grand design spirals and flocculent spirals (Elmegreen & Elmegreen, 1986; McCall & Schimdt, 1986). It is important to note that the SFR in the disks is largely decoupled from the SFR in the circumnuclear regions (bulge) of the galaxies (Kennicutt, 1998).

The study of star formation (SF) and star formation rates (SFR) in galaxies provides vital information regarding galactic evolution. The variation in SF activity across the different types of galaxies is influenced by many factors, including gas content, mass and dynamical environment (Kennicutt, 1998). Trends in SFRs and SF histories across galaxy types allow for predictions of galactic evolution with cosmic lookback time.

1.3 Observing star formation

If very hot, massive stars (T$>10^4$K, M$\sim 3-120\ M_\odot$; Allen 1973) are produced, the UV light they emit is energetic enough to ionize the surrounding gas (mostly hydrogen), which, when recombined, produces optical emission (e.g. the Balmer lines Hα, Hβ, etc). Less massive stars (e.g. A stars: T$\sim 7500-10000$ K, M$\sim 1.5-3\ M_\odot$; Allen 1973) also produce UV emission, but this radiation is not energetic enough to ionize the gas, so Balmer emission is not detected (optical continuum is of course emitted from OB and A stars). Hence, UV and Hα are useful as direct tracers of massive star formation.

Individual stars are only resolved in the closest galaxies, so global SF properties of galaxies are mostly obtained by integrated light measurements. The most common diagnostic methods use measurements in the ultraviolet (UV), far-infrared (FIR), or nebular recombination lines (Kennicutt, 1998). Of particular interest for this thesis are measurements in the UV and the Hα recombination line (656.3 nm).

SF studies using UV, particularly in the wavelength range 1250-2500 Å, provide information on the young stellar population (O,B, A stars). Ground-based observations cannot be performed over this wavelength range for galaxies with redshifts $z < 0.5$. However, this spectral range is observable at optical wavelengths for high redshift galaxies ($z \sim 1 - 5$) (Kennicutt, 1998). Telescopes outside the Earth's atmosphere (e.g. the Ultraviolet Imaging Telescope; Stecher et al. 1992, 1997) are able to observe nearby objects at 1250-2500 Å. UV emission, however, is extremely sensitive to dust extinction, and correcting for this effect can be difficult.

Recombination lines are emitted from gas ionized by young, very hot stars. Many different recombination lines have been used in studies of SF, but the most common is the Hα line. This line is strong only in the presence of the most massive, hottest stars (masses$> 10M_{\odot}$, ages< 20 Myr) that have enough energy to ionize the surrounding hydrogen, and so is an ideal probe fro the young stellar population. Hα emission is also affected by dust extinction. Both Hα and UV measurements can be corrected for dust extinction using infra-red (IR) measurements, which are largely unaffected by dust.

Integrated Balmer line emission from a galaxy can be used as a direct probe of its current SF activity. Kennicutt (1983) shows that the present rate of SF in late-type galaxies is comparable to the past rate, averaged over the lifetimes of the galaxy disks, i.e. the SFR is relatively constant over the lifetimes of most late-type disk galaxies (see also Searle et al. 1973).

All integrated light measurements are converted to SFRs by use of evolutionary synthesis models of galaxies (Kennicutt, 1998). Such models use summed stellar evolution tracks that are weighted depending on the initial mass function (IMF) used in the model (i.e. the initial distribution of mass in the model). The spectra or colours of the galactic models are synthesised as functions of age, and can be compared with the observed measurements to analyse the SF within galaxies.

The volume averaged SFR of the Universe has emerged as a key quantity of cosmic evolution (Lilly et al., 1996; Madau et al. 1996; Steidel et al. 1998). The concept behind this is to simplify the investigation of stellar history, independent of the statistics of individual galaxies. Despite the appeal of this approach, galaxies are fundamental constituents of SF history studies (Madau et al., 1998). The "Madau plot", which considers the volume-averaged SFR as a function of redshift, uses galactic UV emission as a measure of SFR; Glazebrook et al. (1999) include Hα emision in their studies of SF history. Critical to our understanding of galaxy evolution at high redshift is our understanding of the relation between SF, UV and Hα emission in local galaxies.

1.3.1 Stellar evolution and spectra

The greatest influence on a star's evolution is its mass. When a star is born from gravitational collapse of a dense hydrogen gas cloud, it begins by burning hydrogen into helium in its core. This is the longest evolutionary phase, during which the star is known as a *Main Sequence* star. The main sequence corresponds to a curve on the *Hertzsprung-Russell diagram* referred to by the abbreviation H-R diagram or HRD, see Figure 1.1[1]. The H-R diagram is a scatter graph of stars showing the relationship between the stars' absolute magnitudes or luminosity versus their spectral types or classifications and effective temperatures, on which each star of a particular mass and age has a given position. This is, The H-R diagram is an extremely useful way to follow the changes that take place as a star evolves. So, most stars are on the Main Sequence because that is where stars spend most of their lives, burning hydrogen to helium through nuclear reactions. Stars are arranged along the main sequence by their masses. At the lower right end of it are the lightest stars, upper left are the heaviest.This phase ends only when this fuel runs out in the core and the star must start to burn hydrogen in a shell surrounding the helium core. At this point, the star expands, with a larger surface area resulting in a higher luminosity. This, along with a drop in surface temperature leads to a change in the star's position on the H-R diagram. The time scale of the initial H-burning phase is determined by the star's mass, with massive stars moving off the main sequence quicker than lower mass stars. Low mass stars can remain on the main sequence for the lifetime of the galaxyin which they are born. Stars are classified by surface temperature, in order of hottest to coolest: O,B,A,F,G,K and M. This classification system also extends further to cooler stars but the ones mentioned are the most basic. For main sequence stars, this classification is also a measure of mass, where O-type main sequence stars are the most massive and the rest are systematically less

---

[1] image credit: *http://www.atlasoftheuniverse.com/hr.html*

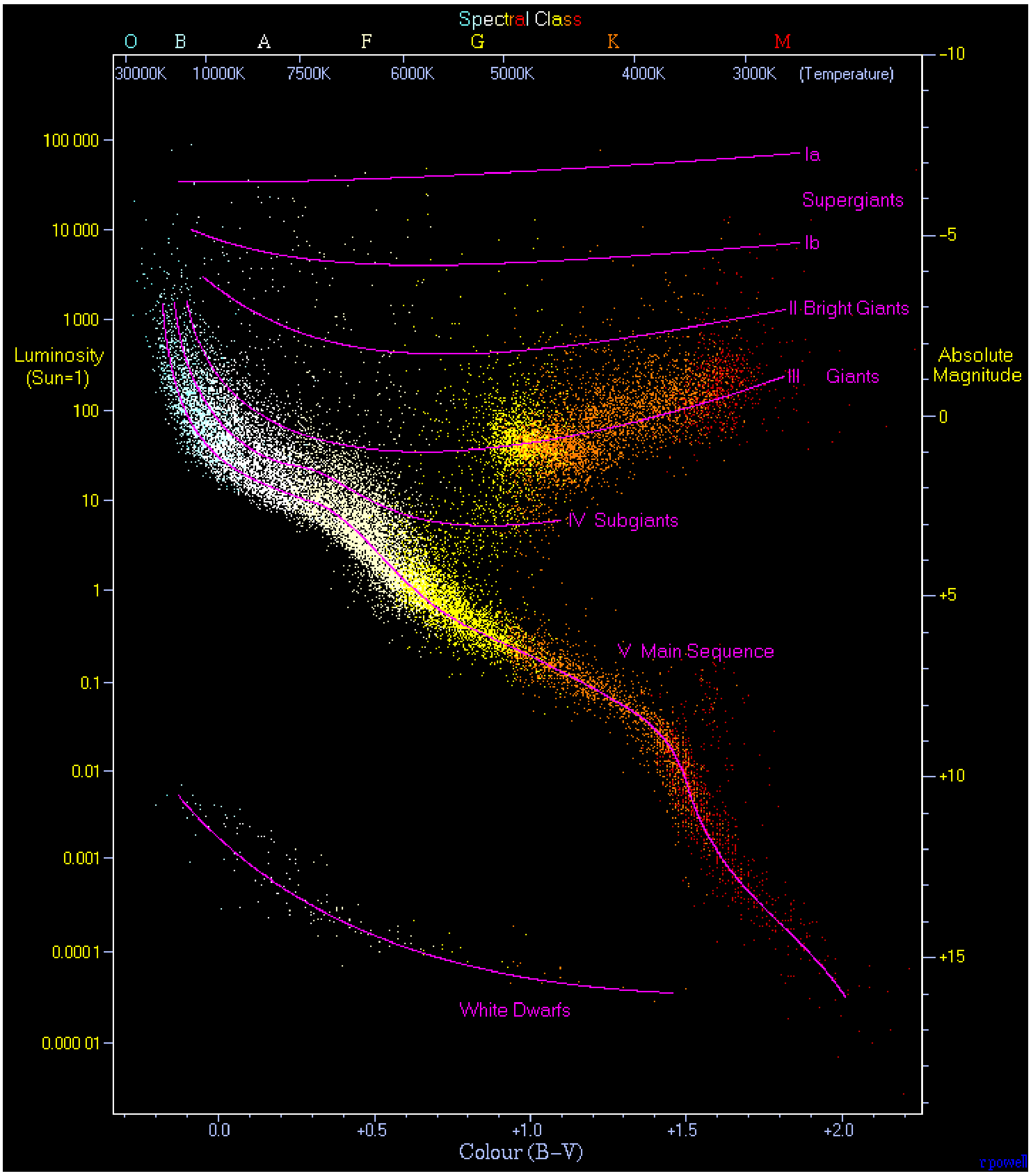

Figure 1.1: Hertzsprung-Russell diagram by Richard Powell (*image credit: http://www.atlasoftheuniverse.com/hr.html*). 22,000 stars are plotted from the Hipparcos catalog and 1,000 from the Gliese catalog of nearby stars. An examination of the diagram shows that stars tend to fall only into certain regions on the diagram. The most predominant is the diagonal, going from the upper-left (hot and bright) to the lower-right (cooler and less bright), called the Main Sequence. In the lower-left is where white dwarfs are found, and above the main sequence are the subgiants, giants and supergiants. The Sun is found on the main sequence at luminosity 1 (absolute magnitude 4.8) and B-V color index 0.66 (temperature 5780K, spectral type G2).

massive. Our Sun is an intermediate size, G-type star, remaining on the main sequence for ~ 10 billion years.

All stars emit a continuous blackbody spectrum (light at all wavelengths) called a *Planck curve* with a single peak at a particular wavelength which depends on the temperature of the star's atmosphere, according to *Wien's law*:

$$\lambda_{peak}T = 2.897 \times 10^{-3} mK \tag{1.3}$$

The surface temperatures of main sequence stars are ultimately dependent on their mass, and therefore higher mass main sequence stars peak in intensity shorter (bluer) wavelengths, or higher frequencies and energies, than lower mass main sequence stars. These massive stars also exhibit a greater total flux over all wavelengths. The mass of the star thus determines not only its evolution but also the properties of the light it emits during its lifetime.

Some of the stars in a galaxy are in other phases, having moved off the main sequence. Short-lived red giants and supergiants are the later phases of intermediate and massive stars respectively, neutron stars and black holes are the remnants of massive stars and white dwarfs are the remnants of intermediate mass stars.

In spiral galaxies, which contain many young bright stars, these phases contribute little to the overall observed spectra. While intense radiation at short wavelengths might possibly be the result of a large number of intermediate mass stars, the peaks of stellar spectra are so steep that it is much more likely that the emission indicates the presence of much fewer high mass stars. This is the basis of interpretations of observed radiation.

When we observe stars, the light we see is not just that which is directly emitted by the star. The material that lies within our line of sight obstructs stellar light by absorbing and radiating. To correctly interpret what is observed, we must first consider what might happen to stellar light before it reaches us.

1.3.2 The Interstellar Medium and the Hα line

The interstellar medium (ISM) is a diffuse mixture of gas and dust that surrounds stars and permeates the enormous spaces between both stars and galaxies. The gas is 90% hydrogen and 10% helium with traces of heavier elements (Salaris & Cassisi, 2005). The ISM has a density that ranges from 10^{-3} to 10 particles/cm^3, compared to the molecular hydrogen gas clouds where stars form which have densities of 10 to 10^2 particles/cm^3 (Salaris & Cassisi, 2005).

Hydrogen gas makes up the bulk of the ISM. It can be ionized to form an HII region (singly ionized hydrogen) by photons at energies of 13.6 eV, which free ground state electrons. This corresponds to a wavelength of 912Å. *Lymann continuum photons* are those shortward of 912Åand are required to ionise the hydrogen gas.

The ionized gas exhibits emission lines upon recombination of free electrons and protons, as the electrons cascade down to lower energy levels. The hydrogen *Balmer series* is the set of lines emitted when electrons drop to n=2 from higher energy level. The Hα Balmer line, emitted during the 3→2 level transition, is at the optical wavelength 656.3 nm (6563Å). Other Balmer lines like Hβ (4→2 level transition at 486 nm) are emitted as well, but the Hα transition is the most common transition during recombination. *Case B* recombination states that all Lyman series photons (emitted upon transitions to n=1) are re-absorbed by *other hydrogen atoms*, an optically thick approximation (Osterbrock & Ferland, 2006). In this scenario, 0.45 Hα photons are emitted for each ionizing photon absorbed by the HI gas (neutral hydrogen).

As mentioned in the previous section, small numbers of massive stars peak at shorter wavelengths, and dominate short wavelength radiation. Ionizing Lyman continuum photons are dominated by emission from massive O-type stars with $M > 10M_{\odot}$ (Iglesias-Páramo et al., 2004; Dopita & Ryder, 1994; Kennicutt, 1998). The ionization is ultimately responsible for the Hα emission, so the Hα line is a tracer for these stars.

Other UV wavelengths are also observed in studies of star formation. At the near-UV (NUV) wavelength of 2000Å, significant amounts of radiation comes from stars with $M > 1.5M_{\odot}$ (Iglesias-Páramo et al., 2004). The integrated UV spectrum between 1500 and 2500Åis dominated by high mass $M \gtrsim 5M_{\odot}$ OB-type stars (Kennicutt, 1998).

1.3.3 Determining the recent history of star formation

The UV-dominating O-B type stars have lifetimes $\lesssim 10^8$ yrs (Iglesias-Páramo et al., 2004; Kennicutt, 1998). The UV thus indicates star formation over the last $\sim 10^8$ yrs. Meanwhile, the O-type stars that contribute significantly to the ionizing flux have even shorter lifetimes as they quickly evolve to red supergiants or erupt as supernovae. Their lifetimes are estimated at $\lesssim 10^7$ yrs by Iglesias-Páramo et al. (2004), or $\lesssim 2 \times 10^7$ yrs by Kennicutt (1998). The Hα emission line is a result of ionization due to fluxes from these stars, so this wavelength traces 'instantaneous' massive star formation no more than 20 Myrs ago.

A comparison of UV and Hα fluxes would give a good indication of recent star formation history. Emission at particular wavelengths reduce as their progenitor stellar types die out. As a new star forming region evolves, the Hα line emission declines before the UV emission does, leading to a decrease in the ratio of Hα line emission to UV flux. This flux ratio is very sensitive to the age of a new star forming region. Over the long term however, it would stabilize as even the UV-dominating O-B type stars have moved off the main sequence.

Normal spiral galaxy models by Iglesias-Páramo et al. (2004) show that the Hα-to-UV flux ratio when integrated over the entire disk stabilizes for galaxies with ages $\geq 10^9$ yrs since the epoch of galaxy formation. This corresponds to galaxies with redshift (distance) of $z \lesssim 7 - 10$. So the flux ratio integrated over the galactic disk will be constant for the nearby galaxies in this study. However, there will be much spatial variation due to the varying ages of individual star forming regions across the disk. The conversion from observed UV and Hα fluxes to a recent star formation history based on intrinsic fluxes requires an understanding of the effects of ISM opacity and dust on the observed fluxes.

1.3.4 Dust and Attenuation

The Lyman continuum photons that do not encounter the hydrogen gas component of the ISM can be then scattered by dust. While gas consists of atoms, molecules and ions, dust contains small particulate matter made of various kinds of ices, graphite, silicates and possibly metals (Mihalas & Binney, 1981; Salaris & Cassisi, 2005). The collective effect of the gas and dust on the radiation is known as *extinction*.

Dust attenuates all radiation but its effect is wavelength dependent, with shorter (bluer) wavelengths being more susceptible to scattering by dust. It absorbs shorter wavelengths and re-emits at longer wavelengths, creating a net 'reddening' effect. UV wavelengths are shorter than the Hα line, so dust scattering will shift the Hα-to-UV flux ratio (Iglesias-Páramo et al. 2004), and alter the resulting SFR estimate. UV dust extinction should be independent of metallicity, according to Iglesias-Páramo et al. (2004), and should therefore affect all galaxies similarly. In some galaxies (M83 and M101), extinction has been shown to be a strongly declining function of radius (Martin et al., 2005). Infrared (IR) measurements are much less affected by dust and so can be used to calibrate the SFR.

1.4 Corrugations

Gas and stars in the Milky Way show quasi-periodic vertical deviations from the formal galactic plane. This kind of pattern, so named corrugations, seems to be a general phenomenon affecting the disk galaxies. Recent studies, both theoretical and observational, have shown that similar structures might appear in the field of the velocity vertical component and could be derived from the radial velocity maps on face-on galaxies. The mechanisms which generate these spatial patterns are connected with those able to arrange the gas and form the large fertile clouds where stars will born. Different proposed models for the generation of corrugations anticipate distinct velocity fields providing a good observational test to these mechanisms.

While studying the galactic distribution of HI in order to define a more precise galactic coordinate system, Kerr (1957) and Gum et al. (1960)

The young stellar component and gas of the Galactic disk show systematic displacements from the formal galactic plane. In the inner regions of our Galaxy the so called corrugations appear to dominate the vertical structure of the galactic disk. This phenomenon, which could be defined as a residual wavy structure with respect to the defined mean plane (Gum, Kerr, & Westerhout 1960; Lopckman 1977; Spicker & Feitzinger 1986; Alfaro, Cabrera-Caño, & Delgado 1992a), has been observed throughout the different spiral arms and galactocentric radial directions (Spicker & Feitzinger 1986; Malhotra & Rhoads 1995).

This phenomenology has also been observed in other galaxies (Florido et al. 1991), which would seem to indicate the universality of these kind of structures. Infrared studies appear to indicate that old stars show similar displacements to those found in the young galactic component, which in turn suggests that they might be of gravitational origin (Djorgovski & Sosin 1989; Rhoads 1995). The amplitude and scale of the corrugations show a wide range of values (50-150 pc in amplitude and 1-13 kpc in scale), depending as much on the spiral arm as on the different spiral tracers chosen for their study (Spicker & Feitzinger 1986; Florido et al. 1991).

Besides these large-scale features, the interstellar medium also shows local deviations from the formal plane, referred to in the literature as chimneys, bubbles, holes and worms (Heiles 1984, 1989; Li & Ikeuchi 1990). These structures seem to arise from local star-gas interactions and show no large-scale patterns.

The gas and young stellar population used in most of these studies also provide the observational basis for studying star-formation processes and for determining the locations and scales of the star-formation regions in our Galaxy and others (e.g., Efremov 1978; Efremov & Sitnik 1988; Elmegreen & Elmegreen 1983). Star formation seems to occur on all scales with a hierarchic pattern generated and controlled by self gravity and turbulence (Elmegreen & Elmegreen 1996). Only in galaxies with strong density waves does the gas become structured by regular forces, and supercomplexes appear as the dominant, largest scale of star formation. Our Galaxy provides us with several examples of large-scale star-formation regions. In grand-design spiral arms, such as Carina-Sagittarius, the density waves seem to control the pattern of star formation, leading to the generation of typical supercomplexes arranged along the whole arm, whereas the Orion-Cygnus arm could have been generated by the balance between turbulence and shear.

1.5 Thesis Overview

This thesis concentrates on the study of the star formation, at different scales. We study the star formation in star complexes, at local scales of SF, as well as the SF across the galactic disks triggered by large scales processes as density waves.

This first chapter introduces some of the scientific background regarding spiral galaxies and star formation studies. Chapter 2 studies the case of a peculiar stellar complex, located at the end of one of the spiral arms of NGC 6946. This gas-star complex of 700 pc in diameter which appears populated by tens of young stellar clusters, and a Super Star Cluster (SSC) as massive as 10^6 M$\odot$. The ionized gas, as drawn by the Hα emission, delineates an almost circular shape which we show here to be in expansion. Previous studies have analyzed the stellar component of the complex, as well as the structure of the atomic and ionized gas; these analyses were restricted to the blueshifted component along the whole extent of the bubble or to a smaller inner region where both sides of an expanding bubble were seen. In this work we present a complete spectroscopic study of this object for two position angles crossing each other close to the young massive SSC. We have obtained new data with a spectral resolution six times better than previous spectroscopic studies, taken under atmospheric conditions better than those previously reported, allowing us to detect the approaching and receding walls of one the largest bubbles in external galaxies ever studied in detail.

The kinematical analysis shows a large expanding bubble, whose walls appear to be highly structured with superposed smaller shells, likely originated as the result of star forming events occurring at the edges of the larger scale shell, a la Huygens. We also study some diagnostic diagrams of the ionized gas and conclude that most of the observed ionization is originated by photons from hot stars, but with clear evidence that some of the gas is shock ionized.

This peculiar complex is an excellent laboratory for the analysis of the interaction and feedback between the gas where the stars were formed and the young and massive generation of new born stars.

In chapter 3 we present the preliminary results from the study of the corrugations, described above in Section 1.4, for a sample of four mostly nearby and nearly face-on spiral galaxies. We find that two of these galaxies, NGC 278 and NGC 1058, clearly show the same kinematical behaviour than that found by Alfaro *et al.* (2001) in NGC 5427, and similar to the one expected in a galactic bore generated by the interaction of a spiral density wave with a thick gaseous disk (Martos & Cox 1998).

In Chapter 4 we present the results of comparing optical observations at Hα emission line, taken with Taurus Tunable Filter (TTF), with UV GALEX images of a sample of nearby (distance $<$ 10 Mpc) spiral galaxies. We explore a new approach for connecting large-scale dynamical mechanisms with star formation processes in disk galaxies, based on deriving burst ages for young stellar populations in spatially resolved, spiral galaxies. The study is performed using a pixel by pixel differential analysis of the ionized gas emission in respect to the stellar far-UV ionizing radiation. The resulting flux ratio is calibrated in term of age by using galactic evolution models and discussed in the light of the large-scale dynamical motions in the disk.

Uncertainties in the Hα to FUV flux ratio, that can be affected by many physical causes such as variable IMF, non-solar metallicities, non-constant SFHs or SFR, dust attenuation, etc (e.g. Iglesias-Páramo *et al.* 2004, Meurer *et al.* 2009, Lee *et al.* 2009), are taken into account. Moreover, the simplified parameters used by galactic evolution models are only examples for basic spiral galaxy evolution, without taking into account such parameters as perturbing objects. Therefore we use these models as a guideline to indicate the relative ages of the stellar populations in the spiral arms. Anyway, this work shows that a comparison of the Hα and FUV observations of nearby spiral galaxies is a relatively direct way to probe burst age variations in spirals.

The resulting age maps show the pattern of ages across these resolved galaxies, remarking as well their morphology and age gradients across the spiral arms, in many cases, in circumnuclear regions (M94) or in HII complexes (IC 2574). A remarkable result has been obtained for M51, where evidence stellar age gradient along the short dust branches, spurs, has been found.

Chapter 5 presents a deeper and detailed analysis of the resulting reddening correction in the previous Chapter 4. The different approaches done to realize the reddening correction are presented and discussed, as well as the reasons for choosing the applied reddening correction method with IR data.

Moreover, taking advantage of the huge amount of pixels and therefore of data to do robust statistics, we independently derive our own IRX-β relation (Heckman *et al.* 1995, Meurer *et al.* 1999) based on our pixel-by-pixel analysis of the six star forming galaxies in our sample.

The final Chapter 6 contains a brief discussion of the conclusions from this thesis, and some ideas for future work.

2

Kinematical & Physical properties of a 700 pc large bubble in NGC 6946

Contents

2.1 Introduction 22

2.2 Observations and data reduction 24

2.3 Spectral Analysis: Emission - Line Fitting 28

2.4 Results 29

2.4.1 Kinematics and Geometry: Expanding bubbles 32

2.4.2 Rotation curve of NGC 6946 39

2.4.3 Size of the Hα complex 41

2.4.4 Density profile of the Hα complex 43

2.4.5 Radial expansion velocities: Timescales. 46

2.5 Diagnostic Diagrams 49

2.5.1 Computing the emission line ratios 50

2.6 Summary 51

2.1 Introduction

The galaxy NGC 6946 harbors a young star cluster which can be considered as the most massive known cluster within the limits of the Local Volume, its estimated mass being around 10^6 $M_\odot$, (Larsen et al. 2001, 2006). The cluster is not isolated but it appears to occupy the central region of a large stellar complex, $\approx$ 700 pc diameter, which was first reported by Hodge (1967) and lately rediscovered and studied by Larsen & Richtler (1999) in their extensive mapping of young cluster populations in nearby galaxies. Since then, this stellar complex has been extensively studied, both through the stellar population as well as through the gas component.

The complex contains more than a dozen of young clusters with ages ranging between 10 and 30 million years (Elmegreen et al. 2000). A detailed study of the stellar population performed by Larsen et al. (2002) allowed them to derive the star formation history (SFH) of the isolated stellar component, showing a present-day high star formation rate (SFR) and an important decrease of the SFR of isolated stars at the time most of the cluster population was born. It, thus, looks like that most of the star formation, between 10 and 15 Myr ago, took place in the mode of cluster formation, rather than forming isolated stars or loose associations.

The massive cluster has an estimated age of 10-15 Myr, from its integrated photometry, with a luminosity of $M_V = -13.2$ and a mass of 10^6 $M_\odot$ as derived from both luminosity and dynamical criteria (Larsen et al. 2001, 2006). The internal velocity dispersion of its members has been calculated to be close to 9 km s^{-1} (Larsen et al. 2006). All these characteristics suggest this object to be the young evolutionary stage of a classical globular cluster. These massive young objects have been denominated in the recent literature by different names, we adopt here that of super star cluster (SSC).

The ionized gas in the complex has also been the subject of recent studies. Efremov et al. (2002) analyzed long slit spectra, centered on the Hα emission line, and taken with the 6 m BTA and 10 m Keck-I telescopes. The radial velocity curves along the slits show the existence of several dips or bumps superimposed on a smooth curve compatible with the expected velocity rotation of the galaxy at these positions. Particularly, conspicuous is the detection of a steep fall-off in the radial velocity curve along P.A.=83°, centered $7''$ away from the SSC location in the side of lower emission density, with an amplitude larger than 70 km s^{-1}. These authors considered that feature as the signature of an expanding semibubble. Three-dimensional optical spectroscopy was lately performed with the INTEGRAL spectrograph attached to the 4 m William Herschel Telescope (WHT) at Roque de los Muchachos Observatory and with the 6 m BTA telescope at the Special Astrophysics Observatory of the Russian Academy of Science (Alfaro et al. 2007; Alfaro & Elías 2006; Efremov et al. 2007). The main picture emerging from these analyses is that we are facing an Hα torus, around 800 pc in diameter, which draws an almost complete circle, 280° long, while it is open in the northeast side of the torus. In addition, two other Hα features, one associated to the SSC and the other forming an arc-shaped structure, 130° long, located at the northwest of the SSC are also evident. This last feature of Hα emission is also spatially associated to the main concentration of the youngest stars (4-My old) in the complex (see Figure 1 in Larsen et al. 2002)

The atomic gas in the complex still lacks a detailed analysis at the adequate spatial resolution, but a few important results have been derived from some recent works (Boomsma 2007; Boomsma et al. 2008; Efremov et al. 2007). The complex appears to be placed in a region of HI low density, which extends further to the northeast, forming an extensive HI hole a few kpc in size. This is not strange since NGC 6946 is known to be a galaxy with a large number of HI holes and high velocity clouds (HVC) (Kamphuis 1993), some of which have kinetic energies above 10^{53} erg. A look to Figure 14 in Efremov et al. (2007) shows that, at the position of the SSC, the distribution of HI density presents a local minimum for a wide range of gas velocities, and some smaller knots are visible at velocities well below the mean value.

All these features make this region an excellent laboratory for analyzing the interaction and feedback between the gas and the youngest products of the star formation processes, in particular, concerning the small-scale relationship between the interstellar medium (ISM) and the SSC. Good spectral and spatial resolution are thus crucial for determining the main physical properties of the gas along the entire super-bubble and for drawing the true geometry of the complex. Through the data presented here, we attempt to clarify which physical mechanisms could apply in this region of NGC 6946.

The paper is organized into six sections; the first is this introduction. In Section 2, we describe the observations and the primary reduction of the spectra. The analysis of the emission lines is shown in Section 3, and in Sections 4 and 5 we explain and discuss the results obtained. Finally, Section 6 summarizes the main conclusions of this work.

2.2 Observations and data reduction

We obtained long-slit spectroscopy with the double arm ISIS spectrograph attached to the WHT, at the Roque de los Muchachos Observatory (La Palma) during August 2003. This instrument consists of two intermediate dispersion spectrographs operating simultaneously, separating the blue and red spectral regions, which are imaged onto an EEV12 and a MARCONI2 CCD chips, respectively. In this way, we have two spectral ranges observed simultaneously, a blue one centered around Hβ (4861 Å), and a red one around Hα (6563 Å). The gratings used, R1200R and R1200B, provide a dispersion of 0.23 Åpixel^{-1}. The slit width of 1 arcsec projects onto about 3.64 pixels full width half maximum (FWHM) on the detector; the spatial sampling along the slit is 0.2 arcsec pixel^{-1}. The slit was placed at two position angles, 0° and 296°, approximately centered on the shell (Figure 1). In table 2.1, we present a comparison of our observational configuration with previous spectroscopic studies dealing with this object and in table 2.2 the log of the observations.

The spectra were reduced and calibrated following the standard procedure. Bias subtraction, flat-fielding, wavelength and flux calibration were done with the IRAF[1] task `ccdproc`. For the wavelength calibration CuNe and CuAr lamps were used. The standard star Feige 110 from the Oke (1990) catalogue was used for flux calibration. Sky subtraction was done using the IRAF NOAO package task `background`. For each wavelength range, the different exposures at each slit orientation were combined, eliminating cosmic rays and bad pixels, thus obtaining four final spectra.

We use an intermediate band Hα image (central wavelength 657.7 nm and FWHM=18 nm) taken with the Nordic Optical telescope (NOT)[2].

---

[1] IRAF is distributed by the National Optical Astronomy Observatory, which is operated by the Association of Universities for Research in Astronomy, Inc., under cooperative agreement with the National Science Foundation

[2] The image kindly made available by Y. Efremov is taken through a filter called wide 'Hα filter' in the NOT system

Figure 2.1: Gemini Multi-Object Spectrograph (GMOS) image from Gemini North on Mauna Kea, in the bands g', r', i', and Hα (Gemini Observatory/Travis Rector, University of Alaska Anchorage). The image has been adapted, showing the relative position of the complex respect to the galaxy center. The two slit positions, used at this study, are also drawn on the complex. North is up and east to the left.

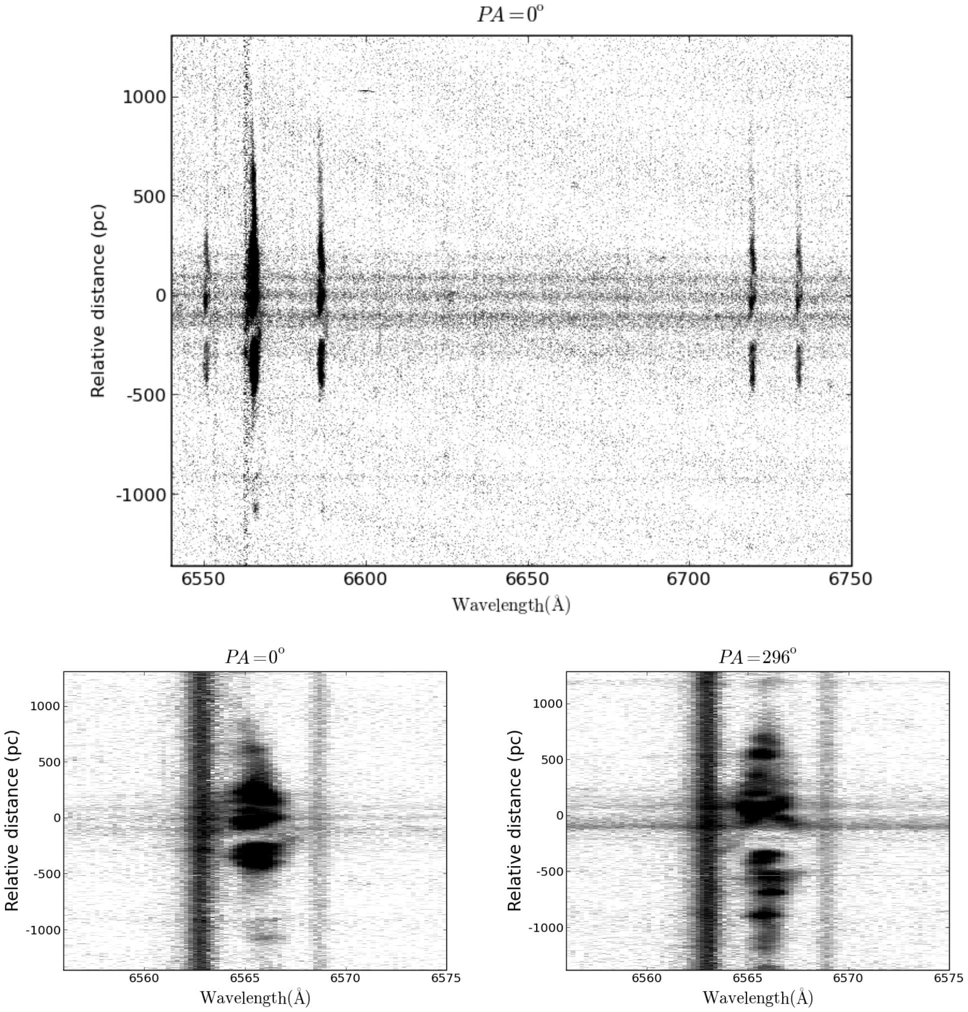

Figure 2.2: Two-dimensional long-slit red spectra, centered at Hα (6562 Å), for both slit positions; relative distance increase toward the north. Top: the sky subtracted red spectrum for P.A. = 0°, showing the Hα (6562 Å), [NII] λ6548, 6584 Å and [SII] λ6716, 6730 Å emission lines. Bottom: red spectra (not sky subtracted) for both slit positions zoomed into Hα show a detailed complex structure of the ionized gas.

Table 2.1: Observational configuration of different spectroscopic studies

Instrument & Detector	Wavelength Range (Å)	Exposure Time (s)	Dispersion (Å/ pixel)	Pixel Scale (″/ pixel)	Seeing (″)
Multi-Pupil Fiber Spectrogragh, 6m BTA[a] CCD EEV42-40 (2048×2048 pixel)	6140 – 7120	3×900	0.76	0.14	1.2, 1.5
6m SAO RAS telescope[b] Photometrics CCD-detector (1024×1024 pixel)	6015 – 7250	1,2×1800	1.2	0.39	1.4,2.7
Keck-I 10m telescope[c] D1 decker (14″× 1″.15 slit)	6220 – 8550	4×3300	0.048	–	0.9
ISIS at William Herschel Telescope MARCONI2 CCD (4096×2048 pixel)	6034 – 7088	3×1800	0.23	0.2	1.0

NOTES.- Values given within the table are only related to Hα range data, for the analysis of the velocity field.

[a] Efremov et al. 2007.

[b] Efremov et al. 2002.

[c] Efremov et al. 2002. But limited to a full extent of 14″along the slit, with a position angle of -10°, close to the SSC location.

Table 2.2: Journal of Observations

Date	P.A. (deg)	Wavelength Range (Å)	Exposure Time (s)	Slit (″)	Airmass
2003 Aug 21	0	6034–7088	2×1800 + 1200	1.0	1.23
2003 Aug 21	296	6034–7088	3×1800	1.0	1.17

2.3 Spectral Analysis: Emission - Line Fitting

The final combined sky subtracted red spectrum at P.A.=0° is shown in Figure 2a, in the spectral range 6540-6750 Å covering the five main emission lines, Hα, [NII]6548,6583, and [SII]6716,6731. Figure 2b shows an expanded view around Hα of the spectrum along P.A.=0°, 296° (not sky subtracted). The origin of the spatial scale has been arbitrarily set to a point close to the shell center (where the two slits intersect). The residuals of the sky subtraction can be seen (in the top panel) along the slit at 6553.5 and 6562.8 Å. Upon close visual inspection, these spectra readily show that the Hα emission is highly structured in velocity along the slit, with a series of components that indicate the presence of shells. In this section, we describe the detailed measurement of these structures with the aim of obtaining the kinematical information along the two slit positions.

We fit the Hα emission line at each pixel along the slit. Line flux, FWHM, central wavelength, and their corresponding errors, are calculated with the STARLINK[3] package DIPSO. The continuum level is simultaneously fitted with a first-order polynomial.

The sky subtracted spectra in Figure 2 (top panel) show residuals in some sky emission lines. Particularly, the atmospheric Hα line is relatively conspicuous and close to the Hα emission in NGC 6946. After some trials we decided to fit the spectra prior to the sky subtraction (bottom panel). The reason is that, at some locations along the slit, there is a faint high velocity blue shifted Hα component very close to the sky Hα emission, and the fitting subroutines work better by fitting an additional component to the sky emission, while the results are worst working with the residual sky emission in the sky subtracted spectra. This method has the additional advantage of obtaining a map of the uniformity of the spectral resolution and quality of the wavelength calibration along the slit, from the fits to the sky emission lines.

Figure 2.3 illustrates two example fits of the slit at P.A.=0°. In the case of the spatial increment 500 along the slit, we fit two components to the Hα nebular emission, and one component to each of the sky emission lines at 6562.8 Å and 6568.9 Å, respectively. The case of the spatial increment 565 along the slit is an example where we could fit three components to the nebular Hα. This extra third component is present only in some locations along the slit, while in most other locations the fit is satisfactory with just two

---

[3] http://star-www.rl.ac.uk/star/docs/sun50.htx/sun50.html

components (inside the stellar complex) or with just a single one (corresponding to the emission outside the complex, see the next section for details). From these fits, we estimate the values for the following variables :

$$V_{obs} = \frac{(\lambda_{obs} - \lambda_0)\, c}{\lambda_0}, \tag{2.1}$$

$$FWHM = W_{obs} \frac{c}{\lambda_0}, \tag{2.2}$$

$$EW = \frac{line\, intensity}{I_c}, \tag{2.3}$$

$$r = (y - y_0)\, 0.2\, \frac{1}{3600}\, \frac{\pi}{180}\, 5.5 \times 10^6, \tag{2.4}$$

where V_{obs} is the line velocity in km s^{-1}, observed from the Earth, c is the velocity of light and $\lambda_0 = 6562.8$ Å the air reference wavelength of the line. Observed velocities were then tied to the heliocentric system. So the velocity of the gas, throughout this paper, refers to the heliocentric velocity. In equation (2.2), $FWHM$ is expressed in km s^{-1}, W_{obs} is the FWHM from the fit. In equation (2.3), EW is the equivalent width and I_c the continuum flux, which corresponds with the independent term of the first-order polynomial fit. The $line\ intensity$ is the integrated flux of the corresponding Gaussian component. Finally, in equation (2.4), r is the relative distance, in pc, from a fixed point of the spectrum y_0. Such point corresponds with the intersection of the two slits (in each case); y is the pixel coordinate along the slit, where the scale is 0.2 arcseconds per pixel and 5.5 Mpc is the distance to NGC 6946 (Sofue 1997).

2.4 Results

Previous studies of this star-forming complex suggest that we are facing a large superbubble in expansion (Efremov 1999; Elmegreen et al. 2000; Efremov et al. 2002, 2007; Larsen et al. 2002). Here, we perform a detailed analysis on the Hα kinematics and how it relates with the physical properties and geometry of the emission gas.

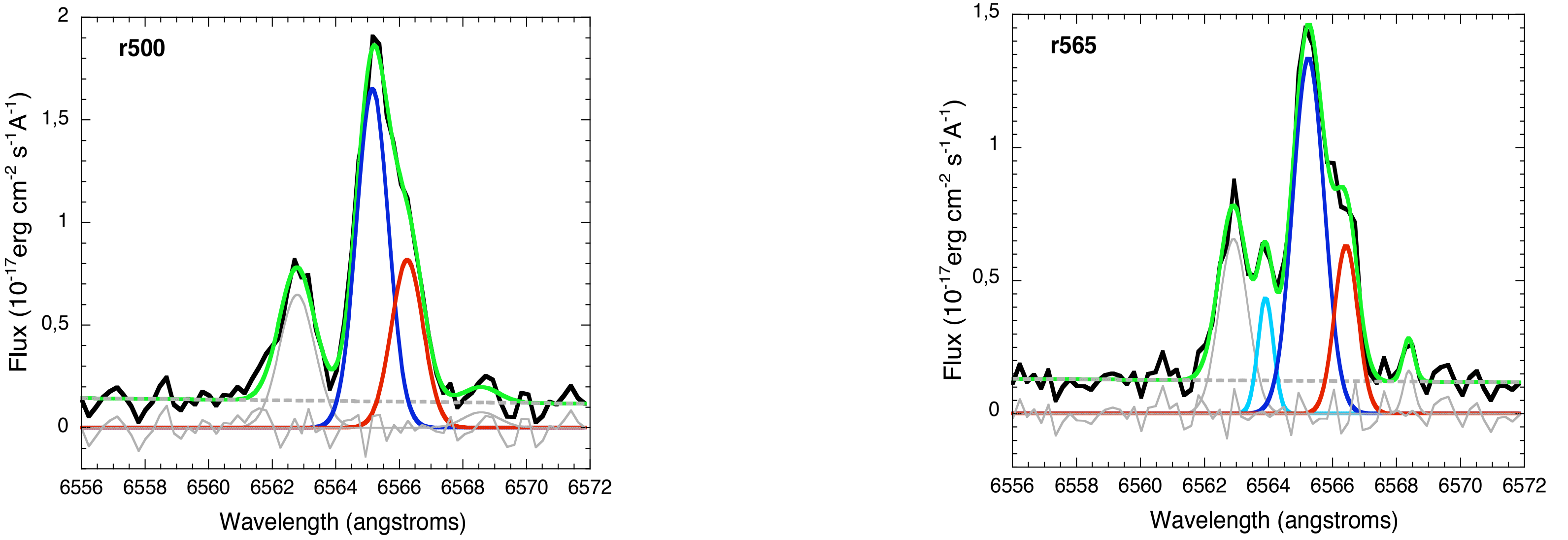

```
LINE 500
Line  Profile   Centre      Width    Peak Flux   Line Flux
 1      1      6562.790    1.305    6.487E-01   9.012E-01
       +/-        0.035    0.101    3.708E-02   6.022E-02
 2      1      6565.166    1.174    1.652E+00   2.065E+00
       +/-        0.019    0.040    4.802E-02   7.159E-02
 3      1      6566.259    1.174    8.169E-01   1.021E+00
       +/-        0.038    0.040    6.008E-02   5.732E-02
 4      1      6568.582    1.305    7.585E-02   1.054E-01
       +/-        0.215    0.101    3.487E-02   4.873E-02


Coefficients of polynomial: ordinate origin at 6556.017
                  1.4328E-01   -1.7004E-03
          +/-     1.5403E-02    1.7797E-03
0(All errors are 68% confidence intervals)
```

```
LINE 565
Line  Profile   Centre      Width    Peak Flux   Line Flux
 1      1      6562.790    1.305    6.487E-01   9.012E-01
       +/-        0.032    0.068    4.307E-02   4.028E-02
 2      1      6563.896    0.902    4.415E-01   4.238E-01
       +/-        0.055    0.068    4.246E-02   3.532E-02
 3      1      6565.224    0.998    1.339E+00   1.423E+00
       +/-        0.020    0.035    3.972E-02   4.622E-02
 4      1      6566.336    0.998    6.931E-01   7.363E-01
       +/-        0.035    0.035    4.183E-02   3.659E-02
 5      1      6568.390    0.413    1.626E-01   7.155E-02
       +/-        0.067    0.186    5.920E-02   2.670E-02
Coefficients of polynomial: ordinate origin at 6556.017
                  1.3281E-01   -9.7124E-04
          +/-     1.2950E-02    1.4193E-03
0(All errors are 68% confidence intervals)
```

Figure 2.3: Examples of two different fit cases. Left (r500): fit with two components for Hα and two for the sky. Right (r565): three components for Hα and one for the sky. These components are located at the center and represented with bold lines, with the same color code that in Figure 2.4: red for the 'red' component, receding gas, and blue for the 'blue' component, approaching gas. Light blue is for the third component, blueshifted at higher velocities. The component in gray corresponds to the sky background. The dashed line is the continuum fit. The green bold line is the global fit for the spectrum (black, bold line).

Table 2.3: Summary of the emission line fitting

Slit		Velocity[a]		FWHM[a]		EW[b]		Flux[c]	
		$\overline{V_{obs}}$	σ_V	$\overline{W_{obs}}$	σ_W	$\overline{EW}$	σ_{EW}	$\overline{F}$	σ_F
P.A. = 0°	(i)	106	25	27	12	9	9	0.99	1.08
	(ii)	148	29	25	11	12	11	1.19	0.89
P.A. = 296°	(i)	120	24	24	10	10	15	0.82	1.25
	(ii)	169	20	23	9	7	7	0.6	0.53

NOTE.- Mean ($\overline{X}$) and standard deviation (σ_X) of the variables obtained from the fits for the blue (i) and red (ii) components of the gas, for both slits. Values correspond only to the central part of the spectra, where the complex is located.
[a] km s^{-1}.
[b] Å.
[c] 10^{-17}erg cm^{-2} s^{-1} Å^{-1}.

The most significant result from the Hα fitting is that the emission line is resolved into (at least) two kinematic components of the gas along the full extent of the complex, ~ 700 pc. We refer as the 'blue component' of the gas that moving toward the observer at velocities of up to ~ 50 km s^{-1}, and as the 'red component,' the one receding at similar velocities.

Table 2.3 contains a summary of the mean values for the two kinematic components along the extent of the bubble, this is ∼(-21, 29) arcsec, or ∼(-660, 773) pc equivalently, from the bubble center for P.A. = 0°, and ∼(-52, 28) arcsec, ∼(-1387, 747) pc, for P.A. = 296°. At P.A. = 0°, the mean velocity is 106 km s^{-1} for the blue and 148 km s^{-1} for the red component, while at P.A. = 296° it is 120 km s^{-1} and 169 km s^{-1}, respectively. Outside this area, we could identify only one velocity component for Hα , which corresponds to the rotation velocity of the gas disk at the supercomplex location. The different line components observed is a clear signature of a bubble kinematics, and the radial velocities measured provide a lower limit to the expansion speed. We study this in detail in Section 2.4.5, once we have determined the main geometric parameters of the complex.

2.4.1 Kinematics and Geometry: Expanding bubbles

An analysis of the kinematics and geometry of the ionized gas is also derived from the results of the fits, which are summarized graphically in Figure 2.4. The heliocentric velocities are plotted versus the relative distance for all the positions along the slit. The reference position for the spatial scale corresponds to the intersection of the two slits (cf. Figure 2.9). The red component of the gas is represented with filled triangles (red color in the electronic version), and the blue component with filled circles (blue color). We can observe in these plots a complex structure of the gas, having several components with different kinematics. The overall kinematic structure is that of a gas bubble in expansion, sufficiently transparent so that the approaching blue component does not obscure the receding red component. The high spatial and spectral sampling of these data allow us to disentangle the expanding kinematics of the bubble.

For the case of P.A. = 0°, we could fit up to three kinematic components to Hα in some regions of the spectrum. This third component appears blueshifted at high velocities (~85 km s^{-1}) with respect to the rotation velocity of the galaxy at its respective position. It is represented as filled squares (and light blue) in Figure 2.4.

For the spectrum at P.A. = 296°, we always found two components as the best fit to the nebular Hα emission along the whole extent of the complex.

Efremov et al. (2002) studied the kinematics of the ionized gas within this complex through the Hα emission, using long-slit spectroscopy at several positions with the 6m BTA telescope. Only the blueward side of the bubble was detected and analyzed by these authors. The lower spectral dispersion (six times lower) and the larger seeing of their data as compared with the data we present here may be the reasons why Efremov et al. (2002) did detect only one main component. A 14$''$ long slit centered at the SSC, at P.A. $=-10°$, taken with the Keck-I telescope (see table 2.1), shows both velocity components in emission extending on both sides of the SSC. It is in this spectrum where they detect a bubble 6$''$ in radius and 60 km s^{-1} expansion.

The rest of the spectrum along the two slit position in our data shows the Hα emission of the interstellar medium surrounding the complex, and only one component was fitted. Emission from other Hα regions to the north and west ends of the slits can be seen in

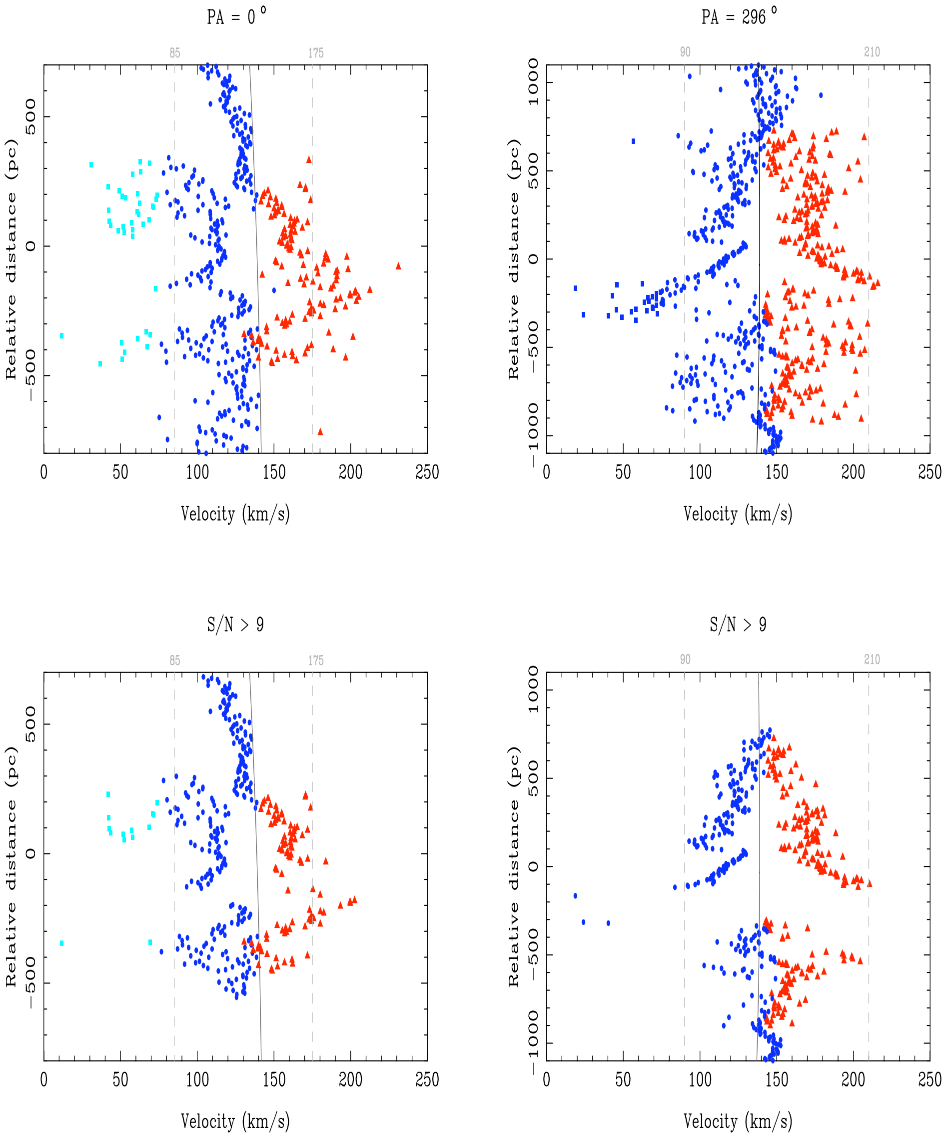

Figure 2.4: Top left: Hα velocity along the slit at P.A.=0°. In some locations only one component could be fitted (filled blue circles), in other locations two components were present (blue circles for the approaching and red triangles for the receding), while at other locations a third component at higher approaching velocities could be clearly identified (light blue squares). Top right: the same for the slit at P.A. = 296°; a maximum of two components could clearly be fitted. The bottom panels show the same data but after removing those points with fluxes smaller than $9\sigma_f$, where σ_f is the uncertainty in measuring the faintest emission line in the two-dimensional spectrum (see the text for details).

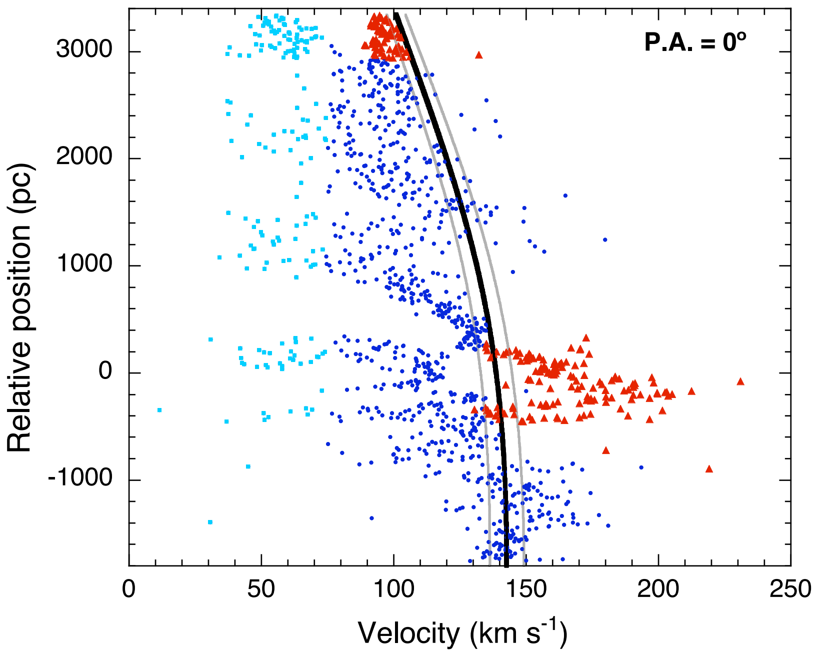

Figure 2.5: Same plot as in Figure 2.4, for the case P.A. = 0°, along 5330 pc representing nearly the full extent of the slit, where it was possible to fit at least one component to Hα. The rotation curve of NGC 6946 is also represented with the error limits from the fit (more details in section 2.4.2).

Figures 2.5 and 2.7. In Figure 2.7, the slits are represented on a Hα image of the galaxy. Figure 2.5 shows the complete kinematic map of Hα along P.A. = 0°, together with the rotation curve of the galaxy described in section 2.4.2 below (bold black line with its error limits in gray). The north tip of the spectrum could be fitted with two components, but this part of the data set is out of the scope of this work, so we do not further analyze it.

The bubble is clearly seen in Figure 2.5 between -500 pc and 400 pc with the kinematic components well differentiated. Outside the bubble, the emission appears to fit the gas rotation velocity at this galactic location (blue points); also an approaching component, at ~ 60 km s^{-1}, is present along the whole extent of the slit. The origin of the bluest component is still controversial, and it could represent the diffuse ionized gas (DIG) in the halo of the host galaxy (NGC 6946). Its constant velocity and low emissivity along the whole extent of the slit support this hypothesis, because the extraplanar gas does not follow the rotation curve of the disk (Heald et al. 2006). This velocity feature is also found by Efremov et al. (2007) in the HI emission. At the top right-hand and bottom left-hand panels of their Figure 14, the HI position−velocity diagrams for two slits are represented, with different position angles, and the structure in velocity is very similar to what we find here. A more detailed study is needed to elucidate the origin of this emission.

Errors in velocity measurements are larger for fainter intensities. In order to obtain reliable estimations of the bubble expansion velocities and to contrast the complex structure of the ionized gas, a filter is applied to eliminate those points with worse signal-to-noise ratio (S/N). We take as detection limit the weakest sky emission line that we can measure in the two-dimensional spectrum. Since the sky line flux must be constant along the slit, its variation gives us an approximation of the dispersion in the measurement of the faintest emission lines. Moreover, the intensity of the Hα emission in the disk of NGC 6946 outside the complex coincides with that of the weaker sky line, so the fluctuations of these lines about their mean value provide a good indicator of the uncertainty in measuring the weakest lines. The reference dispersion of the flux, σ_f, that we measure is $\sigma_f = 1.2 \times 10^{-17}$ erg cm^{-2} s^{-1}.

Most of the points in the top panels of Figure 2.4 have measured fluxes $> 3\sigma_f$. The bottom panels represent just the same data but only for those points where the flux is $> 9\sigma_f$. This is a very stringent criterium, but the result tells about the reliability of the kinematic structures seen in the data. If we compare with the top of Figure 2.4, now the structure is somewhat cleaner, but all the important features remain of the expanding bubble with much substructure around. Only some of the very faint points of the extremely blueshifted component remain after this strong constraint, although all of them have fluxes $> 3\sigma_f$.

Furthermore, at the bottom panel of Figure 2.4 there is a gap around a relative distance of -200 pc, more noticeable at P.A. = 296°. These gaps in the kinematics are clearly visible in the two dimensional spectrum in Figure 2.2, not only for Hα but also for [NII] and [SII]. The HI data in Efremov et al. (2007) also show this gap in the position−velocity diagram (compare their Figures 14, 19, and 21).

Dashed lines, in the bottom panels of Figure 2.4 mark approximately the maximum expansion velocities of both components. So, along P.A. = 296° we find a radial velocity amplitude of 60 km s^{-1}, corresponding to the larger difference in the main structure.

Overimposed to the large bubble we can observe smaller structures at each side of the large shell, which show deviations of ~ 35 km s^{-1} with respect to the main velocity of the bubble walls. At P.A. = 0°, the main radial velocity amplitude is 45 km s^{-1}, while the velocity deviations of the smaller substructures are always below 25 km s^{-1}.

The solid lines that run through the complex represent the rotation curve of the galaxy NGC 6946, corresponding to the complex zone. More details about how it has been calculated is described in the next subsection. The rotation curve sets the systemic velocity of the galaxy around the complex, and it does indeed matches the mean velocity computed for the expanding gas. These velocities are around 135 and 140 km s^{-1}, somewhat larger than the value given by Bonnarel et al. (1986, 1988) of around 125 km s^{-1}.

To better visualize our model of the gas kinematic structure, the top panel in Figure 2.6 shows a simple sketch drawn on the velocity–distance diagram. This Figure is similar to fig. 2.4, but now the velocity is in the ordinate axis and the points are drawn with their error bar. The Figure also includes the corresponding color-coded fluxes of the different components (units on the right-hand side ordinate axis). This panel also includes a sub-panel with the instrument-corrected velocity dispersion of the main blue component along the slit. The bottom detached panel plots the velocity dispersion of the two main components versus the Hα flux for all the points in the complex along the slit; its analysis is described below, at the end of the section. First, we compare and analyze the model at the top with the results from Figure 2.4.

This sketch gives an idea of the large size of the gas structure in expansion, the main bubble. As apparent from a cursory look, the main kinematic shell is highly structured. Both sides of the shell (approaching and receding), along the two slit positions, contain localized structures that could be interpreted as superposed smaller shells, likely having been formed as the result of star-forming events occurring at the edges of the larger scale shell (Larsen et al. 2002).

These smaller shells or bubbles detected at some locations along the two sides of the main shell of the complex do not appear as complete shells, but rather we only see one of their sides. One example of a small bubble is drawn in the receding main component of the bubble complex at location -200 pc, where we would be measuring a small bubble but only its receding component at ~30 km s^{-1} with respect to the main receding kinematic component at 170 km s^{-1}. Two additional examples are drawn on approaching component of the main complex; we have sketched two small bubbles at 0 pc and -250 pc where we can measure their receding component at $\sim$20 km s^{-1} with respect to the main approaching kinematic component at 110 km s^{-1}.

These clumps of emission along the main shell of the complex are likely second-generation star-forming regions occurring in the shocked and highly compressed walls of the main shell, produced by the combined effects of previous generation stellar winds and supernova explosions. This shell is surrounded toward the inside and outside by very low density gas. Thus, when the second-generation star-forming regions start to expand due to their stellar winds it is probable that they easily break into the lower density surrounding medium and we would only be able to see either the approaching or receding sides (Elmegreen & Lada 1977; Walborn & Parker 1992, and references therein). There is no doubt that these regions are locally ionized by star clusters. This can be observed in the Gemini image, Figure 2.1 (or expanded in Figure 2 of Efremov et al. 2007, or Figure 1 of Larsen et al. 2002); the HII regions across the shell of the complex, corresponding to the small bubbles, clearly contain stellar clusters inside.

An alternative explanation suggested by the large number of HVC in NGC 6946 would be that these smaller bubbles are the result of impacts by some of these HVC against the main bubble of the complex. The possibility of a HVC impact as a mechanism which might explain the formation of the complex is considered in Larsen et al. (2002).

Although the kinematic structure is quite symmetric overall, compatible with the idea of a bubble, it is not easy to explain the large size of the complex. Which mechanism caused this enormous complex is still under discussion. The idea of superexplosions has been put forward by Larsen et al. (2002); a highly energetic explosion that swept the gas to the shell of a large bubble, subsequently triggering a second-generation star formation in the shell. Formation of the younger stars might have been caused by such hypernova explosion ejected from the young super stellar cluster (YSSC; Efremov 2001), but even these explosions hardly explain the high energy required for such large bubble and the formation of the older stellar population in the complex or the YSSC. Comparison with HI intensity maps might help our understanding of the origin of this peculiar complex.

The bottom part of the top panel of Figure 2.6 shows the velocity dispersion of the blue component along the slit. The velocity dispersion values have been corrected quadratically for instrumental broadening using the Hα emission in the sky ($\sigma_{sky} = 24 \pm 5$ km s^{-1}). No clear tendency of the velocity dispersion along the slit is seen, although there is a hint of highs and lows anticorrelated with the line intensity.

For an idealized shell in expansion, an anticorrelation is expected between the velocity dispersion and the Hα intensity. This arises because in the center of the shell, as seen in projection, the integrated Hα intensity is lower than in the border, while the velocity dispersion is highest in the center (given that the radial component of the expansion velocity is maximum there). Muñoz-Tuñón et al. (1996), Martínez-Delgado et al. (2007), and Bordalo, Plana & Telles (2009) have explored further this correlation in their studies of giant HII regions and of blue compact galaxies (compare their Figures 2, 1, and 13, respectively). In the bottom panel of Figure 2.6, the expected trend of anticorrelation is clearly seen, confirming the overall geometry of an expanding shell.

The median value of σ along the complex is 11 km s^{-1}, which corresponds with a hydrogen kinetic temperature of T$\sim$4800 K, through the expression

$$\mathrm{KE_{avg}} = \overline{\left[\frac{1}{2}\mathrm{mv}^2\right]} = \frac{3}{2}\mathrm{K_B T}, \tag{2.5}$$

where $\mathrm{K_B}$ is the Boltzmann constant, and we have used the velocity dispersion for $\overline{\mathrm{v}^2}$.

If we calculate the sound velocity in the cloud, assuming the ideal gas law, we have that

$$v_s = \sqrt{\frac{\gamma R T}{M}}, \tag{2.6}$$

where γ is the adiabatic index, that for a monatomic ideal gas is 5/3; R is the molar gas constant; T is the temperature, for which we use the value estimated above 4800 K; and M is the gas molar mass. Assuming a gas composed only of hydrogen, we obtain a value of $c_s = 8.2$ km s^{-1}. So the velocity dispersion measured is supersonic. If we assume a gas mass composition of 90% percent hydrogen and 10% percent helium, the resulting sound velocity is even lower, $v_s = 7.1$ km s^{-1}, and the velocity dispersion is still supersonic. Notice that although marginally supersonic, these values of the velocity dispersion are *spatially resolved* along each side of the shell, which implies that these are locally supersonic velocities in a scale of ~ 5.3 pc (1 pixel). Supersonic line widths are one of the defining properties of giant extragalactic HII regions and starburst regions, and although their values are often measured of order or larger than 20 km s^{-1}, these correspond to much larger areas. Bordalo, Plana

& Telles (2009) give a recent detailed analysis of supersonic motions in IIZw 40, but their resolved pixel is of order 100 pc; see their paper for a detailed discussion of supersonic motions from an observational point of view.

2.4.2 Rotation curve of NGC 6946

To model the two-dimensional rotation of NGC 6946, we took the data from Blais-Ouellette et al. (2004), who measure the global Hα rotation curves from Fabry-Perot data centered at Hα . We apply the inverse procedure to compute a two-dimensional rotation map, shown in Figure 2.7. We compute the rotation map outside the central 50 arcsec radius, because the lack of Hα emission in the central part of the galaxy makes the true kinematics in that central region difficult to retrieve. This does not affect the region of interest, the star-forming complex that we study, which is located farther out, around 187$''$.5 (or 5 kpc), from the galaxy center (Larsen et al. 2002). The reason for using the Hα instead of the HI rotation curve (which would allow a complete map of the galaxy farther out) is due to the lower spatial resolution provided by the HI data which shows beam smearing (Blais-Ouellette et al. 1999; Swaters 1999; van den Bosch et al. 2000).

The rotation curve from Figure 7 in Blais-Ouellette et al. (2004) is fitted using the parametric model of Giovanelli & Haynes (2002),

$$V_{pe}(r) = V_0(1 - e^{-r/r_{pe}})(1 + \alpha\, r/r_{pe}), \tag{2.7}$$

where V_0 regulates the overall amplitude of the rotation curve, r_{pe} yields a scale length for the inner steep rise, and α sets the slope of the slowly changing outer part. After a least-square fit of this model to the data, the parameters obtained are $[V_0, r_{pe}, \alpha]$ = [138±8 km s^{-1}, 40±5 arcsec, 0.037±0.008]. Let V(r) be the rotational velocity of an axially symmetric disk at a distance r from its center (r being the radial coordinate along the disk's projected major axis). Let (x,y) be a set of Cartesian coordinates in the plane of the disk. If the disk is thin and it is inclined at an angle i (i = 90° for edge-on) to the line of sight, the observed component of the velocity, along the line of sight, that intercepts the disk at (x,y) is (Giovanelli & Haynes 2002)

$$V_{||} = V(r)\frac{x}{\sqrt{x^2+y^2}} sin\, i + V_{nc}, \tag{2.8}$$

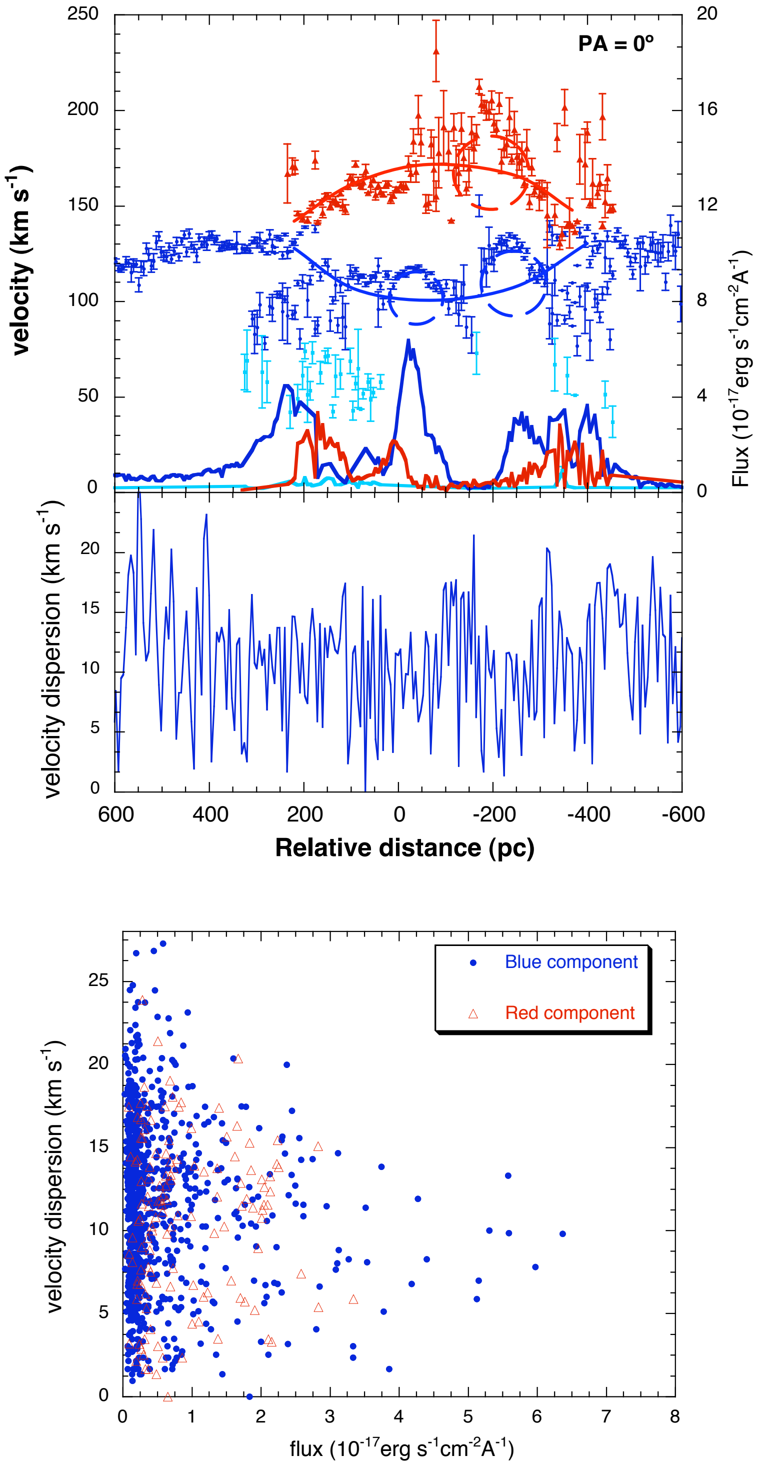

Figure 2.6: Top: a sketch of the kinematics of the gas suggested in the complex of NGC 6946. Velocity and velocity dispersion of the gas vs. relative distance along the complex. The relative flux of each component is also plotted. The model suggested for the kinematic of the gas, a large spreading bubble with small subbubbles on its wall at the same time, is indicated with the lines using the same color as the component of the gas that they represent.

where V_{nc} accounts for non-circular motions and x is oriented along the disk's apparent major axis. To obtain the observed component of rotational velocity, we use the Equation (2.8) above, ignoring the non-circular motions and adding the systemic velocity of NGC 6946, 145 km s^{-1},

$$V_{||} = V(r)\frac{x}{\sqrt{x^2+y^2}} sin\, i + 145. \tag{2.9}$$

The inclination angle used is $i = 38°$ and the position angle of the line of nodes $60°$ (Blais-Ouellette et al. 2004).

Once we have the rotation curve projected on our tangent disk, it is azimuthally expanded around the center of the galaxy to obtain the two-dimensional model map, shown in the left panel of Figure 2.7. The location of the young SSC is marked by a star, and the two slit positions, at P.A. = 90° and 296°, are represented by full lines. The full and dashed lines are the isophotes for negative (approaching) and positive (receding) velocities, respectively. The range of velocities shown spans from -80 km s^{-1} to 160 km s^{-1}. On the right-hand side, the Hα image of NGC 6946 around the complex is shown with the two slits and five model isovelocity contours.

2.4.3 Size of the Hα complex

To obtain a value for the size of the shell radius, we use a method based on the characteristic radial profile of an emitting bubble. For a hollow shell of a given thickness seen in projection on the plane of the sky, the radial dependence of the observed flux from this shell has a characteristic form with a maximum at the radius of the shell, decreasing inward to a minimum value at the shell center, and decreasing outward to a vanishing flux value. Figure 2.8 shows the pixel-to-pixel radial dependence of the Hα flux from the narrow band image. Instead of the actual flux, we represent the equivalent root mean square (rms) density of the emitting gas[4]. Instead of plotting each pixel, for the sake of clarity, we represent the number of pixels (in log units) with that value of $n_{rms}(H_\alpha)$ in a discrete grayscale. The thin dashed line represents the radial dependence of an idealized shell of inner radius 365 pc and 45 pc thickness, plus an r^{-1} fall off density gradient outside the shell. The bold line is the integral

---

[4] $n_{rms}(H_\alpha) \propto \sqrt{n_p n_e}$, where $4\pi j_{H_\alpha}/n_p n_e = 3.56\times10^{-25}$ (case B at a temperature of 10^4 K, Osterbrock & Ferland 2006). To calculate the emission coefficient j_{H_α}, for an unresolved source and assuming that the source is uniformly emitting, the total luminosity is $L = 4\pi j_{H_\alpha} V$. Where V is the emitting volume, and the flux received at a distance d is $F_{H_\alpha} = L_{H_\alpha}/4\pi d^2 = j_{H_\alpha} V/d^2$.

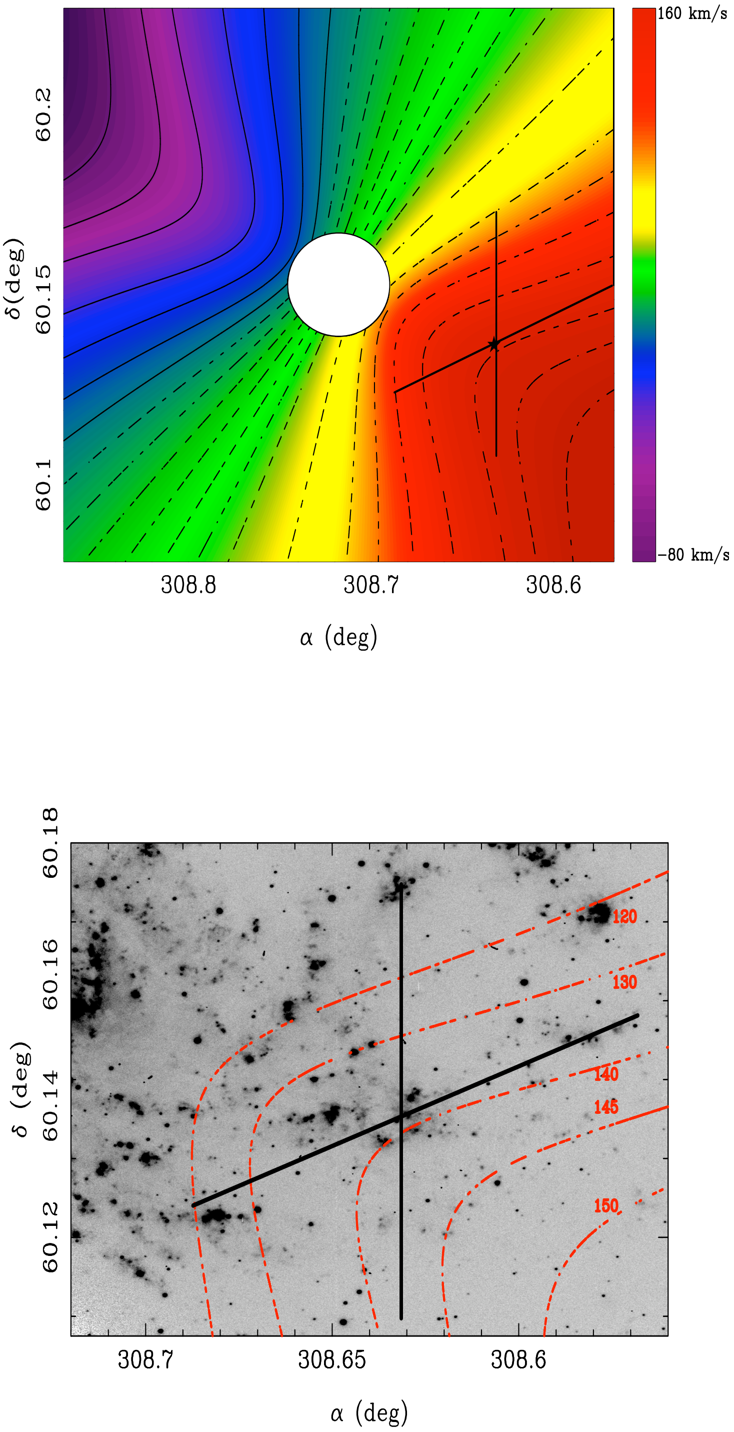

Figure 2.7: Rotation velocity map of NGC 6946. Top: two-dimensional model map obtained by fitting the rotation curve from Blais-Ouellette et al. (2004) with the parametric model $V_{pe}(r) = V_0(1 - e^{-r/r_{pe}})(1 + \alpha\, r/r_{pe})$ (Giovanelli & Haynes 2002). Isophotes are represented with full lines for negative (approaching) velocities, and with dashed lines for positive (receding) velocities. The two slit positions are also represented and a star indicates the location of the SSC. The white circle in the middle of the map indicates the lack of Hα data at distances less than 50 arcsec from the galaxy center. Bottom: Hα image with five isovelocity contours overplotted as well as the two slit positions.

of this radial density law projected on the plane of the sky. This resulting bold line provides a fair representation of the data. The Hα emission in the complex is obviously much more structured as seen from the image, and in particular it has a significant contribution from the ISM outside the idealized shell, which accounts for the emission outside the $365 + 45$ pc radius. In our simplified picture, this emission outside the idealized shell is represented by the r^{-1} fall-off density gradient. This is not meant to be a fit to the data, but rather an approximate idealized representation of the overall geometry of the region.

This method involves the uncertainty of having to choose the center of the complex. The central SSC (Larsen et al. 2002; Efremov et al. 2002) is taken initially as reference, being closer to the center of this spherical structure model. Different attempts were done, choosing the center of the bubble around in a small central region to the northeast of the SSC. The resulting radial distributions do not change significantly the pixel−density structure of the Figure.

The value of the inner radius that we obtain, 365 pc, is larger than the values given in the literature, of ∼300 pc (Larsen et al. 2002; Efremov et al. 2002), but it is somewhat smaller than the value expected observing the velocity−position plots, Figure 2.4.

2.4.4 Density profile of the Hα complex

Using the Hα flux, the rms density of the ionized gas can be calculated to obtain the density profile in the complex. In Figure 2.9 the pixel density of rms density values obtained from Hα is represented instead of its flux, since these quantities are proportional this does not affect the structure of its radial distribution.

There is a direct relation between the flux and the rms density through the definition of the effective recombination coefficient (Osterbrock 1989),

$$n_p n_e \alpha_{nn'}^{eff} = \sum_{L=0}^{n-1} \sum_{L'=L\pm1} n_{nL} A_{nL,n'L'} = \frac{4\pi j_{nn'}}{h\nu_{nn'}} \tag{2.10}$$

where the effective recombination coefficient of Hα is α_{32}^{eff}, n_p and n_e are the proton and electron density respectively, h the Planck constant, $h\nu_{32}$ the energy of the transition, and j_{32} is the emission coefficient of the line. The left side of eq. 11 (erg cm^3 s^{-1}) is tabulated for H_β (Osterbrock & Ferland 2006), and taking case B at a temperature of 10000 K:

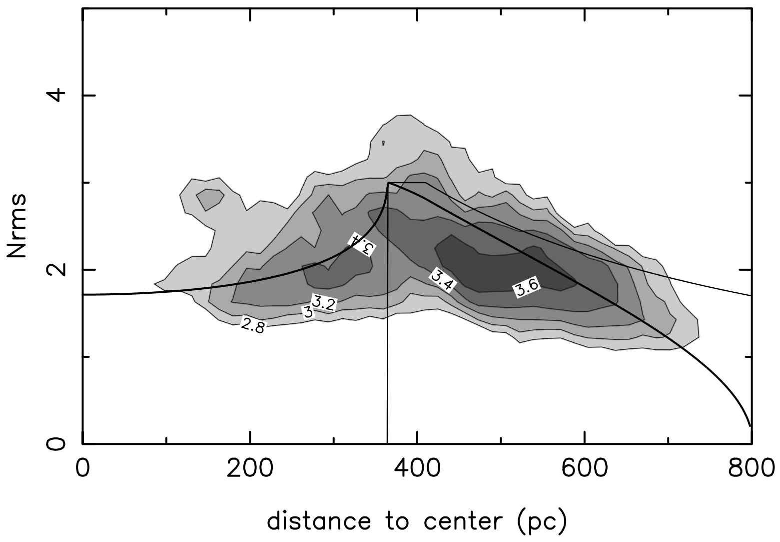

Figure 2.8: Root mean square (rms) density radial profile obtained from the Hα image. The grayscale contours represent (in log units) the number of Hα image pixels at that distance from the center of the bubble with a given value of the gas rms density (as obtained from the Hα flux). The thin dashed line is the radial dependence of the gas density of an idealized shell, plus an r^{-1} fall off law outside the shell. The thick line represents the integral of this radial density law, which gives a fair representation of the data, indicating that the ionized gas emission can indeed be approximated by a shell. If an extinction correction were applied to Hα brightness of A$_B = 1$, the rms density values would increase by a 30%.

$$4\pi j_{H_\alpha}/n_p n_e = 3.56 \times 10^{-25} \tag{2.11}$$

Thus, by calculating the emission coefficient, j_{H_α}, we obtain the Hα rms density $n_{rms}(H_\alpha) \sim \sqrt{n_p n_e}$. For an unresolved source, if it is assumed that the source is uniformly emitting, the total luminosity will be $L = 4\pi j_{H_\alpha} V$, where V is the emitting volume, and the flux received at a distance d is $F = L/4\pi d^2 = j_{H_\alpha} V/d^2$. In this way we have related the flux, at each pixel in the image, with the emissivity of the Hα line and therefore with the rms density, $n_{rms}(H_\alpha)$. Because we are integrating the emission of the bubble along the line of sight to the plane of the sky, the volume of one pixel of the image used is equal to the area of one pixel multiplied by the depth of the bubble at the corresponding distance from its center.

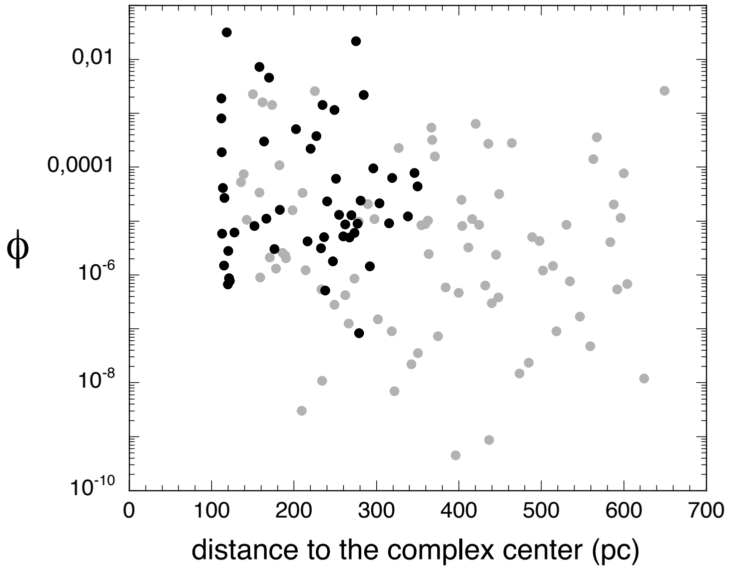

Figure 2.9: Radial dependence of the filling factor from the bubble center along the two slits, black circles for P.A. = 0° and grey circles for P.A. = 296°.

In a similar way, we can calculate the rms density along the slits using the Hα line flux from the fits to the spectra. Moreover, from the [SII] $\lambda6716/\lambda6731$ ratio it is possible to obtain an estimation of the electron density, n_e, which, compared with the rms density at the same location, can be used to compute the filling factor of the HII region along the slit. The two [SII] lines were fitted in the same way as described for Hα (section 2.3) to calculate the electron density from their flux ratio, but using only one gaussian component per line. For a consistent comparison between the electron density n_e, obtained from the [SII] fluxes ratio, and the rms density n_{rms}, obtained from the Hα line flux, the Hα line were fitted again but using only one component. Once these two values of the density are calculated at the same locations, the filling factor is computed from the following equation,

$$\phi = (\frac{< n_e >_{rms}}{n_e})^2 \tag{2.12}$$

Figure 2.9 shows the resulting values of the filling factor versus the radial distance to the shell center. The values within the complex, at distances from the center less than ∼365 pc, cover a range of 10^{-2} to 10^{-6}, which is normal in HII regions (Rozas et al. 1999, 2000). Values in the ISM outside the complex, at distances larger than 365 pc, are smaller by some two orders of magnitude on average, 10^{-4} to 10^{-8}.

2.4.5 Radial expansion velocities: Timescales.

In order to calculate the actual velocities of the shell expansion, we assume a bubble with spherical symmetry, and compute the radial velocities along the two slits on the projected geometry of the bubble, as explained below.

Neither of the slits runs through the center of the bubble, therefore the observed velocities are not exactly the radial velocities, since the slit does not determine a maximum circle. They are the projection of the corresponding component of the radial velocity to line of sight, so the observed velocities are lower limits of the actual radial velocities.

As the slit determines a circular section that does not contain the diameter of the sphere, the maximum velocity we can observe is the radial velocity multiplied by the cosine of the angle determined by the distance of the slit to the center of the sphere. This is, the observed velocity is then given by

$$v_{obs} = v_r\, cos\, \alpha\, cos\, \beta, \tag{2.13}$$

where v_r is the radial velocity of expanding gas, α is the angle along the slit, and β is the angle from the spherical coordinates (Figure 2.10), determined by the position of the slit.

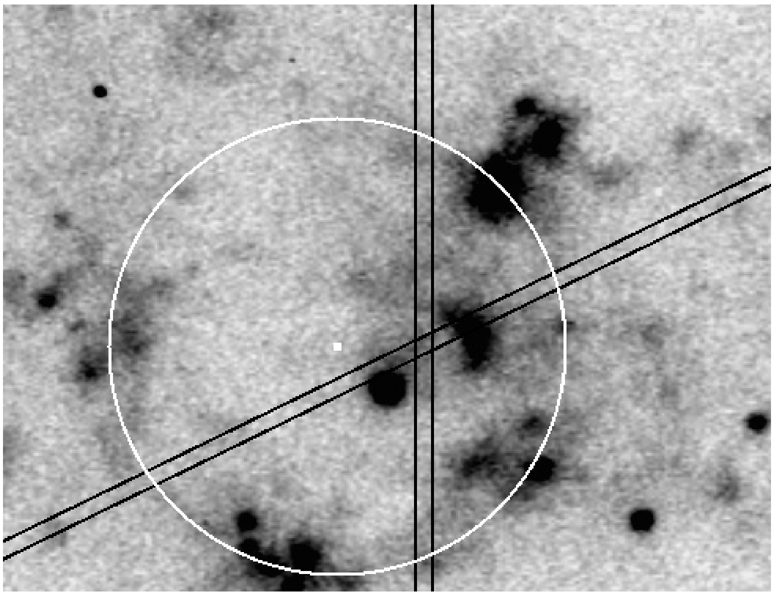

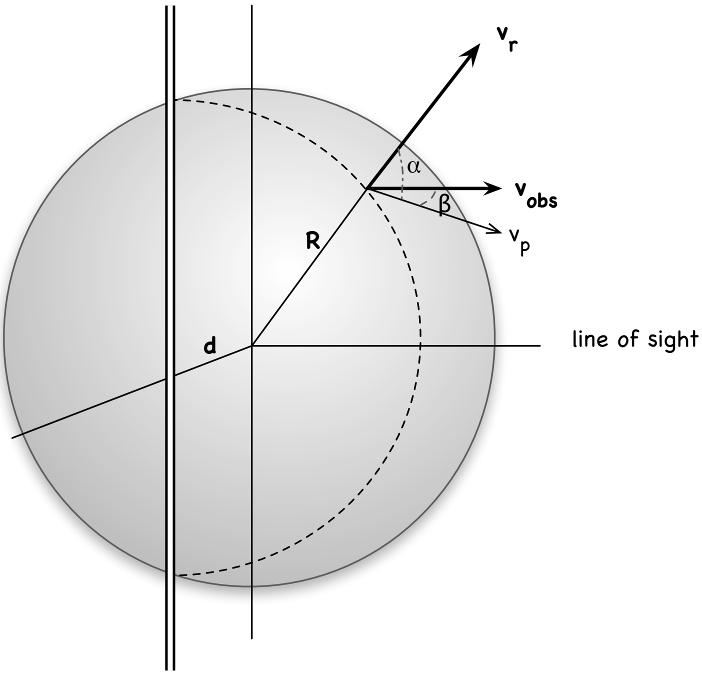

Figure 2.10: Top: an Hα image of the complex (from the NOT telescope) with the slits and a representation of the inner radius resulting from the simplified shell model (paragraph 2.4.3). Bottom: model of the bubble and slit geometry for the case of P.A. $= 0^\circ$. The case for the another slit position is analogous.

The maximum velocity along the slit is given by $v_{obs} = v_r \, cos\beta$, corresponding to the projection of the radial velocity on the plane that contains the line of sight and is perpendicular to the slit, $\alpha = 0$. To obtain the expansion radial velocity from the observed value, we only have to determine the angle β for $\alpha = 0$. This angle depends on both the distance of the slit to the center of the bubble, d, and also on the radius of the bubble, R, as follows

$$sin \, \beta = d/R. \tag{2.14}$$

This simple relation is directly deduced from spherical coordinates, from the triangle formed in the plane containing the line of sight when $\alpha = 0$ (cf. Figure 2.10). In section 2.4.2 above, we estimated both the bubble center and the radius, R $\sim$ 365 pc, which inserted into these geometric relations, equations (2.13) and (2.14), provide an estimation of the expansion velocity.

For the slit at P.A. = 0°, the distance of the slit to the bubble center is 118 pc, and the observed expansion velocities are around 35 $-$ 45 km s^{-1}, so from equations (2.13) and (2.14), and taking $\alpha = 0$ to get the maximum value, the corresponding expansion velocities are $v_r \sim$ 37 $-$ 48 km s^{-1}. For P.A. = 296°, the distance between the complex center and the slit is 66 pc, and the measured expansion velocities are $\sim$ 35 $-$ 50 km s^{-1}, giving true expansion velocities of $v_r \sim$ 36 $-$ 51 km s^{-1}.

Using as the true expansion velocity, 37 km s^{-1}, it is possible to compute the expansion time of the main bubble through the simple formula t_{dyn}(Myr) = R(pc)/v(km s^{-1}) $\approx$ 10 Myr.[5] This kinematic age is compatible with the age estimated for the stellar population of the SSC, $10 - 15$ Myr (Larsen et al. 2002), where the stellar winds and supernovae explosions would be the main source for the energetics of the shell expansion.

Similar calculations can be applied to a different part of the complex. In section 2.4.1 above, we identified the small-scale structures in the wall of the main expanding bubble as the bubbles corresponding to the second generation of star formation, produced by the compression of the ISM by the expansion of the main shell (cf. Larsen et al. 2002). If we take one of these small bubbles on the wall of the main shell, measure its radius, r $\sim$ 80 pc, and its observed expansion velocity (with respect to the expansion velocity of the main shell) of $\sim$ 20 km s^{-1}, giving then a $t_{dyn} \sim$ 4 Myr. The expansion time of this small

---

[5] t_{dyn} is estimated assuming that the expansion velocity remains constant during the life of the bubble, giving just an order of magnitude for the age.

bubble is compatible with the stellar ages of this second generation of star formation, given that Efremov et al. (2002) find an age of 4 Myr for the stellar population in the arc-shaped structure to the northwest of the central SSC.

2.5 Diagnostic Diagrams

Plots of emission-line ratios are developed in this section with the aim to determine the main mechanism of excitation of the ionized gas. The structure and stellar evolution of this star forming complex encompasses a suit of ionization and excitation processes, including photoionization by hot stars and shocks by stellar winds and supernova explosions among other, and here we explore whether with these data sets it is possible to distinguish them.

Baldwin, Philips & Terlevich (1981; BPT) researched how to classify empirically extragalactic objects based on their predominant excitation mechanism, from several combinations of pairs of easily measurable emission-line ratios. They separate these mechanisms into four categories: gas ionized by hot stars of type O and B, as in HII regions or star forming regions; planetary nebulae, photo-ionized by stars hotter than type O; photo-ionization by a non-thermal continuum following a power law, as in active galactic nuclei (AGNs); and gas heated by shock waves.

BPT found that these four groups can be efficiently separated by plotting [NII]λ6584/Hα versus [OIII]λ5007/Hβ, and [OII]λ3727/[OIII]λ5007 versus [OIII]λ5007/Hβ, [NII]λ6584/Hα , or [OI]λ6300/Hα .

These diagrams have been used extensively and their utility for classification has been widely demonstrated. They were also used as abundance diagnostics in emission nebulae (Sabbadin, Minello & Bianchini 1977; D'Odorico 1978; Dopita 1977, 1978).

Looking for the best choice among all the possible emission-line ratios, Veilleux & Osterbrock (1987) gave some criteria that include choosing strong nearby lines which are not blended; preferably a ratio of a forbidden to an HI Balmer. The line ratios satisfying these criteria are the following: [OIII]λ5007/Hβ, [NII]λ6583/Hα , and [SII](λ6716+λ6731)/Hα .

2.5.1 Computing the emission line ratios

In order to achieve enough S/N in [OIII] and Hβ, which are faint in our spectra, we have extracted the spectra adding a few pixels around the brightest regions. Figure 2.11 shows spatial cuts of spectra along P.A. = 0° and P.A. = 296°, each one centered at the wavelengths around Hα and Hβ. The whole length of the slit is shown, and the location of the star-forming complex is marked by an arrow in the cuts around Hβ. In the cuts centered at Hα, numbers indicate the locations from where the spectra have been extracted. We used DIPSO to fit Hα, [NII], and [SII] from the red spectra, and Hβ, and [OIII] from the blue spectra, at both slit P.A., and then computed the flux ratios $log(I_{[OIII]\lambda5007}/I_{H\beta})$, $log(I_{[NII]\lambda6584}/I_{H\alpha})$ and $log(I_{[SII](\lambda6716+\lambda6731)}/I_{H\alpha})$.

Unfortunately, the emission in the blue spectra is still very faint even after the coadded extraction, and there are very few points remaining with enough signal to fit the Hβ and [OIII] lines. In this circumstance, we decided to use the diagnostic diagram log([SII]6717+6731/Hα) versus log([NII]6584/Hα). We use two types of measurements to construct the diagnostic diagram, pixel-by-pixel fluxes along the slit and coadded extractions around the brightest knots. The models used to analyze these ratios and to determine the ionization mechanism involved are described below.

I.- In Figure 2.12, we use the models by Sabbadin, Minello & Bianchini (1977; SMB77) as regions separating main groups of ionized regions dominated by different ionization and excitation mechanisms. SBM77 introduced the electronic-excitation density diagrams with the aim to understand the nature of the nebulae S176. These diagrams compare the emission-line ratios Hα/[NII], [SII]$\lambda\lambda$6717/6731 and Hα/[SII] observed in supernova remnants (SNR), planetary nebulae (PNe), and HII regions. These nebulae are supposed to be in different regions in the diagrams due to the different ionization and excitation processes governing their nebular structure. The model is adapted to the ratios that we measure in this work. SBM77 model is still widely used, e.g., López-Martín et al. (2002), Riesgo & López (2006), and Phillips & Cuesta (1999).

SMB77 model locates the complex in the region associated to photoionization by hot massive stars. Most of the points are inside or close to the HII region box, as it can be seen in the top panel of Figure 2.12. A fraction of the points lie outside the HII region box; those few points indicating low values of the two ratios may correspond to higher excitation regions. More significantly, the points corresponding to higher values of the two ratios, located in the transition zone between HII and SNR, could indicate the presence of shocked gas, which would be represented by larger [SII]/Hα and [NII]/Hα ratios. This result is suggestive but tentative, because only a few data points remain with fluxes above $9\sigma_f$ outside the HII box. The overall ionization structure of a star-forming complex is dominated by the hot massive stars, while the impact in the ionization structure by the SNR and PNe in these giant complexes is less readily ascertained in the diagnostics diagrams (Martin 1997). Thus, this result is promising but higher spatial resolution and S/N spectra are needed to confirm it. Notice that this is consistent with the supersonic velocity dispersion values measured across the shell.

II.- In Figure 2.13, we use the model by Dopita & Sutherland (1996; DS96). This is a high-velocity radiative shock model, including the magnetic pressure as support of the photoionization/recombination zone. It is a more complete and elaborate model, and it can explain some objects which cannot be understood in terms of the simpler photoionization models with a central source. The basic physical idea is that a high-velocity radiative shock in the ISM is an important source of ionizing photons. These photons are produced in the cooling of hot plasma after the shock, and they may spread encountering the pre-shock gas and forming a precursor HII region. We use this model to look for some clues of shocks within the complex. Data to represent the grid are obtained from Table 8 in DS96, paper I. This is a low-density steady-flow model, the shock velocities lie in the range 150 $\leq$ V$_S$ $\leq$ 500 km s^{-1}, and the magnetic parameter 0 $\leq$ B/n$^{1/2}$ $\leq$ 4 μG cm$^{-3/2}$.

When comparing the emission-line ratios with the grid of the DS96 model, Figure 2.13, data points are located in zone of shocks with low velocities and magnetic parameter. Better S/N data would be required to make a more detailed study of the presence of shocks and their role. Efremov et al. (2002) conclude that the intensities of Balmer, [NII], and [SII] emission lines within and around the complex indicate that shock excitation makes a contribution to the emission from the most energetic region.

2.6 Summary

The gas-star supercomplex located in the galaxy NGC 6946 is an excellent laboratory for the study of the interaction between the massive star formation and the gas cloud where the

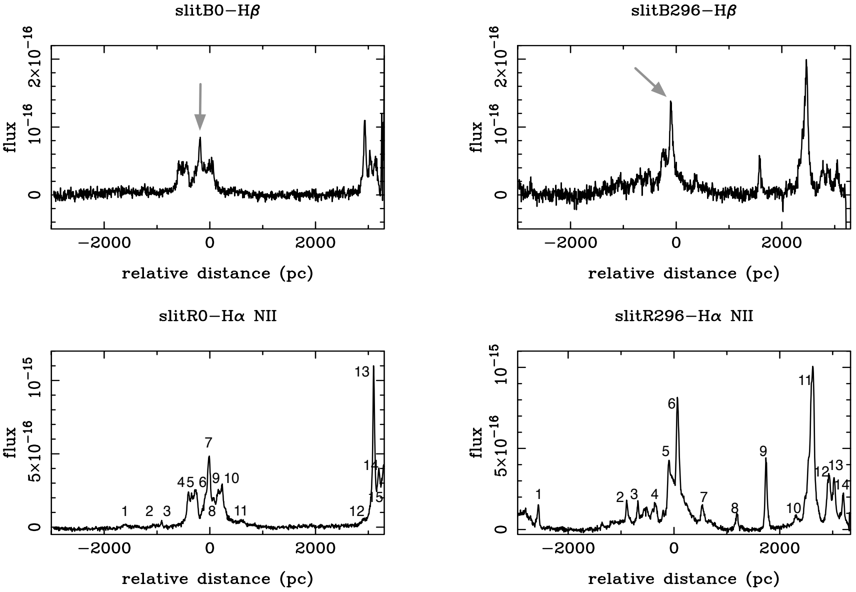

Figure 2.11: Spatial cuts along the slit at P.A. = 0° and P.A. = 296° for the blue and red spectral ranges. Abscissa is in parsec, and ordinate represents flux in erg cm^{-2} s^{-1}Å^{-1}. The location of the complex is marked with arrows in the cuts around Hβ; numbers indicate that the locations were spectra were summed and extracted for the diagnostic diagrams.

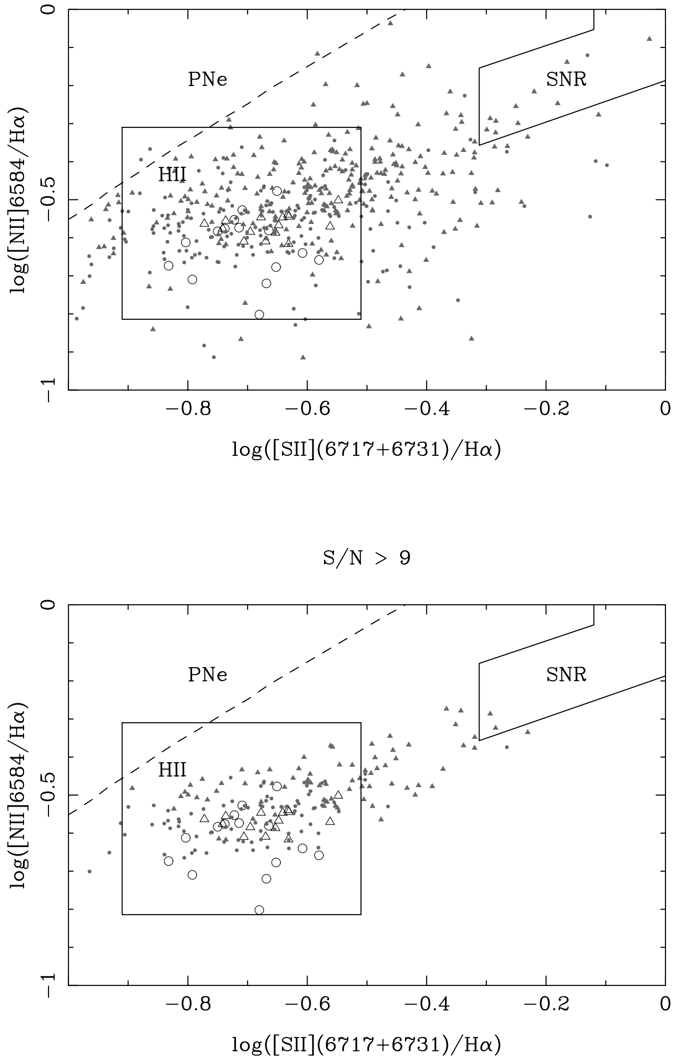

Figure 2.12: Diagnostic diagram of the brightest emission line ratios in the red spectral range. The top panel shows all the ratios measured along the slit, while the bottom panel shows only those with S/N $> 9\sigma_f$. The small filled symbols represent the pixel by pixel measurements along the slit across the star-forming complex, while the large open symbols represent the coadded extractions around the brightest knots (circles for P.A.=0° and triangles for P.A.=296°).

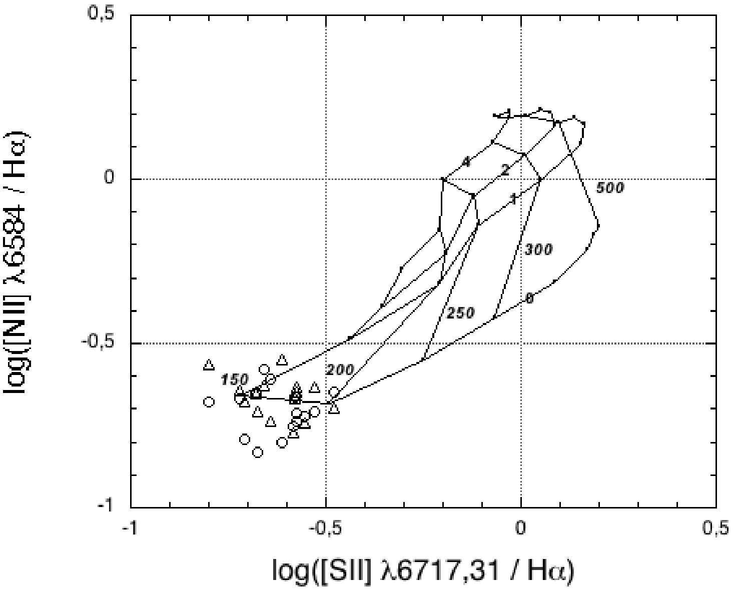

Figure 2.13: Comparison of the emission-line ratios log([NII]λ6584/Hα) vs. log([SII]λ6717,6731/Hα) with the DS96 high velocity shocks grid of models, with shock velocities in the range 150 $\leq$ V$_S$ $\leq$ 500 km s^{-1}, and magnetic parameter 0 $\leq$ B/n$^{1/2}$ $\leq$ 4 μG cm$^{-3/2}$. The circles and triangles represent ratios from the spectrum at P.A. = 0° and at P.A. = 296° respectively.

stars originated. The presence of a SSC with a mass around 10^6 $M_\odot$ and an age younger than 20 Myr appears to be the main source of ionizing photons able to generate an Hα bubble near 730 pc in diameter. Previous studies of this star-forming complex indicate its shell geometry (Larsen & Ritchler 1999; Efremov 1999; Elmegreen et al. 2000; Efremov et al. 2002, 2007; Larsen et al. 2002), and here we carry out a comprehensive analysis of the kinematical and photometric parameters of a shell in expansion. Moreover, in this study we obtain for the first time the large-scale velocity field of both bubble sides, the approaching and receding walls, which shows a complicated pattern with subbubbles forming at the walls of the largest structure, in a similar scheme to the formation 'a la Huygens', where some points on the surface of the previous bubble become the formation center of the second-generation bubbles. The estimated ages (Elmegreen et al. 2000; Larsen et al. 2002) of the supercluster and of the younger stellar population forming an arch like structure at the northwest side of the bubble center are compatible with this scenario. This spectroscopic analysis provides detailed information about the spatial distribution along the bubble of several variables concerning the physical state of the gas such as gas density, velocity dispersion, and line ratios, making this object the best available probe for testing dynamical and physical models of superbubble generation.

The radius calculated for the main bubble is 365 pc, somewhat larger than the values given in the literature at the moment. The radial expansion velocity of the complex is calculated in the range 37−50 km s^{-1}. Furthermore, with the lower limit of the radial velocities, $v_r = 37$ km s^{-1}, an estimation of the (dynamical) expansion time for the complex is about 10 Myr. This age is consistent with the stellar ages within the central part of the complex. This fact supports the hypothesis for the origin of the large bubble due to a sequence of supernova explosions, which would provide enough energy for such a large bubble.

The diagnostic diagram from the emission-line ratios show that most of the ionization arises from energetic photons from massive stars, while there are indications that some locations may be ionized by low-velocity shocks from stellar winds and/or supernova explosions, consistent with the supersonic velocity dispersion measured throughout the shell.

3

Corrugated velocity pattern in spiral galaxies

Contents

3.1 Introduction 57
3.2 Galaxy Sample 61
3.2.1 NGC 278 61
3.2.2 NGC 1058 62
3.2.3 UGC 3574 65
3.2.4 NGC 2500 65
3.3 Observations and data reduction 65
3.4 V_Z calculation. Preliminary results. 69
3.5 Diagnostic Diagrams 73
3.6 Summary 78

3.1 Introduction

The disks of spiral galaxies are highly structured. Besides the spiral arms typically associated to the galaxy main plane, there are systematic deviations, above and below the plane, which show characteristic patterns. These patterns receive several names such as tilts, warps, etc. In particular, the sinusoidal wave-like morphologies observed in both, gas and stellar, components of the Milky Way have been called **corrugations**. These structures are also apparent in some edge-on external galaxies (Arp 1964, Florido *et al.* 1991) as well as in a wide range of wavelengths. Reviews of the different observational properties can be seen in Spicker & Feitzinger (1986), Malhotra & Rhoads (1995), Alfaro & Efremov (1996), and Alfaro (2004).

The origin of corrugations has been ascribed to either well-localized features, such as spiral arms and collisions with high velocity clouds (HVCs), or to large scale perturbations such as gravitational interactions. For instance, some authors have explored the possibility of undulations along spiral arms, induced by magnetogravitational instabilities (see, e.g., Nelson 1985; de Castro & Pudritz 1992; Kim *et al.* 1997; Franco *et al.* 2002). In this case, the arms are corrugated by the undular mode (Parker 1966) of the instability, and the structuring occurs only in the azimuthal direction (a possible association to the radial patterns could be made if one assumes that these are projection of the azimuthal corrugations on the radial direction). Another localized origin could be ascribed to collisions of HVC with the disk of the galaxy; HVC impacts could cause the midplane disk to oscillate in a mode of wavy patterns as well (Franco *et al.* 1988; Santillán *et al.* 1999). In the large scale scenario, the undulations represent the natural response of the disk, which behaves like a loose drumhead, to the perturbations induced by either some companion galaxies or other galactic subsystem (Weinberg 1991; Edelsohn & Elmegreen 1997).

One obvious inference is that these corrugations should be associated with equally undulated coherent motions, and models addressing the vertical displacements also show wavelike z-velocity fields with amplitudes of the order of tens of km s^{-1}(see, e.g., Nelson 1976, 1985; Franco *et al.* 1988, 2002; Edelshon & Elmegreen 1997; Kim *et al.* 1997; Santillán *et al.* 2000; Gómez & Cox 2002, 2004).

Despite this expectation, however, the data about actual velocity features associated with spatial corrugations are scarce, only a few works aimed to detect and analyze the behaviour of the perpendicular velocity field across a spiral arm, as Alfaro *et al.* (2001) or more recently Matthews & Uson (2008).

This project is mainly based on previous results, such as, on one hand, observational evidence of kinematic corrugations across one spiral arms in NGC 5427 (Alfaro *et al.* 2001, see their fig. 2). On the other hand, a theoretical model based on the interaction between a spiral perturbation and a magnetized thick disk seems to explain the main features observed in NGC 5427 (Gómez & Cox 2002, see their fig. 17). 3D MHD models show that Parker instability in a thick magnetized disk, including the presence of a spiral arm, triggers the formation of large interstellar clouds (with masses in the range of $10^6 - 10^7$ solar masses) inside the arms but generates only small structures with slight density enhancements in the interarm regions. The resulting clouds are distributed in an antisymmetric way with respect to the midplane, and their masses are similar to those inferred for HI superclouds in our Galaxy. Such a cloud distribution results in an azimuthal corrugation along the arm, and for conditions similar to those of the optical segment of the Carina Sagittarius arm, it has a wavelength of about 2.4 kpc. A corrugated velocity pattern along the arm is also advanced. The typical scale length is similar to that of spatial corrugations (Franco *et al.* 2002).

The main interest of this kind of studies resides on the apparent connection between the 3D structure of galactic disks and large scale star formation processes. The same mechanisms shaping the aspect of the galaxy seem to be the responsible, at large scales, of the gas arrangement in the disk and later triggering of star formation (Alfaro *et al.* 1991, 1992).

Thus, the immediate aim of this work is addressed to:

- Prove the existence of velocity corrugations in a sample of face-on (i$\leq 25^{\circ}$) spiral galaxies.

- Characterize their main observational properties, such as: amplitudes, typical spatial scales, azimuthal and radial patterns, etc.

- Use this information to provide observational constrains to the different theoretical models provided to explain the origin of the kinematic corrugations.

The current work is in an early stage, presenting preliminary results from the kinematic vertical velocity determinations across the galactic disks of a sample of nearby, nearly face-on, spiral galaxies.

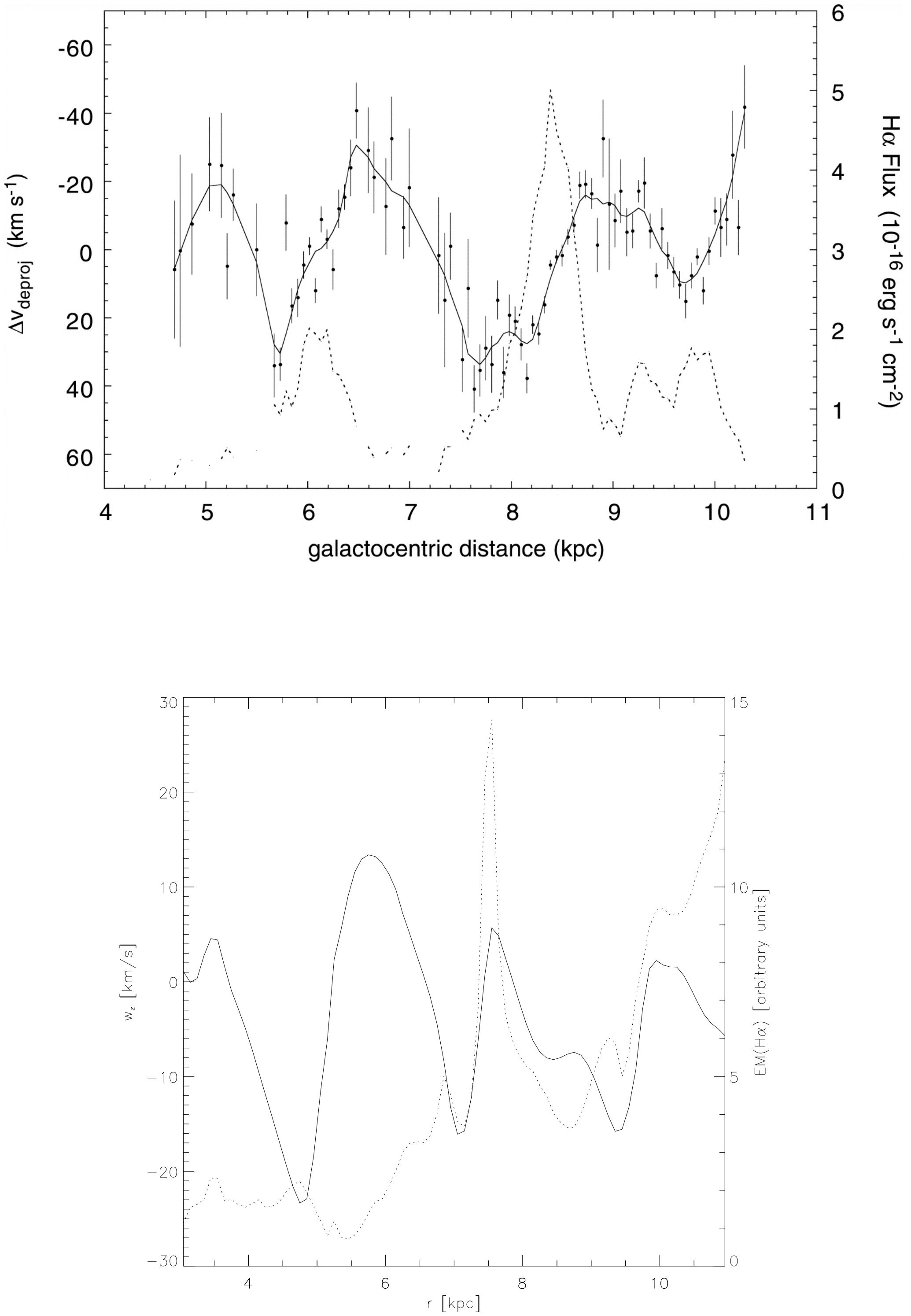

Figure 3.1: *Up: Fig. 2b of Alfaro et al. (2001).* The velocity (dots with error bars) and intensity (dotted line) curves between 5 and 10 kpc, where the relationship between the velocity and intensity structures is clearest; the velocity curve has been detrended for the gentle rising slope and plotted upside-down, with the approaching blueshifted velocities higher in the ordinate axis. *Down: Fig. 17 of Gomez & Cox (2002)*, synthetic Hα observation of the model along $\phi = \pi/2$, to be compared to the above. The solid line is the vertical velocity weighted with the square of the density for those grid zones with n< 0.01 cm^{-3}. The dotted line is the emission measure for the same positions. As the gas approaches the gaseous arm at 8.5 kpc, the flow rises to pass above it and then falls behind. Notice that the peak of the emission measure is upstream from the higher density gaseous arm in the midplane because of the forward lean of the arm at high z.

3.2 Galaxy Sample

The sample of galaxies is made from the LEDA database (Lyon-Meudon Extragalactic Database), where the selection criteria are: (i) low inclination angle (i$< 25°$); (ii) nearby ($v < 4000$ km s^{-1}); (iii) a well defined spiral morphological type (2<t<8); and (iv) diameter larger than 2 arcmin (D$_{25} > 2$). This information and other basic properties of the galaxy sample are summarized in Table 3.1.

Moreover, the galaxies are shown in Figures 3.2 to 3.5, where HST images are displayed together with the different slit positions. The bi-dimensional spectra corresponding to each slit are also plotted, in the spectral window that shows the emission of Hα and [SII] across the galactic disks. The reference point corresponds to the pixel where the three slits cut, the galactic center.

3.2.1 NGC 278

NGC 278 is an isolated (Bushouse, Werner & Lamb 1988) and almost face-on galaxy, part of the local supercluster of galaxies centred around the Virgo cluster (Vallee 1993). It is relatively small in the optical emission, with size of about $2'$ (Israel 2009) corresponding to a diameter of 7 kpc for a distance of ~ 12.1 Mpc (see Table 3.1). However in HI its diameter is five times larger (Knapen *et al.* 2004).

In optical images its morphology is that of a small, non-barred galaxy with a bright star forming nucleus and spiral arms. Its nucleus is not only quite bright in the Hα line, but also in the infrared continuum (Dale *et al.* 2000; Sanders *et al.* 2003) and the [CII] line (Malhotra *et al.* 2001) consistent with intense star-forming activity (Ho, Filippenko & Sargent 1995; Eskridge et al. 2002). However there is no indication of a low-luminosity AGN (Tzanavaris & Georgantopoulos 2007).

NGC 278 can be found in many recent works, but mostly forming part of surveys (e.g. Israel 2009). A specific study of this galaxy can be found in Knapen *et al.* (2004), who concluded that its appearance most likely reflects a recent minor merger. Asymmetries set up in the disk by this minor merger may well be the cause of the intense star formation in the inner region, which can be interpreted as a rare example of a nuclear ring in a non-barred galaxy. Rather than being induced by a bar, this nuclear ring would then be the direct result of an interaction event in the recent history of the galaxy. They also show a disturbed velocity field in its Hα kinematics, which may be partly the result of spiral density wave streaming motions. The HI emission, although faint, also shows disturbed morphology and kinematics.

3.2.2 NGC 1058

NGC 1058 is a nearly face-on spiral galaxy with an inclination angle in the range 4° to 11° (Petric & Rupen 2007). The distance to this galaxy is uncertain, ranging from 8.4 Mpc (Battinelli *et al.* 2000) to 14.5 Mpc (Sandage & Tammann 1974). We adopt a distance of 9.8 Mpc, given by a more recent work (Moustakas & Kennicutt 2006), for which $1''$ corresponds to 47.5 pc.

It has a clear knotty structure not organized into spiral arms (Battinelli *et al.* 2000), with a complete absence of any well defined-arms in Hα emission and a flocculent appearance of the innermost regions of the disk (Ferguson *et al.* 1995). These features are also observed in the HST image (Figure 3.3).

Radial metallicity and reddening gradients, both decreasing with the galactocentric distance, are found from studies of Hα emitting regions by Ferguson *et al.* (1998a,b), a trend often observed in spirals.

The HI velocity dispersion (ranging between 4 and 15 km s^{-1}) also decreases with radius, but the decline of starlight with radius is much steeper than that of the velocity dispersion (Petric & Rupen 2007). These authors find moreover that the HI velocity dispersion is not correlated with star formation or the spiral arms, so a global radial falloff must be explained in the context of significant local effects.

Battinelli *et al.* (2000) also found a steeper radial slope for the SFR in NGC 1058, with young star associations relatively small (peak at $\sim$ 50 pc), being the star formation clearly stronger in the central regions. From our long slit spectra, Figure 3.3, the Hα emission reveals however stronger emission in the outer than in the innermost regions.

Figure 3.2:

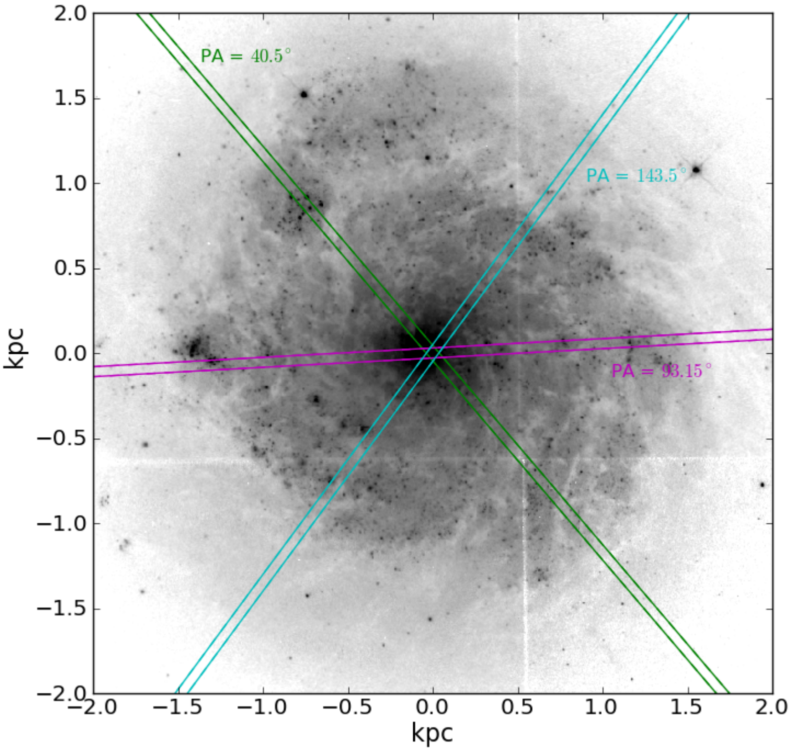

(a) HST image (WFPC2+F450W) of NGC 278; North is up and East to the left. The different slit positions of the long-slit spectra, taken with the red arm ISIS spectrograph attached to the 4.2m WHT, are also represented on the image with different colors.

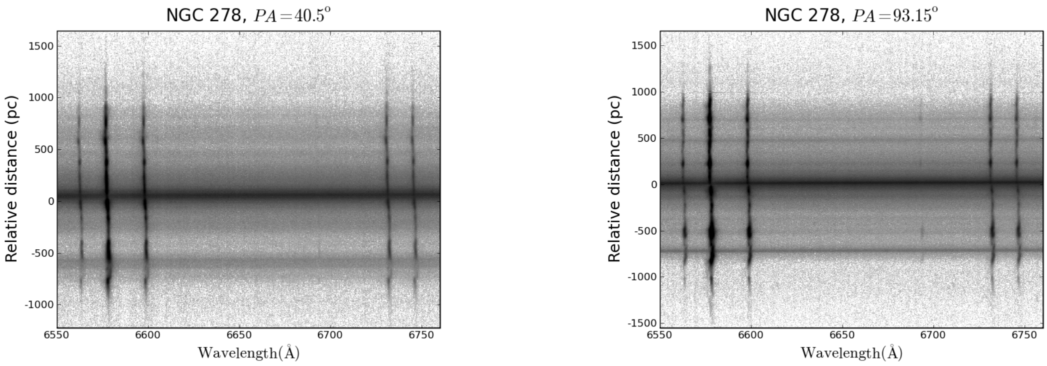

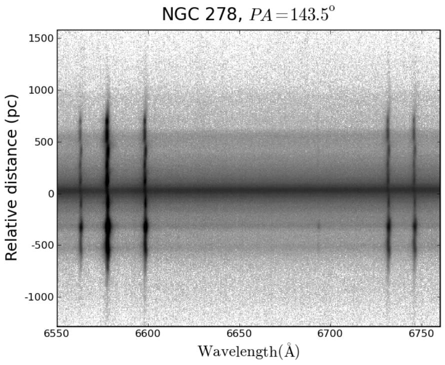

(b) The bi-dimensional spectra for each slit position. The Hα, [NII] and [SII] emission are observed.

Figure 3.3:

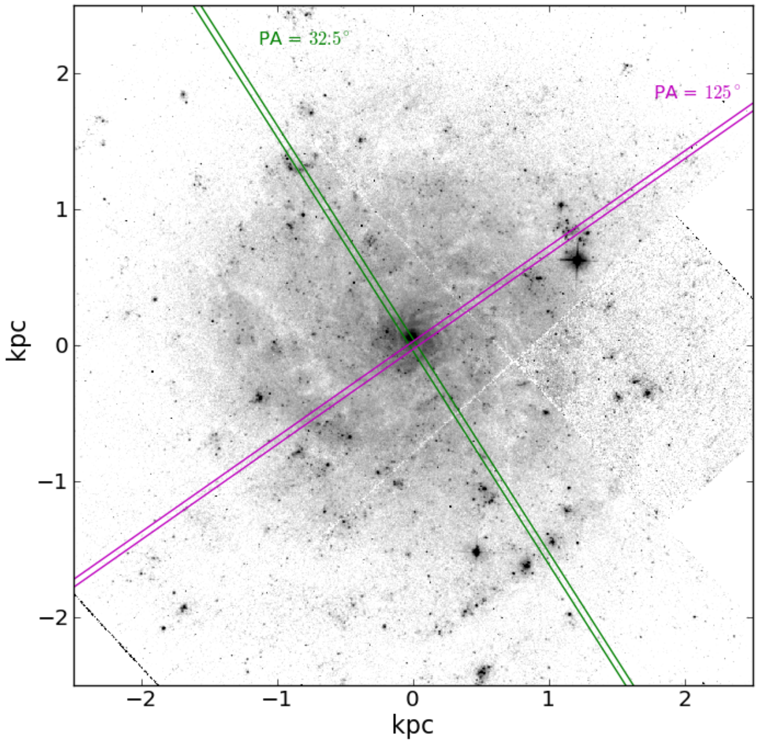

(a) HST image (WFPC2+F450W) of NGC 1058, North is up and East to the left, and the different slit positions represented with different colors.

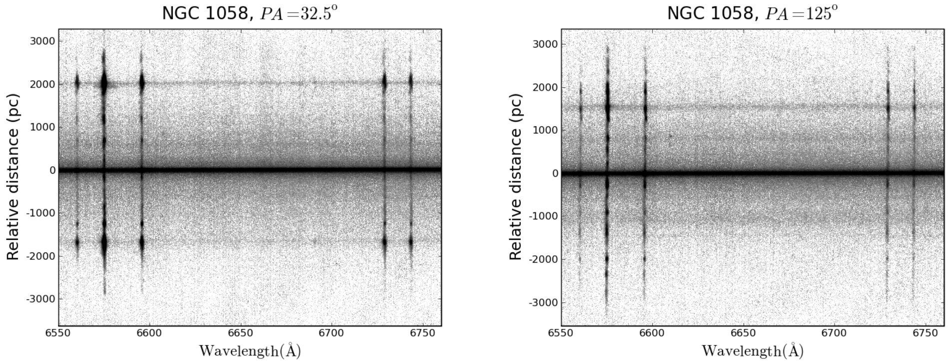

(b) The bi-dimensional red spectra (showing the Hα, [NII] and [SII] emission) for each slit position.

3.2.3 UGC 3574

UGC 3574 is a nearby late-type spiral galaxy, with low inclination; at a distance of 21.8 Mpc (James *et al.* 2004) is the furthest galaxy of the sample. The optical image shown in Figure 3.4, taken with the Palomar 48-inch Schmidt telescope[1], is of low resolution and therefore many spatial details are lost. Two faint spiral arms can be distinguished, while the stronger emission comes from the nuclear region and some very compact and clumpy sources at the end of the southern spiral arm or across the northern one.

No specific studies for this galaxy are found in the literature, but it is included in many surveys for different purposes, e.g. Böker *et al.* (2002) who study the nuclear star clusters in late-type spiral galaxies. In the latter work, UGC 3574 is characterized as having a "naked" nuclear cluster in the I-band WFPC2 image, forming a distinct and isolated entity within the disk and without any signs of a kinematic center.

3.2.4 NGC 2500

NGC 2500 belongs to a quartet of galaxies (Sandage & Bedke 1994). Epinat *et al.* (2008) find diffuse Hα emission in their observed Hα maps, in agreement with James *et al.* (2004), where its short bar is almost aligned with its minor kinematical axis. As in the case of UGC 3574, there are not individual works for this galaxy, mainly found as part of surveys, e.g. Epinat *et al.* (2008) or James *et al.* (2004).

In the HST/WFPC2+F450W image, Figure 3.5, it is observed that the star formation is mainly concentrated in the nuclear region and its well defined, northern spiral arm. The southern arm is fainter and, globally, the southern region of this galaxy appears more flocculent.

3.3 Observations and data reduction

We obtained long-slit spectroscopy with the double arm ISIS spectrograph attached to the 4.2m William Herschel Telescope (WHT), at the Roque de los Muchachos Observatory

---

[1] NASA/IPAC EXTRAGALACTIC DATABASE, reference code 1994DSS...1...0000

Figure 3.4:

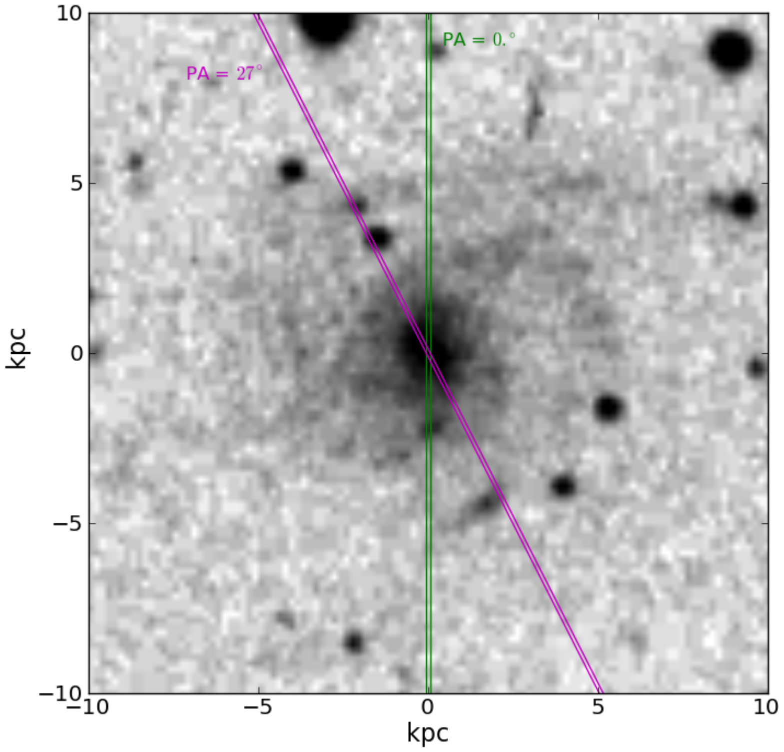

(a) Image of UGC 3574, taken with the Palomar 48-inch Schmidt telescope. North is up and East to the left. The two slit positions are represented with different colors.

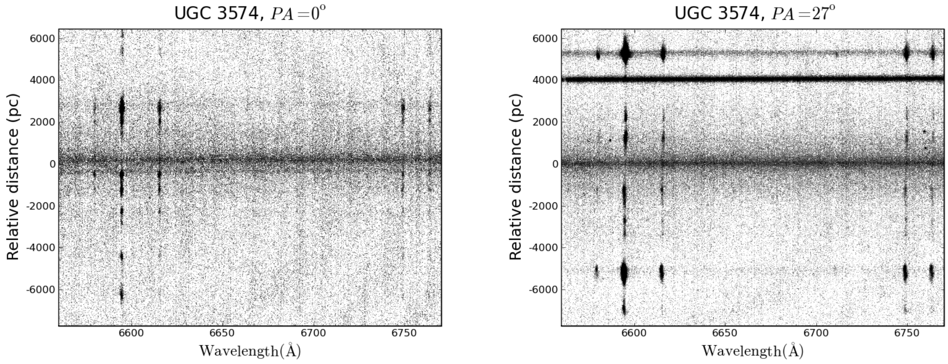

(b) The bi-dimensional red spectra (showing the Hα, [NII] and [SII] emission) for each slit position.

Figure 3.5:

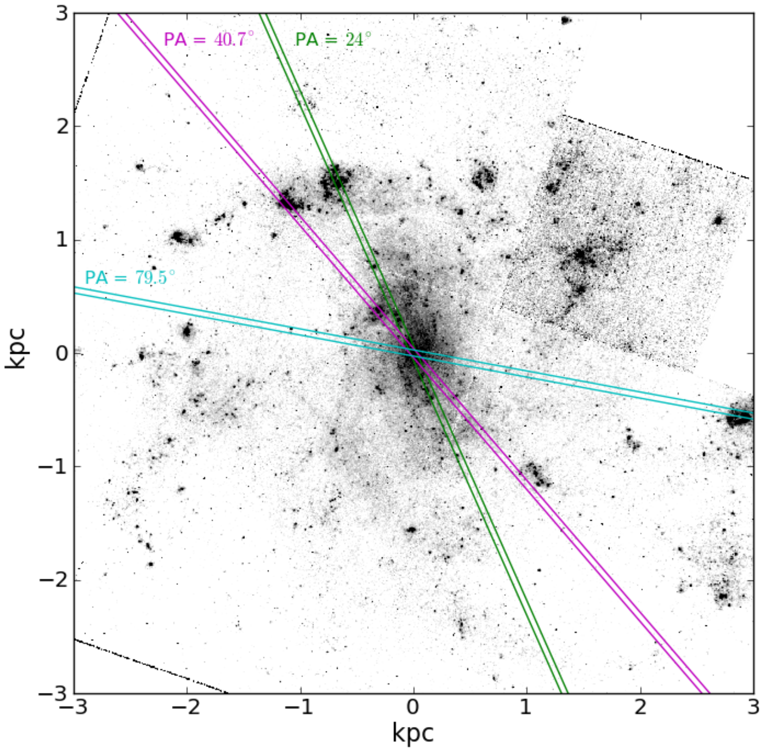

(a) HST image (WFPC2+F450W) of NGC 2500; North is up and East to the left. Similarly to the rest of galaxies, the different slit positions are also represented on the image with different colors.

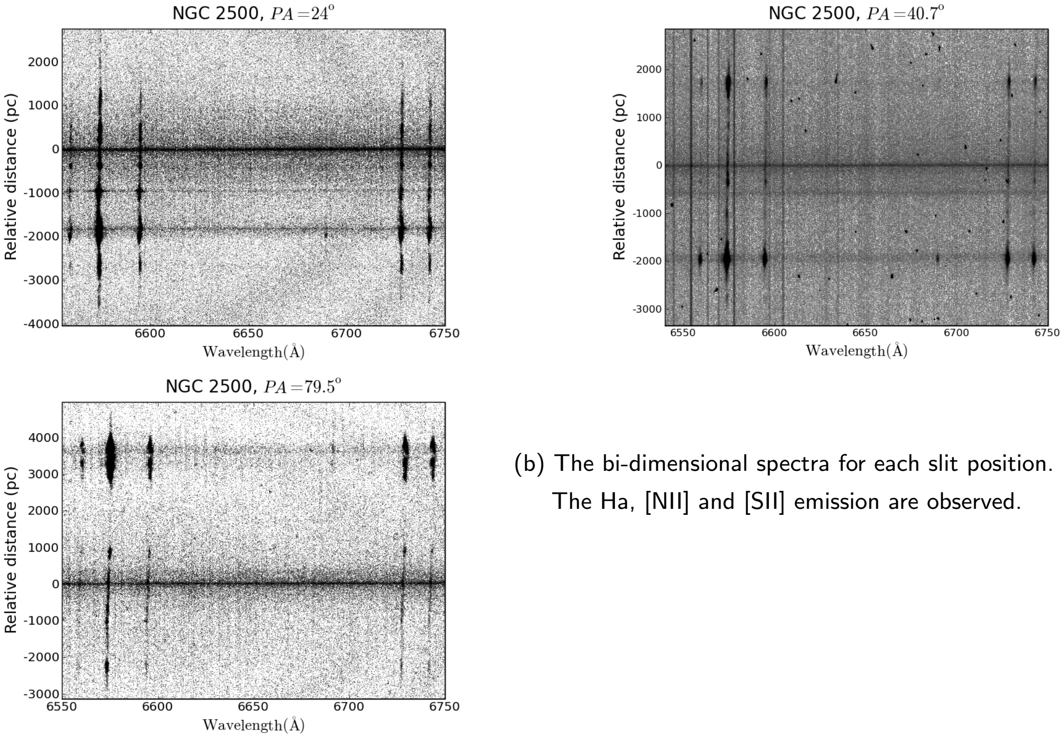

(b) The bi-dimensional spectra for each slit position. The Ha, [NII] and [SII] emission are observed.

Table 3.1: Galaxy Parameters[a]

Galaxy	RA (J2000) h m s	Dec. (J2000) ° ′ ″	Type	Redshift	Dist.[b] (Mpc)	Inclin.[c] (deg)	Dimensions (arcmin)	M_B
NGC 278	00 52 04.3	+47 33 02	SAB(rs)b	0.002090	12.1	21	2.1×2.0	11.47
NGC 1058	02 43 30.0	+37 20 29	SA(rs)c	0.001728	9.8	6	3.0×2.8	11.82
UGC 3574	06 53 10.4	+57 10 40	SA(s)cd	0.004807	21.8	19	4.2×3.6	13.2
NGC 2500	08 01 53.2	+50 44 14	SAB(rs)d	0.001715	11.0	41	2.9×2.6	12.20

[a] Sourced from *NASA Extragalactic Database*
[b] Moustakas & Kennicutt 2006; except for UGC 3574, James *et al.* 2004
[c] Epinat *et al.* 2008.

(La Palma) during December 2003. This instrument consists of two intermediate dispersion spectrographs operating simultaneously, separating the blue and red spectral regions, which are imaged onto an EEV12 and a MARCONI2 CCD chips respectively. In this way we have two spectral ranges observed simultaneously, a blue one centered around Hβ (4861 Å), and a red one around Hα (6563 Å). The gratings used, R1200R and R600B, provide a dispersion of 0.23 and 0.45 Å/pixel respectively. The slit width of 1 arcsec projects onto about 3.64 pixels Full-Width-Half-Maximum (FWHM) on the detector; the spatial sampling along the slit is 0.2 arcsec/pixel. The slit was placed at two or three different position angles for each galaxy (Table 3.2).

The reduction process is the same as that outlined in Chapter 2. The spectra were reduced and calibrated following the standard procedure. Bias subtraction, flat-fielding, wavelength and flux calibration were done with the IRAF[2] task `ccdproc`. For the wavelength calibration CuNe + CuAr lamps were used. The standard stars Feige 34, g191b2b, gd248, gd50 and hz21 from the Oke (1990) catalogue were used for flux calibration. Sky subtraction was done using the IRAF NOAO package task `background`. For each wavelength range, the different exposures at each slit orientation were combined, eliminating cosmic rays and bad pixels, thus obtaining the final spectra.

We fit the Hα emission line with a Gaussian at each pixel along the slit. Line flux, FWHM, central wavelength, and their corresponding errors, are calculated with the

---

[2] IRAF is distributed by the National Optical Astronomy Observatory, which is operated by the Association of Universities for Research in Astronomy (AURA) under cooperative agreement with the National Science Foundation

Table 3.2: Journal of observations

Galaxy	Date	P.A. (deg)	Wavelength range (Å)	Exposure time (s)	Slit (″)	Airmass
NGC 278	15.12.2003	40.5, 93.15, 143.5	6034−7088	3×1200	1.03	1.06 - 1.33
NGC 2500	15.12.2003	24, 79.5, 40.7	6034−7088	2,3×1200	1.03	1.08 - 1.14
NGC 1058	16.12.2003	32.5, 125	6034−7088	3×1800	1.03	1.01 - 1.17
UGC 3574	16.12.2003	0, 27, 122	6034−7088	3×1200; 2,3×1800	1.03	1.14 - 1.28

STARLINK[3] package DIPSO. The continuum level is simultaneously fitted with a first order polynomial. Following the same process as in Chapter 2

3.4 V$_Z$ calculation. Preliminary results.

In the case of face-on galaxies the vertical component of the disk velocity field should be obtained straightforward. As our sample galaxies are nearly face-on, the observed velocity is the result of the sum of several projected velocity components, due to their inclination angle. This sum can be summarized as the vertical component to the disk plus its parallel component. We assume then that the observed velocity can be expressed in terms of

$$\begin{aligned} V_{obs} &= V_{sys} + V_{\|}\sin i + V_{\perp}\cos i = \\ &= V_{sys} + (V_{rot}\cos\theta + V_{exp}\sin\theta)\sin i + V_Z\cos i \end{aligned} \quad (3.1)$$

where V$_{sys}$ is the systemic velocity of the galaxy, V$_{rot}$ and V$_{exp}$ the rotational and expansion velocity respectively, at the plane of the disk, and V$_Z$ is the vertical velocity component; θ is the angle in the plane of the galaxy (counterclockwise from the major axis), and i is the inclination angle of the galaxy disk.

We consider the x-axis as our zenith in the plane of the sky, and X-axis coincides with the major axis in the plane of the galactic disk. Then, the polar coordinates in the plane of the sky, (r,ϕ), and in the plane of the galaxy, (R,θ), are related as follows:

$$R = r\sqrt{\cos^2(\phi - PA) + \sin^2(\phi - PA)\cos^{-2} i} \quad (3.2)$$

$$R\cos\theta = r\cos(\phi - PA) \quad (3.3)$$

$$R\sin\theta = r\sin(\phi - PA)\cos^{-1} i \quad (3.4)$$

---

[3] http://star-www.rl.ac.uk/star/docs/sun50.htx/sun50.html

From equation 3.1, neglecting the expansion velocity in equation 3.1 (this is, assuming $v_{exp} = 0$) and applying the relations between the celestial coordinates (equations 3.2 and 3.3), the vertical velocity component can be expressed as:

$$\begin{aligned} V_Z &= \left(V_{obs} - V_{sys} - V_{rot}\frac{r}{R}\cos(\phi - PA)\sin i\right)\cos^{-1} i = \\ &= \left(V_{obs} - V_{sys} - V_{rot}\frac{\sin i}{\sqrt{1 + \tan^2(\phi - PA)/\cos^2 i}}\right)\cos^{-1} i \end{aligned} \quad (3.5)$$

Data for the rotation curves, the inclination angle and the PA of the line of nodes for each galaxy are taken from Epinat *et al.* (2008), see Table 3.1. But these rotation curves were fitted using a different parametric model than these authors, we use the parametric model of Giovanelli & Haynes (2002) (as for NGC 6946 in Chapter 2),

$$V_{pe}(r) = V_0(1 - e^{-r/r_{pe}})(1 + \alpha\, r/r_{pe}) \quad (3.6)$$

where V_0 regulates the overall amplitude of the rotation curve, r_{pe} yields a scale length for the inner steep rise, and α sets the slope of the slowly changing outer part. After a least square fit of this model to the data, the parameters obtained for each galaxy are summarized in Table 3.3.

Table 3.3: Parameters from the rotation curve fit for each galaxy.

Galaxy	V_0 (km s^{-1})	r_{pe} (arcsec)	α	R (correlation)
NGC 278	219.73±59.1	1.08±0.36	-0.40±0.17	0.907
NGC 1058	74.5±12.7	0.16±0.10	0.05±0.03	0.668
UGC 3574	155.5±18.5	1.29±0.31	0.024±0.017	0.916
NGC 2500	55.9±3	0.40±0.53	0.04±0.007	0.872

** The rotation curve has been fitted by a least squares fit, following the parametric model of Giovanelli & Haynes (2002): $V_{pe}(r) = V_0(1 - e^{-r/r_{pe}})(1 + \alpha\, r/r_{pe})$.

Figure 3.6 shows the observed and vertical velocities, V_{obs} and V_Z, for NGC 278. Top panels show the observed radial velocities together with the fitted rotation curve, to be subtracted from the latter, and for each position angle. The resulting vertical components of the velocity, equation 3.5, are represented versus galactocentric distance at each position angle (with different color code) along the slit in the middle panels; zero marks the galactic center position. The Hα emission line flux is also plotted, with the aim of looking for some relation or correlation between the velocity and flux peaks.

As the rotational velocity is fitted with least squares, $V_{rot} = V(R) + e_{rot}$, the errors in the fitting can be clearly observed in some cases, middle panels of Fig. 3.6, where the rotational residues are not completely removed. So, what it is actually being represented is

$$\Big\{V_{obs} - V_{sys} - V(R)f(\phi, PA)\sin i\Big\}\cos^{-1} i = e_{rot}f(\phi, PA)\tan i + V_Z \tag{3.7}$$

where $f(\phi, PA) = (1+\tan^2(\phi-PA)/\cos^2 i)^{-\frac{1}{2}}$. The left hand side of the above equation, that we assume as V_Z, is then an approximation of the actual perpendicular component. To remove this effect, the vertical velocity component has been detrended, ΔV_Z, by fitting a linear component to the gentle rise for each rotation curve side, the approaching and the receding. Therefore, the global trend from the rotational residues is removed, remaining only the local fluctuations or oscillations of the vertical velocities.

$$\Delta\Big\{V_{obs} - V_{sys} - V(R)f(\phi, PA)\sin i\Big\}\cos^{-1} i \simeq V_{Zactual} \tag{3.8}$$

This analysis is done for the rest of galaxies, Figures 3.7, 3.8, and 3.9 show the variations of the vertical velocity component across the disk, through the spiral arms and for different slit positions. In many cases a remarkably well-defined wavelike structure is clear.

Analyzing the detrended vertical velocities ΔV_Z for NGC 278, bottom panels of Fig. 3.6, we find the same kinematical behaviour than that found by Alfaro *et al.* 2001 in NGC 5427. A systematic displacement between the velocities and the emission line peaks, where the approaching (negative values) peaks of ΔV_Z occur in the convex border of the arms, and the receding maxima (positive values) are located behind the Hα emission maxima, in the concave side. This kinematical behavior is similar to the response of a gas flow into a spiral density wave in a thick and magnetized gaseous disk, described by the Martos & Cox (1998) and Martos *et al.* (1999) galactic bore models.

A remarkable feature is found in the slit position PA=143.5°, where a strong vertical velocity peak at ~ 0.8 kpc from the galactic center is related with a very faint Hα emission peak. As it weren't associated with a spiral arm. At this slit position however it is observed that the Hα emission is weaker in one side (positive distances from the center) than in the other. The other two slits have both sides with similar Hα intensities.

The kinematical relation described above, between the vertical velocities and the Hα emission peaks, can be also found in NGC 1058 (Fig. 3.7). In this case the vertical displacements of the velocity seem to be smaller than in NGC 278, in the majority of order 10 km s^{-1}, with some peaks no bigger than 15 km s^{-1}. The vertical displacement appears more continuously, with a more sinusoidal wave like aspect than for NGC 278.

It seems than this kinematical relation is more associated with the encounter with a spiral arm, than with its intensity. Such as it can be observed from these two last galaxies, the magnitude order of the vertical displacements, V_Z, is not related with the Hα intensity emission.

The other two galaxies of the sample do not show so clearly this kinematical behaviour.

The Hα emission line was fitted pixel by pixel across the slits for NGC 278 and NGC 1058, however in NGC 2500 and UGC 3574 there are some regions with no Hα emission or where it was too faint to be fitted, see Figures 3.8 and 3.9. This is more noticeable in UGC 3574, loosing therefore a global view of the vertical velocity deviations, that only can be discerned, with respect the Hα emission peaks. So, V_Z has not been detrended for this galaxy.

For NGC 2500 this discontinuity in the Hα emission line fit is not so extreme. There are only small gaps in the Hα fit, for the slit positions of 40.7° and 79.5°, but the V_Z structure can be clearly distinguished.

However, we find in the slit with PA=24°, where the Hα emission line is fitted continuously pixel by pixel along the slit, that the relation between V_Z, or ΔV_Z, with the Hα emission peaks does not seem to hold as for NGC 278 and NGC 1058. The clearest features differing are the most negative peak (approaching peak) of ΔV_Z, at a distance of ~ -1.8 kpc, that occurs in the concave side of the arms, instead of appearing in the convex border. And its preceding positive peak of ΔV_Z (receding peak) is located in front of a Hα emission maxima, not behind.

In the other two slits, with PA=40.7° and 79.5°, the central regions do not show neither a clear structure of ΔV_Z, between distances of -1.8 to 1.5 and -2.5 to 2.5 kpc respectively.

In this regions the Hα emission is much more fainter than in the extremes, the error bars are therefore bigger, and we also find gaps in the Hα emission line fit.

In the ends of these two slits the ΔV_Z structure is clearer and its relation with the Hα emission peaks. But we find that for the slit with PA=40.7° such relation is more similar with that of PA=24°, differing with the galactic bore model of NGC 278 and NGC 1058.

Only in the slit with PA= 79.5°, between distances of $\sim$ 2.8 to 4.2 kpc, this kinematical relation seems to agree with the latter.

This part of the work is still in an analysis stage, and more study about the kinematical properties of these galaxies is required before trying to give any firm conclusion or result.

3.5 Diagnostic Diagrams

A brief introduction about the Diagnostic Diagrams (DD) can be found in Section 2.5 of previous Chapter 2. To complete the kinematic analysis in this chapter, DD are included to determine the ionizing mechanisms in the observed features. The ionization and excitation process can be determined by diagnostic of ratios of [NII]/Hα versus [OIII]/Hβ, depending on its location in such diagrams (Baldwin, Philips & Terlevich 1981).

As Hβ and [OIII] data are available, the blue spectra, [NII]/Hα versus [OIII]/Hβ can be plotted, as one of the best options among all the possible emission line ratios (Veilleux & Osterbrock 1987), and therefore one of the most commonly and widely used DD.

In any case, both this DD and that used for NGC 6946, [SII]/Hα versus [NII]/Hα, are applied for determining the excitation mechanism. They are found in Figure 3.10 for each galaxy. The color code is the same as in previous Figures 3.6 to 3.9, for clarity and coherence.

Moreover, thanks to the availability of Hβ data, the flux ratios are corrected from reddening following the relation

$$\frac{I_{H\alpha}}{I_{H\beta}} = \frac{F_{H\alpha}}{F_{H\beta}} \times 10^{0.4(A_{H\alpha}-A_{H\beta})} = \frac{F_{H\alpha}}{F_{H\beta}} \times 10^{0.4A_V(k_{H\alpha}-k_{H\beta})} \tag{3.9}$$

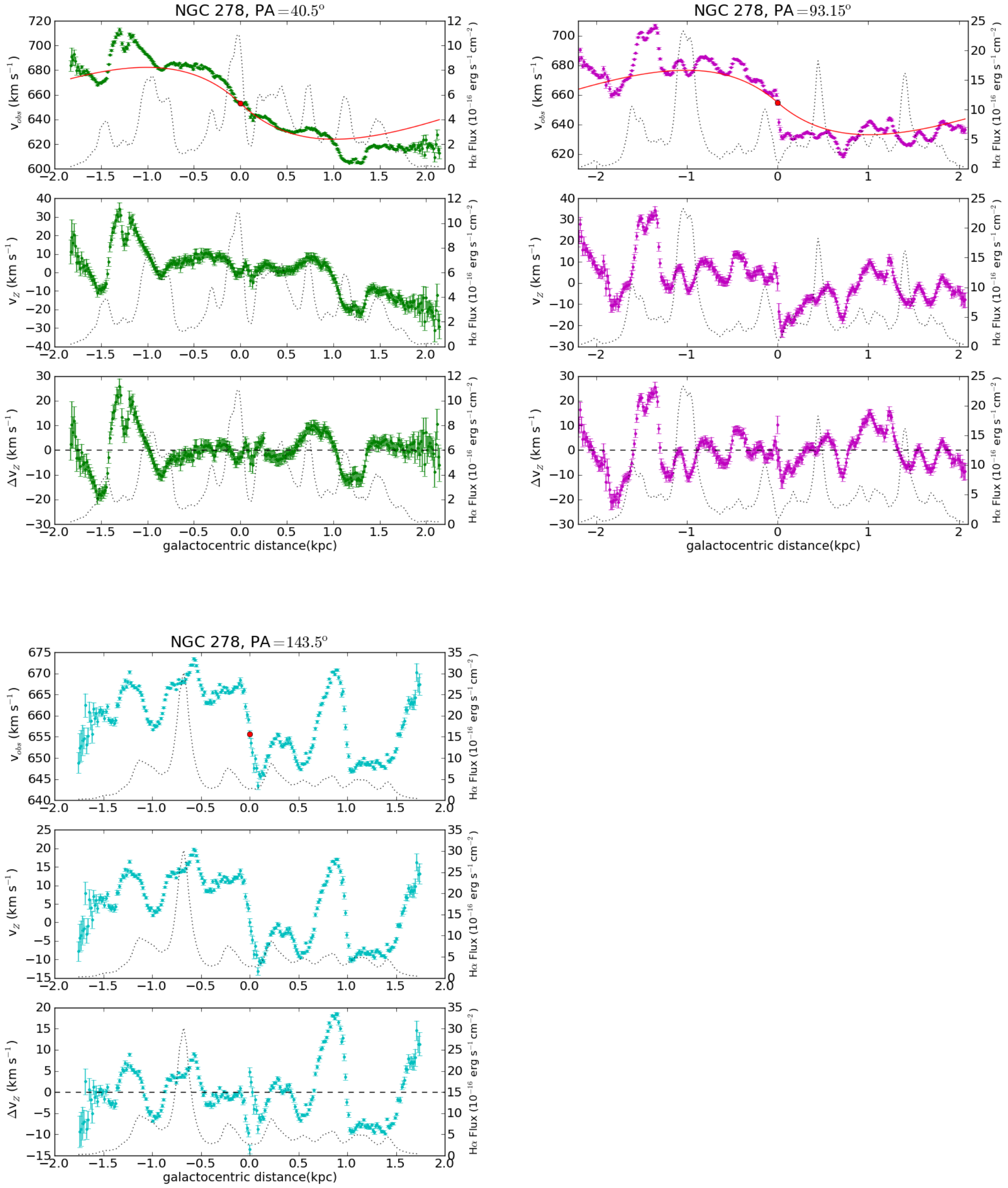

Figure 3.6: NGC 278, for the three slits positions. *Top panels:* The observed velocities for NGC 278, derived from the Hα emission lines (see Section 3.3). The red line corresponds with the projected rotation curve, and the red dot marks the systemic velocity. The Hα intensity is drawn in the right-hand ordinate, with a dotted line. The *x-axis* represents the distance to the reference pixel, in kpc units; *Middle panels:* The perpendicular velocity V_Z, at each pixel position across the slit, calculated as Equation 3.5; *Top panels:* The detrended perpendicular velocity, after fitting a linear component to the global trend. A dashed line marking the zero value emphasizes that the global trend has been practically removed, remaining only the local oscillations of V_Z.

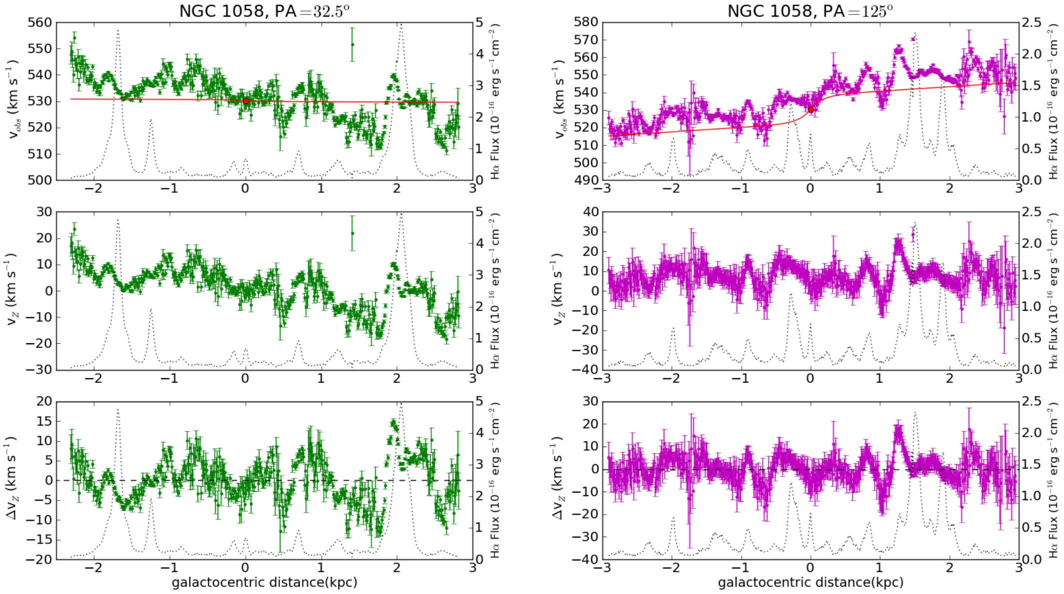

Figure 3.7: NGC 1058, PA $= 32.5°$. *Top panels:* The observed velocities for NGC 1058, derived from the Hα emission lines (see Section 3.3). The red line corresponds with the projected rotation curve, and the red dot marks the systemic velocity. This PA slit position is very close to the minor axis and the rotation curve projection appears to be rather constant, equal to the V$_{sys}$, since the rotational velocity is negligible. The Hα intensity is drawn in the right-hand ordinate, with a dotted line. The *x-axis* represents the distance to the reference pixel, in kpc units; *Middle panels:* The perpendicular velocity V_Z, at each pixel position across the slit, calculated as Equation 3.5; *Bottom panels:* The detrended perpendicular velocity after fitting a linear component to the global trend, residuals still from the fits of the rotational velocity. The removal of such global trend can be checked by just comparing with the central plot.

where I_λ is the un-reddened emission at a certain wavelength from the source, and F_λ is the observed flux, affected by dust absorption. $A_\lambda = k_\lambda A_V$ is the extinction factor at a particular waveband λ, and k_λ and A_V are the extinction curve and the absorption in the V band respectively. A detailed explanation of the reddening and its correction is described in Chapter 5. The Balmer decrement is a way for reddening correction, deduced from the comparison of the observed Hα to Hβ flux ratio with the theoretical value of 2.86 (Osterbrock 1989), based on case B recombination. Applying the Balmer decrement we have that,

$$A_V = \frac{log(2.86) - log(F_{H\beta}/F_{H\alpha})}{0.4(k_{H\alpha} - k_{H\beta})} \tag{3.10}$$

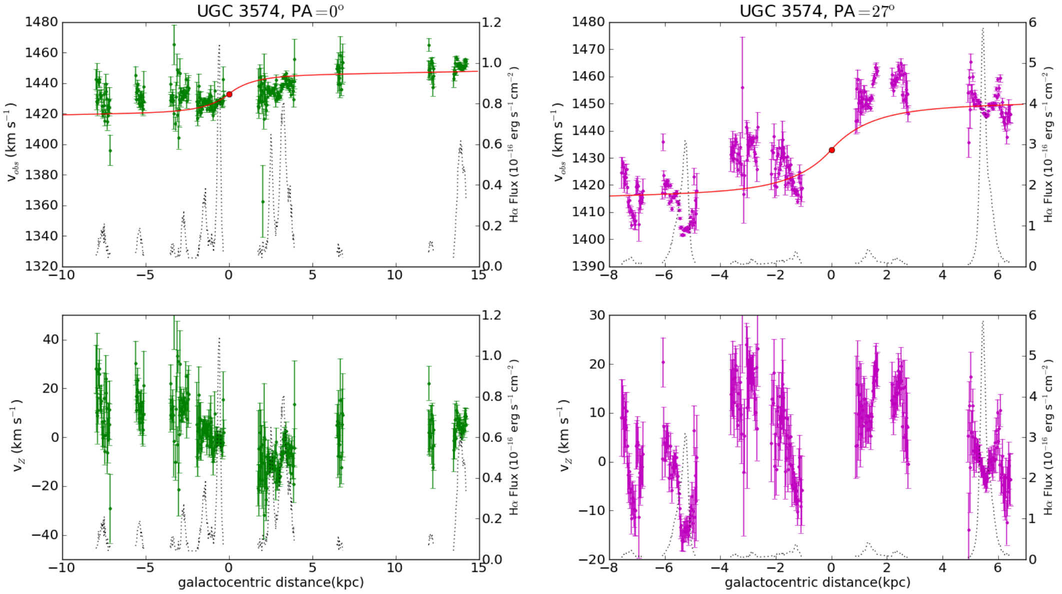

Figure 3.8: *Top panels:* The observed velocities for UGC 3574, derived from the Hα emission lines (see Section 3.3). The red line corresponds with the projected rotation curve, and the red dot marks the systemic velocity. For this galaxy only some regions of the slit were fitted, due to its fainter emission as it can be clearly observed in Figure 3.4. The Hα intensity is drawn in the right-hand ordinate, with a dotted line. The *x-axis* represents the distance to the reference pixel, in kpc units; *Bottom panels:* The perpendicular velocity V_Z, calculated as Equation 3.5, is only represented where it was possible to fit the Hα emission line.

So, the unreddened flux ratios can be obtained as

$$
\begin{aligned}
log\left(\frac{I_{\lambda 1}}{I_{\lambda 2}}\right) &= log\left(\frac{F_{\lambda 1}}{F_{\lambda 2}}\right) + 0.4A_V(k_{\lambda 1} - k_{\lambda 2}) = \\
&= log\left(\frac{F_{\lambda 1}}{F_{\lambda 2}}\right) + C_1 log\left(\frac{F_{H\alpha}}{F_{H\beta}}\right) - C_2
\end{aligned}
\tag{3.11}
$$

where $C_1 = \frac{k_{\lambda 2} - k_{\lambda 1}}{k_{H\alpha} - k_{H\beta}}$, and $C_2 = log(2.86)C_1$.

From Figure 3.10 we can deduce that photoionization, from high energetic photons, is the main ionization mechanism. Although there is a small portion of the gas that appears to be ionized by low-velocity shocks. In NGC 1058, for the slit with PA$= 125°$, this portion is more important.

Two clear different patterns appear in the [NII]/Hα versus [OIII]/Hβ diagnostic

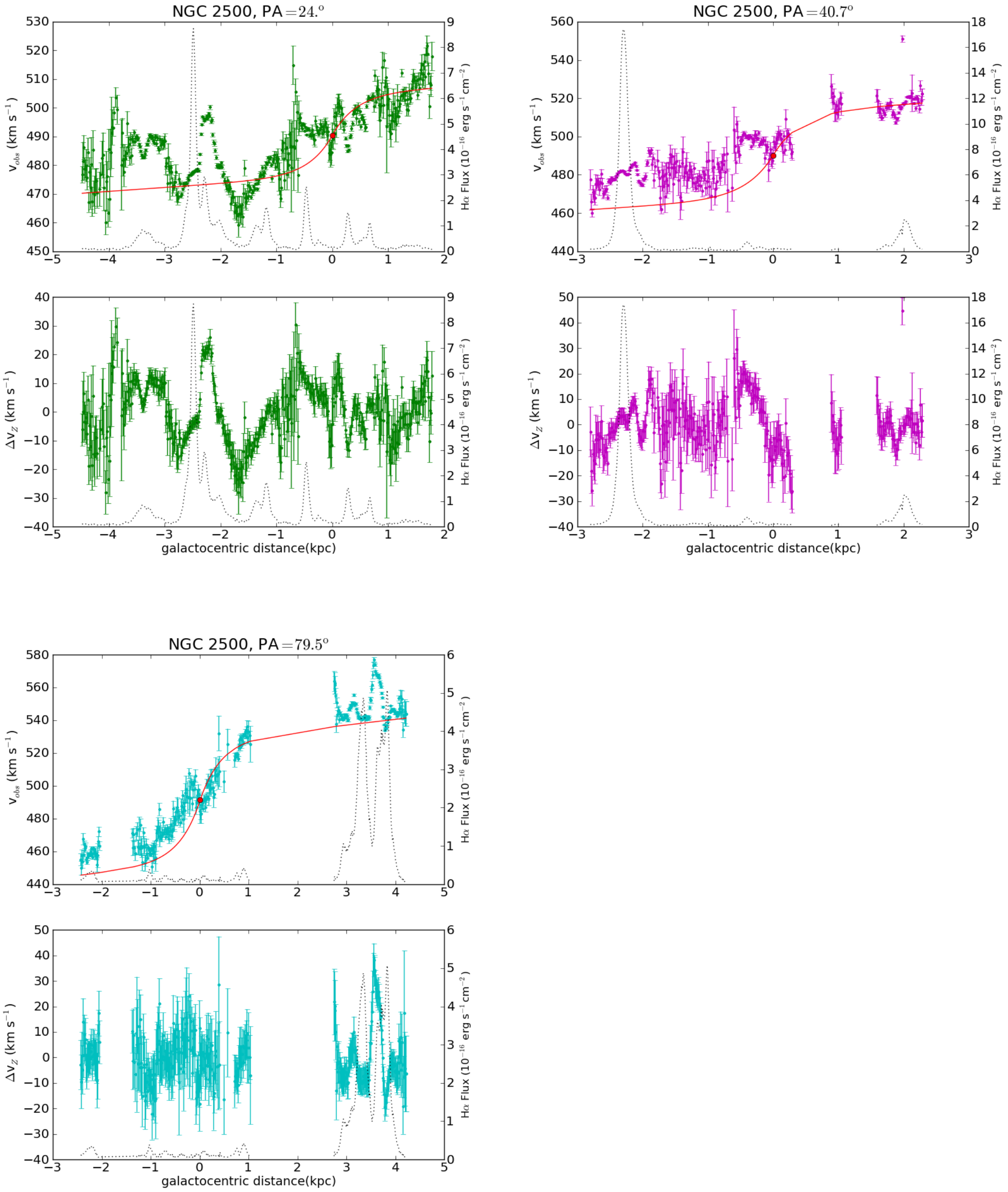

Figure 3.9: *Top panels:* The observed velocities for NGC 2500, derived from the Hα emission lines (see Section 3.3). The red line corresponds with the projected rotation curve, and the red dot marks the systemic velocity. The Hα intensity is drawn in the right-hand ordinate, with a dotted line. The *x-axis* represents the distance to the reference pixel, in kpc units; *Bottom panels:* The detrended perpendicular velocity ΔV_Z, at each pixel position across the slit, calculated as Equation 3.5

diagrams. NGC 278 and NGC 1058 have all their pixels, for the three slit positions, concentrated at the same location in the DD. Whereas for NGC 2500 and UGC 3574 each slit position occupies a different location in the DD, nearly covering the theoretical curve separating the different ionization mechanisms, as metallicity gradient.

It should be interesting to analyze how the kinematical behaviour found in last section, between the vertical velocities V_Z location respect the Hα emission peaks (coinciding with a galactic bore model or not), is related with these two patterns in the DD. Since those galaxies where the kinematical behaviour clearly coincided with a galactic bore model, NGC 278 and NGC 1058, occupy the same location in the DD clearly differentiate from the other two galaxies, NGC 2500 and UGC 3574, where such kinematical relation can not be established.

3.6 Summary

The existence of corrugations has been already reported, e.g. Alfaro *et al.* (2001), Matthews & Uson (2008). In this work not only the existence of radial and azimuthal corrugations are clearly observed, we report a first systematic study on the velocity corrugations in a sample of nearly face-on spiral galaxies.

Corrugations are closely linked, as cause/effect, to the large scale star formation processes: density waves, tidal interactions, galactic bores, collisions of high velocity clouds with the disk, etc. Which mechanism is the origin of disk corrugations is still an open problem.

A first stage of the analysis of our data set and the results is presented. These first results are:

NGC 278 and NGC 1058 show a similar behavior to NGC 5427 (Alfaro *et al.* 2001), with a clear displacement between the velocities and emission line peaks. Where the approaching (negative values) peaks of $_Z$ occur in the convex border of the arms, and the receding maxima (positive values) are located behind the Hα emission maxima, in the concave side. This kinematical behavior is similar to the one expected in a galactic bore generated by the interaction of a spiral density wave with a thick gaseous disk.

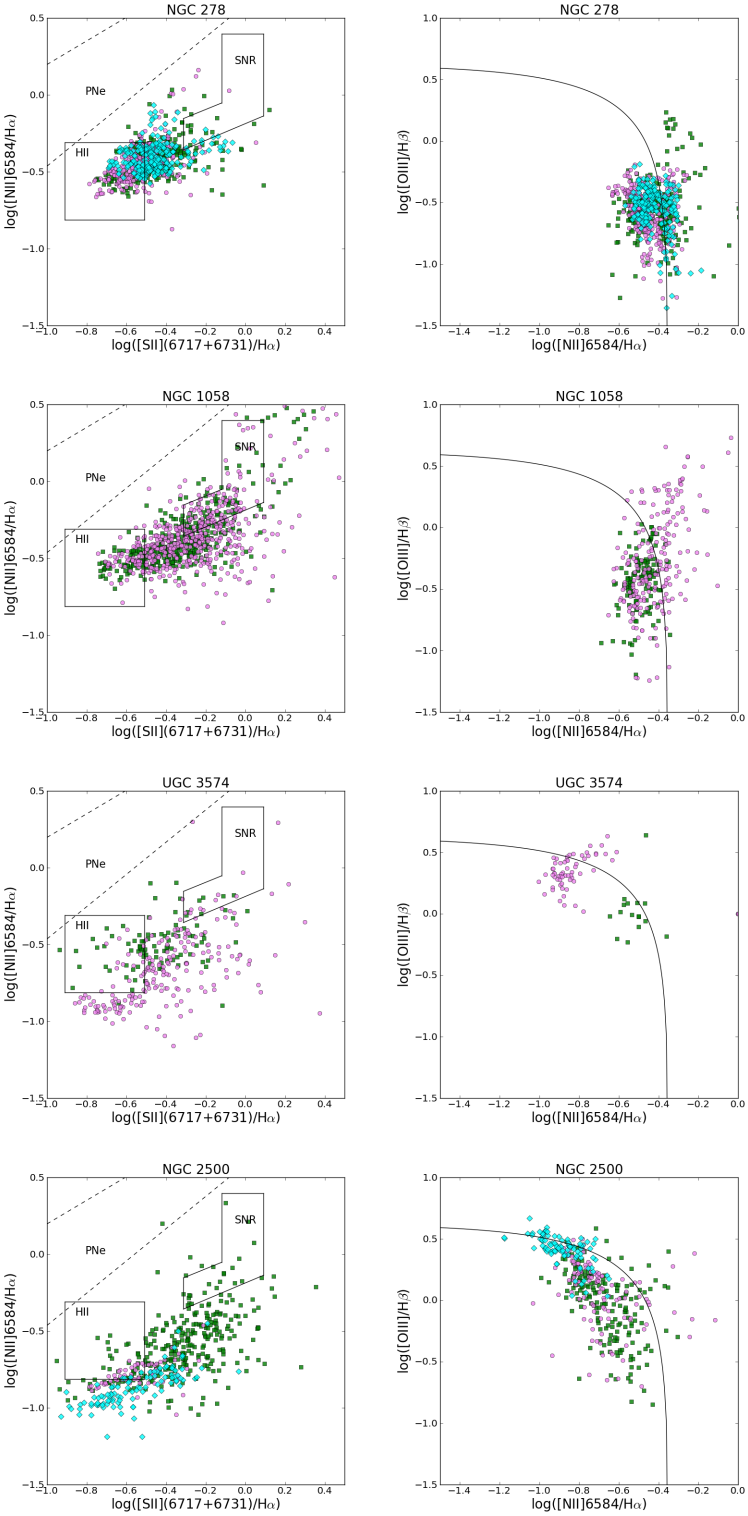
NGC 278
NGC 278
NGC 1058
NGC 1058
UGC 3574
UGC 3574
NGC 2500
NGC 2500

Figure 3.10: Diagnostic Diagrams for the four galaxies of the sample, following the same diagrams that in the case of NGC 6946, [SII]/Hα vs. [NII]/Hα, on the left, and on the right the most commonly used [NII]/Hα vs. [OIII]/Hβ diagram (Veilleux & Osterbrock 1987). The color code is the same followed across the whole chapter: NGC 278, PA=40.5° in green, PA=93.15° in magenta and PA=143.5° in cyan; NGC 1058, PA=32.5° in green and PA=125° in magenta; UGC 3574, PA=0° in green and PA=27° in magenta; NGC 278, PA=24° in green, PA=40.7° in magenta and PA=79.5° in cyan. For both diagrams the photoionization appears to be the main ionizations mechanism, although with some regions of low velocity shocks.

Whereas NGC 2500 and UGC 3574 do not show such a clear relation between the velocity and emission line peaks. This may be an observational bias be due to a fainter Hα emission and discontinuous line fit.

We also obtain the same differentiation among the galaxies, NGC 278 and NGC 1058, on the one hand, and NGC 2500 and UGC 3574, on the other, in their ionization behavior in the DD.

In NGC 278, the PA=143.5° slit has a quite strong ΔV_Z peak in a weak Hα emission zone. This could be associated with the co-rotation.

This part of the thesis work is still in progress, and more analysis is required, such as the study of the correlations between the velocity and the flux peaks. As well as the case of the galaxies NGC 2500 and UGC 3574, that do not show clearly the same pattern as NGC 278, NGC 1058 or NGC 5427, of a galactic bore from the effect of density waves crossing the galactic disk. It is not clear yet if it is a biased effect due to the lack of information or an actual different mechanism.

4

Age Patterns in a sample of spiral galaxies

Contents

4.1 Introduction 82

4.2 Sample and Data 84

4.2.1 Galaxy Selection 84

4.2.2 Data Reduction 85

4.2.3 Age Calibration 89

4.3 Age Maps 92

4.3.1 M74 (NGC 628) 94

4.3.2 IC 2574 96

4.3.3 M100 (NGC 4321) 97

4.3.4 M94 (NGC 4736) 98

4.3.5 M63 (NGC 5055) 100

4.3.6 M51 (NGC 5194) 102

4.4 Reliability and Robustness 103

4.4.1 Lowest Threshold Pixel Mass for a Fully Sampled IMF 104

4.4.2 Spatial Binning Scale 105

4.4.3 Metallicity and IMF Variation 107

4.5 Discussion and Summary 108

4.1 Introduction

The origin and persistence of spiral structure in galaxies is still largely an open question, although several plausible alternatives have been hypothesised. In some cases, spiral structure has variously been attributed to tidally influences of companions, a central rotating bar, or orbiting dark matter clumps (e.g. Bottema 2003; Dubinski *et al.* 2008). Alternatively, spirals density waves may be self-excited, either through quasi-steady global modes of the underlying disk (Lin & Shu 1964; Bertin & Lin 1996), or as short-lived, recurrent transient patterns from self-gravitational instabilities (Toomre 1964, 1990; Sellwood & Carlberg 1984). Central to all these hypotheses is the need distinguish between transient and ongoing star-formation on the very small scales ($<$ 1 kpc).

Spatial variation in the current star formation rates (SFR) and star formation history (SFH) across a galaxy can provide vital clues to its dynamical and secular evolution. Grebel (2000) finds that galaxy mass and environment are important factors in determining SFH, and finds a diversity of star formation and enrichment histories among galaxies of the Local Group, even for galaxies with the same morphological type. The most common star formation diagnostics use far ultraviolet (FUV), far-infrared (FIR), or nebular recombination lines (Kennicutt 1998). UV emission is mainly dominated by OB stars, that have lifetimes $\lesssim$ 108 yr (Iglesias-Páramo *et al.* 2004, Kennicutt, 1998). In contrast, the Hα line is strong only in the presence of the most massive, hot O stars (masses $> 10M_{\odot}$, ages $<$ 20 Myr) with sufficient UV output to ionize the surrounding hydrogen. These stars have even shorter lifetimes ($\lesssim$ 107 yrs; Iglesias- Páramo *et al.* 2004; Kennicutt 1998) as they rapidly evolve off the main sequence, making the resulting Hα emission the most instantaneous probe of star formation.

The ratio of the UV to Hα flux therefore gives a good relative indicator of very recent star formation history (SFH). As a nascent star forming region evolves, the Hα line emission declines earlier than the UV continuum, leading to a decrease in the Hα/FUV ratio. With appropriate assumptions about the amount of extinction by dust and the nature of the initial mass function (IMF), this ratio is a direct indicator of the age of a new star forming region. Various authors have pointed to other factors that could influence Hα/FUV flux ratio, such as variations in the initial mass function (IMF), star formation history (SFH), and metallicity (e.g. Iglesias-Páramo 2004, Meurer *et al.* 2009, Lee *et al.* 2009). Different levels of dust attenuation between individual HIIregions also has a major influence, especially in the highly extincted FUV region. Clearly, any effort to use Hα/FUV fluxes needs to account for these systematics insofar as the data allow.

Traditional comparisons between star forming distributions have concentrated on identifying entire HIIregions as individual, distinct sources. Commonly, workers in the field select HIIregions by eye (e.g. Zurita *et al.* 2001; Battinelli *et al.* 2000; Rozas *et al.* 2000; Knapen 1998; Kennicutt 1998). However, such techniques are necessarily subjective and therefore difficult to standardise or reproduce. The flux thresholds at which regions are defined can vary significantly between different observers, and the ability to differentiate individual HIIregions from more clumpy structures becomes compromised. Alternatively, region-finding codes, such as SExtractor (Bertin & Arnouts, 1996) and REGION (developed by C. Heller) search through an image for regions bounded by a chosen flux or luminosity threshold. However, such codes rely on the user subjectively placing the boundaries of HIIregions, or manually separating HIIregions that are situated too closely to allow easy discrimination by the software. Furthermore, the threshold flux is critically dependent achieving good background subtraction which is notoriously difficult in the field of a nearby galaxy. Clearly by avoiding the need to explicitly define HIIregions at all, one removes a major source of systematic error.

To this end, we are motivated to use a pixel-by-pixel differential comparison of star formation regions, analogous to the pixel Colour-Magnitude Diagrams of Lanyon-Foster *et al.* (2007), and earlier work by Abraham *et al.* (1999) and Eskridge *et al.* (2003). This technique provides information on the global SF properties of a galaxy without the need to define HIIregions. In principle, such measurements are completely characterised by pixel scale, spatial resolution, and flux threshold, and so are therefore fully reproducible over a diverse sample of galaxies.

In this chapter we derive age maps for a sample of six nearby spiral galaxies, using pixel-based methods. Section 2 describes the data and its reduction, including the methodology of the pixel-based mapping technique and corrections for extinction. We also describe our adopted model for the age calibration and explore its dependency on star formation history, metallicity, and initial mass function. In Section 3 we present our age maps and discuss them for each galaxy in turn.. In Section 4 we analyse the uncertainties and robustness of this method in the context of both random and systematic error. Section 6 contains a brief discussion and conclusions from this work.

4.2 Sample and Data

4.2.1 Galaxy Selection

The galaxies in our sample were selected across a range of star-forming types based on their orientation and proximity. Members were chosen to be as face-on as possible to mitigate the effects of extinction and scattering, as well as minimising the wavelength shift in Hα due to galactic rotation. Galaxies were also chosen with distances nearer than 10 Mpc to allow sufficient spatial resolution to resolve individual star forming structures within spiral arms. Finally, all galaxies in the sample have archival UV images from the Galaxy Evolution Explorer (GALEX[1], Martin et al 2005) database and far-infrared images from the *Spitzer* Infrared Nearby Galaxies Survey (SINGS[2], Kennicutt *et al.* 2003). The former are used for age dating and to provide estimates of extinction, while the latter are necessary for dust extinction correction. The final sample consisted of 6 spiral galaxies, ranging from early to late-type. Two of the spirals are barred, M100 and IC 2574, and all have spatially-resolved HI (Martin 1998). A summary of their main properties is presented in Table 4.1.

Optical images were obtained in Hα using the Taurus Tunable Filter (TTF; Bland-Hawthorn & Jones 1997) on the William Herschel Telescope (WHT) on 1999 March 4–6. Conditions were photometric with stable seeing of 1.0 arcsec. TTF was tuned to a bandpass of width $\Delta\lambda = 20\,\text{Å}$ centred at $\lambda_c = 6570\,\text{Å}$. The intermediate-width R0 blocking filter ($\lambda_c/\Delta\lambda = 6680/210\,\text{Å}$) was used to remove transmissions from all but a single interference order. Table 4.2 gives details of the observational set-up. Each galaxy was integrated for 1800 s in Hα and either 120 or 300 s in the continuum (Table 4.3).

The UV images come from the Nearby Galaxies Survey of the Galaxy Evolution Explorer (NGS survey, GALEX) mission. This survey contains well-resolved imaging (1.5 arcsec/pix) of 296 and 433 nearby galaxies for GR2/GR3 and GR4 releases, respectively, in two passbands: a narrower far-ultraviolet band (FUV; $\lambda_{\text{eff}}/\Delta\lambda = 1516/268\,\text{Å}$), and a broader near-ultraviolet band (NUV; $\lambda_{\text{eff}} = 2267/732\,\text{Å}$). Archival *Spitzer* images for the galaxies

---

[1] http://galex.stsci.edu/GR2 and GR4

[2] http://irsa.ipac.caltech.edu/data/SPITZER/SINGS/

of the sample were used to provide additional estimates of extinction.

4.2.2 Data Reduction

The optical tunable filter data were reduced using standard IRAF[3] tasks, as well as some written specifically for tun-able filter data. Bad pixel data were corrected using the IRAF `proto.fixpix` task and the median bias level in the overscan regions was subtracted from all frames. Both emission line and continuum images from TTF were flat fielded using a combination of dome and sky flats. Continuum images used sky flats for the corresponding broad-band filter. Night sky rings were present in most TTF images due to the well-known phase variation of transmission wavelength with changing off-axis angle. To remove this effect we assumed fixed ring pattern with radial variation centered on the optical axis and fit and subtracted the background azimuthally, as described in Jones *et al.* (2002).

Flux calibration of the continuum-subtracted TTF emission-line images was done following Bland-Hawthorn (1995). The TTF bandpass is sufficiently narrow that fluxes can be converted from counts to physical units (erg cm^{-2} s^{-1} Å^{-1}) by multiplying the total counts per second by the CCD gain, and dividing by the reduced telescope area, (which takes the central Cassegrain obstruction into account). This was then divided by the total system efficiency (telescope plus instrument), determined from published spectrophotometric standard star fluxes (Oke 1990). Standard stars were observed during each observing run at the same TTF plate spacings as for the science frames.

We first resampled and aligned our Hα, UV, and FIR image data onto a common pixel scale and orientation. Images were trimmed to a common field size, rotated to north- up east-left, and resampled to the lowest scale of all frames (1.5 arcsec pix^{-1}), using the IRAF tasks `magnify`, `geomap`, and `geotran`. Individual FIR frames were combined into a single total infrared image as described above. The effects of binning the data in this way were investigated and are discussed in Section 4.4.2. Galaxy fields were masked to a common area across the Hα, UV and combined FIR frames. Those galaxies with prominent bulges (M51 and M74) also had these central regions removed, as were foreground Galactic stars and CCD artifacts.

---

[3] IRAF is the *Image Reduction and Analysis Facility*, produced by the National Optical Astronomy Observatories (NOAO).

Table 4.1: Galaxy Parameters[a]

Galaxy	RA (J2000) h m s	Dec. (J2000) ° ′ ″	Type	Redshift	Dist.[b] (Mpc)	pc/″[c]	Inclin.[d] (deg)	Dimensions (arcmin)	M_B
NGC 628 (M74)	01 36 41.70	+15 46 59.4	SA(s)c	0.002192	11.4	55.27	5	10.5×9.5	9.95
IC 2574	10 28 21.25	+68 24 43.2	SAB(s)m	0.000190	4.0	19.39	77	13.2×5.4	10.80
NGC 4321 (M100)	12 22 54.90	+15 49 21.0	SAB(s)bc	0.005240	16.1	78.06	30	7.4×6.3	10.05
NGC 4736 (M94)	12 50 53.06	+41 07 13.7	(R)SA(r)ab	0.001027	4.7	22.79	35	11.2×9.1	8.99
NGC 5055 (M63)	13 15 49.25	+42 01 49.3	SA(rs)bc	0.001681	8.4	40.72	55.2	12.6×7.2	9.31
NGC 5194 (M51a)	13 29 52.71	+47 11 42.6	SA(s)bc pec	0.00154	8.1	39.27	20	11.2×6.9	8.96

[a] Sourced from *NASA Extragalactic Database* : – Position reference – 20032MASX.C, 1991RC3.9C (M51a); – Redshift – Lu *et al.* (1993), Huchtmeier & Skillman(1998), Rand(1995), Mulder & van Driel (1993), 1991RC3.9C, Turner & Ho (1994), respectively for each galaxy.

[b] References : (M74) Tully, 1988, Nearby Galaxies Catalogue; (IC 2574) Karachentsev et al., 2002, A&A 383, 125; (M100) Paturel et al., 2002, A&A 389, 19; (M94) Tonry et al., 2001, ApJ 546, 681; (M63) Kennicutt et al., 2003, PASP 115, 928; (M51) Feldmeier, Ciardullo, & Jacoby, 1997, ApJ 479, 231.

[c] Scale in pc per ″ in the final Hα images and the age maps plots, where the pixel scale is 1.5″/px.

[d] Martin & Kennicutt 2001; Dumke *et al.* 2008; K.T. Chyzy *et al.* 2008.

Table 4.2: Instrument set-up for Hα observations

Date	1999 March 4 – 6
Telescope	WHT
Focal station	f/8
Detector	TEK2
Pixel scale (arcsec/pixel)	0.56
Field of view (arcmin)	15
seeing (arcsec)	1.0
tunable filter	RTTF
Hα filter (R0)	$\lambda\lambda$ 668 – 24 nm
Hα continuum (R1)	$\lambda\lambda$ 710 – 28.5 nm
Hα continuum (R3)	$\lambda\lambda$ 760 – 32.6 nm

Table 4.3: Log of optical and UV exposures (in seconds)

Galaxy	$t^{a}_{H\alpha}$	t^{b}_{cont}	t^{c}_{NUV}	t^{d}_{FUV}
NGC628 (M74)	1800	300	1644	1644
IC 2574	1800	120	1861	1861
NGC4321 (M100)	1800	300	2962	1773
NGC4736 (M94)	1800	300	4019	4019
NGC5055 (M63)	1800	120	1660	1660
NGC5194 (M51a)	1800	120	2539	2539

[a] Hα image exposure time.

[b] Continuum image exposure time.

[c] GALEX near-ultraviolet (NUV) exposure time.

[d] GALEX far-ultraviolet (FUV) exposure time.

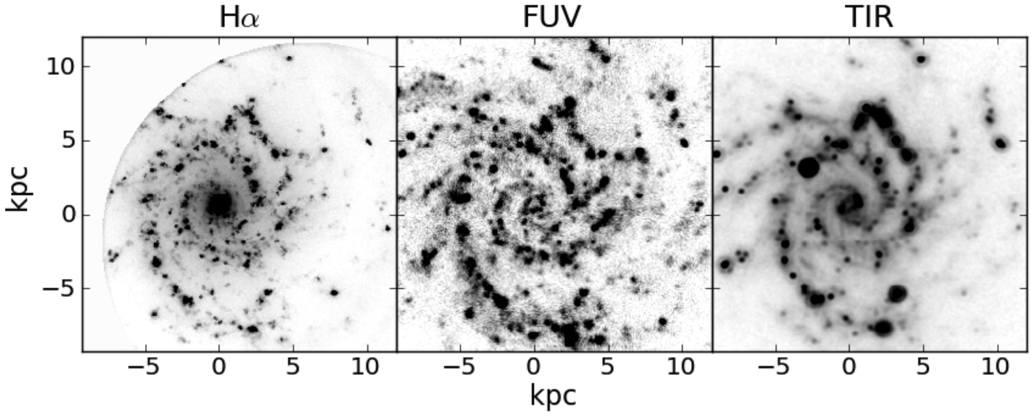

Figure 4.1: Examples of processed frames in Hα (left), far ultraviolet (FUV; centre), and total infrared (TIR; right) for the galaxy M74. The images have been resampled to have identical size, orientation, and pixel scale (1.5"/pix).

Galactic extinction was corrected using the Schlegel et al. (1998)[4] dust maps for colour excess $E(B-V)$. The extinction, A$_\lambda$, at wavelength λ was determined from

$$A_\lambda = k_\lambda E(B-V) \tag{4.1}$$

where $k_{H\alpha} = 2.54$, $k_{FUV} = 8.22$ and $k_{NUV} = 8.20$ using a Cardelli et al. (1989) extinction curve and R$_V = 3.1$.

Internal extinction for the galaxies in our sample was calculated in a two stages. First, the *Spitzer* images at 24, 70, and 160 μm for each galaxy were combined into an image of total far-infrared (TIR) flux, according to

$$F_{TIR} = \zeta_1 \nu F_\nu(24\mu m) + \zeta_2 \nu F_\nu(70\mu m) + \zeta_3 \nu F_\nu(160\mu m) \tag{4.2}$$

where [ζ_1,ζ_2,ζ_2] = [1.559, 0.7686, 1.347], (Dale & Helou 2002). The different plate scales for each frame (1.5 arcsec pix^{-1} for 24 μm, 4.5 arcsec px^{-1} for 70 μm, and 9 arcsec pix^{-1} for 160 μm) were all resampled to 1.5 arcsec pix^{-1} where necessary, identical to that of the optical and GALEX (FUV and NUV) frames. With this in hand, a value for the FUV extinction, A$_{FUV}$, was then derived through Eqn. 2 of Buat *et al.* (2005),

$$A_{FUV} = -0.0333y^3 + 0.3522y^2 + 1.1960y + 0.4967, \tag{4.3}$$

---

[4] http://www.astro.princeton.edu/∼schlegel/dust/data/data.html

which relates the TIR-to-FUV flux ratio, $y = log(F_{\rm TIR}/F_{\rm FUV})$, also referred to as the infrared-excess (IRX). This expression, and the TIR-to-FUV flux ratio, appear to be much a more robust and universal tracer of dust extinction than other methods. As a quantitative dust estimator, it is found to be almost independent of dust and stellar geometry, provided that the galaxies are forming stars actively (Buat & Xu 1996; Buat *et al.* 1999; Gordon *et al.* 2000). With no available Hβ data, the A(Hα) extinction was calculated using the relation $A_{FUV} = 1.4A(H\alpha)$ of Boissier *et al.* (2005). This equation assumes the extinction curve of Pei (1992) and that the colour excess of the stellar continuum ($E(B-V)_{\rm S}$) relative to the gaseous emission ($E(B-V)_{\rm g}$) is $A_{FUV} = 8.87E(B-V)_S$ (Calzetti 1994, 1997).

4.2.3 Age Calibration

Model Hα and FUV luminosities were generated from Starburst99 (Leitherer et al. 1999; Vázquez & Leitherer 2005). The code can be run with two different star formation modes: an instantaneous burst or continuous. In choosing our model inputs we considered three alternatives in the stellar initial mass function, (IMF):

(i) Case A: a Salpeter law with $\alpha = 2.35$ and $M_{up} = 100M_{\odot}$ (our reference model),

(ii) Case B: a truncated Salpeter law with $\alpha = 2.35$ and $M_{up} = 30M_{\odot}$, and

(iii) Case C: a Miller-Scalo law with $\alpha = 3.3$ and $M_{up} = 100M_{\odot}$,

For each of these, we used five values of metallicity: Z = 0.04, 0.02 (solar, $Z_{\odot}$), 0.008, 0.004 and 0.001. Five metallicities were used for each IMF: Note that although Z is used in this context to distinguish among the different model metallicities, it is not strictly the logarithmic number abundance of metals relative to the Sun (Vázquez & Leitherer 2005). Leitherer *et al.* (1999) list these models in their Table 1.

The full models cover the age range 10^6 to 10^9 yr in stpng of 1 Myr with spectral energy distributions (SEDs) spanning 100 Å to 1 μm in wavelength. However, we restricted the ages from 1 to 10 Myr as we are only interested in the youngest stellar populations responsible for the Hα and UV output. We compute our model luminosities as

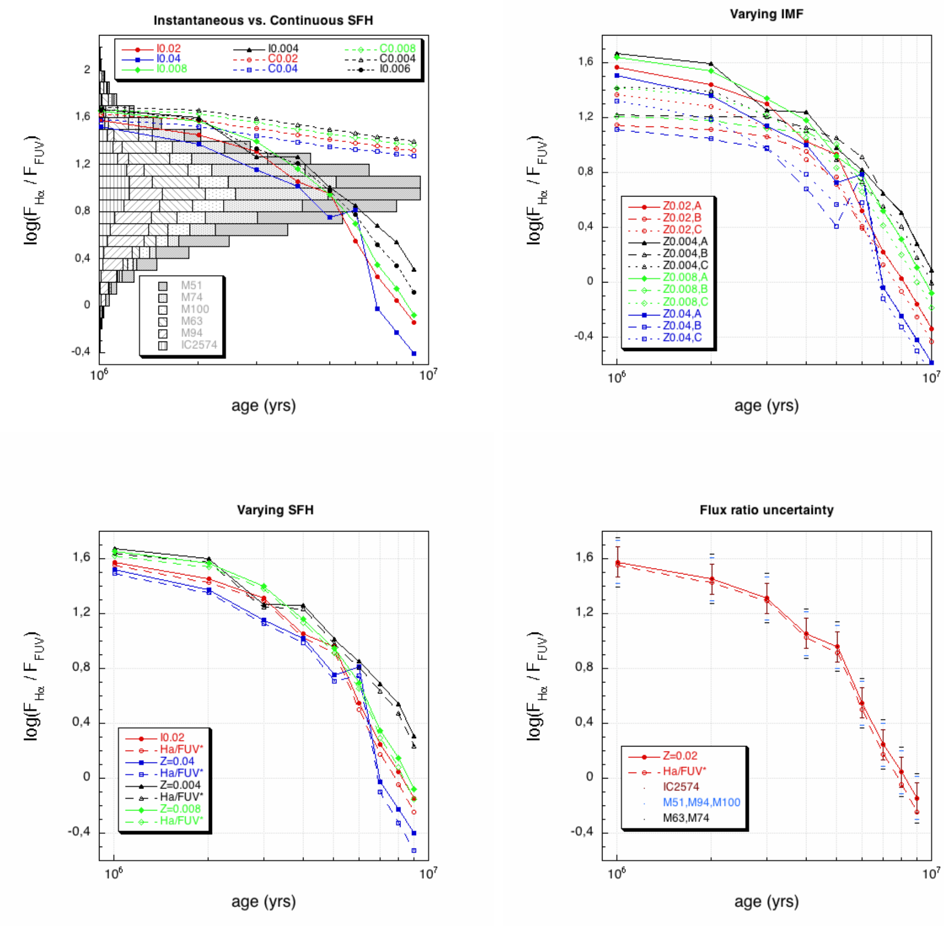

Figure 4.2: The effect of varying SFH, IMF, and metallicity on model Hα to FUV flux ratios, log(F$_{H\alpha}$/F$_{FUV}$). *Upper left:* Flux ratio in the case of both instantaneous (dashed lines) and continuous SFHs (solid lines). The models in this panel assume a Salpeter IMF and range of metallicities: Z =0.02 (red circles), 0.04 (blue squares), 0.008 (green diamonds) and 0.004 (black triangles). The underlying histogram shows the range of measured flux ratios for each galaxy in the sample. *Upper right:* Model Hα to FUV flux ratios as a function of varying IMF: (A) Salpeter, $\alpha = 2.35$ and $M_{up} = 100M_{\odot}$; (B) truncated Salpeter, $\alpha = 2.35$ and $M_{up} = 30M_{\odot}$; (C) and Miller-Scalo, $\alpha = 3.3$ and $M_{up} = 100M_{\odot}$. In these cases, the assumed SF law is instantaneous and the metallicities are the same as those in the upper left panel, and with the same colour coding. *Bottom left:* A comparison between an instantaneous SFH with recent 25 Myr-old burst (dashed lines) to a plain instantaneous burst (solid lines). The latter are the same solid curves as shown in the upper left and the same metallicities (and their colours) have been used. *Bottom right:* A comparison of the systematic model uncertainties with random uncertainty in the flux measurements. The instantaneous and (instantaneous+recent burst) models are shown (solid and dashed red lines, respectively). Photometric measurement errors for the galaxies (in three groups) are indicated by the horizontal bars.

$$log(L_{H\alpha}) = log(EW(H\alpha)) + log(C(H\alpha)) \tag{4.4}$$

$$L_{FUV} = \frac{\int F(\lambda)S(\lambda)d\lambda}{\int F(\lambda)d\lambda} = \frac{\sum_{\lambda=1341}^{1809} F(\lambda)S(\lambda)}{\sum_{\lambda=1341}^{1809} F(\lambda)} \tag{4.5}$$

where $EW(H\alpha)$ is the Hα equivalent width (in Å), and $C(H\alpha)$ is the Hα continuum (measured as the median continuum luminosities at wavelengths 6550 and 6590 Å). The $F(\lambda)$ term in Eqn. 4.5 is the GALEX response curve and $S(\lambda)$ is the luminosity of the SED in units of erg s^{-1} Å^{-1}.

To assess the suitability and robustness of our reference model we calculated the effect of changing various model inputs on the SB99 F$_{H\alpha}$/F$_{FUV}$ ratios (Figure 5.3). The upper left panel shows of Fig. 5.3 shows the ratios for both an instantaneous and continuous SFH, and shows the former to be much better match to the observed ratios. Like Iglesias-Páramo *et al.* (2004), we find an instantaneous SFH to be a more sensitive discriminant of the age variations in younger star forming regions. One might naively assume that because our galaxies are not starbursts they would be better modeled assuming continuous star formation. However, as our pixel approach delineates individual star forming regions (as opposed to integrating the total star formation across the face of the galaxy), each particular star-forming region, represented by a pixel in the image, is more accurately regarded as having undergone a stellar burst. Although the SFHs of individual regions will be more complex, an instantaneous starburst is a reasonable approximation for localised regions of star formation younger than 10^8 yr (e.g., Pasquali *et al.* 2008).

In the upper right panel of Fig. 5.3 we show the effect that changing the IMF has on the Hα-to-UV ratio for a range of metallicities. All three cases of IMF are shown (A, B, and C) which represent a plausible spread of slopes and mass cut-offs. For each case we apply metallicities of $Z =$ 0.02 (solar), 0.04, 0.004, and 0.008. We see that for fixed metallicity, the variation between the different IMFs is no more than 0.4 dex for the youngest ages, reducing to ~ 0.1 dex beyond ~ 6 Myr. Alternatively, for a given fixed IMF, the variation in Hα-to-UV with metallicity is at most ~ 0.5 dex over the longest ages, reducing to ~ 0.2 dex within the first few Myr.

We would expect that the Hα-to-UV ratios are especially sensitive to SFHs that containing a recent burst of star formation (say 25 Myr). These would no longer emit in Hα but still carry some output in the FUV given the relatively longer ages of the lower mass UV-emitting stars. To investigate this, we compute FUV* which is the FUV flux generated from a current burst of star formation combined with a 25 Myr-old burst with identical SFR. In the lower left panel of Fig. 5.3 we compare the flux ratio $F_{H\alpha}/F_{FUV*}$ (for a SFH with an additional burst) to the same ratios $F_{H\alpha}/F_{FUV}$ plotted in the upper left (for an instantaneous SFH). The figure shows that there is negligible difference (< 0.15 dex) between either case of SFH, for a fixed given metallicity. We therefore conclude that recent bursts are much less of an effect on the FUV than one might expect.

The lower right panel of Fig. 5.3 puts the size of this variation due to SFH into the context of the measurement errors. The red solid and dashed lines show the reference model for both the instantaneous and (instantaneous+recent burst) cases. Also shown at each point are the 1σ measurement uncertainties for all of the galaxies. We see that compared to the observational errors, systematic uncertainty due to the SFH is negligibly small.

We conclude that of all the model inputs, it is choice of IMF that matters most over the first few Myr after an instantaneous burst of star formation. Metallicity matters more after several Myr have elapsed, and in both cases the range is 0.4 to 0.5 dex at most, and is comparable with the observation errors. We also conclude that a continuous SFH can be ruled out on the basis of our observed $F_{H\alpha}/F_{FUV}$ ratios, and that an instantaneous burst gives a more realistic distribution of values. While one might expect that the addition of a recent burst of (25 Myr ago) would affect the FUV flux significantly, we find that this is not the case. Most important of all, we see that while the change in Hα-to-UV fluxes in absolute terms is about 0.4 to 0.5 dex due to changing model inputs, the change in relative terms (i.e. difference from 1 to 10 Myr) is much less (< 0.15 dex). Therefore, any relative age comparisons are largely immune to the choice of model inputs.

4.3 Age Maps

Once the alignment and re-scaling of the images is done, we are in a position to derive calibrated age maps for the sample. We adopt our reference model which assumes an instantaneous star formation law and Salpeter IMF ($\alpha = 2.35$, $M_{up} = 100M_{\odot}$). In each

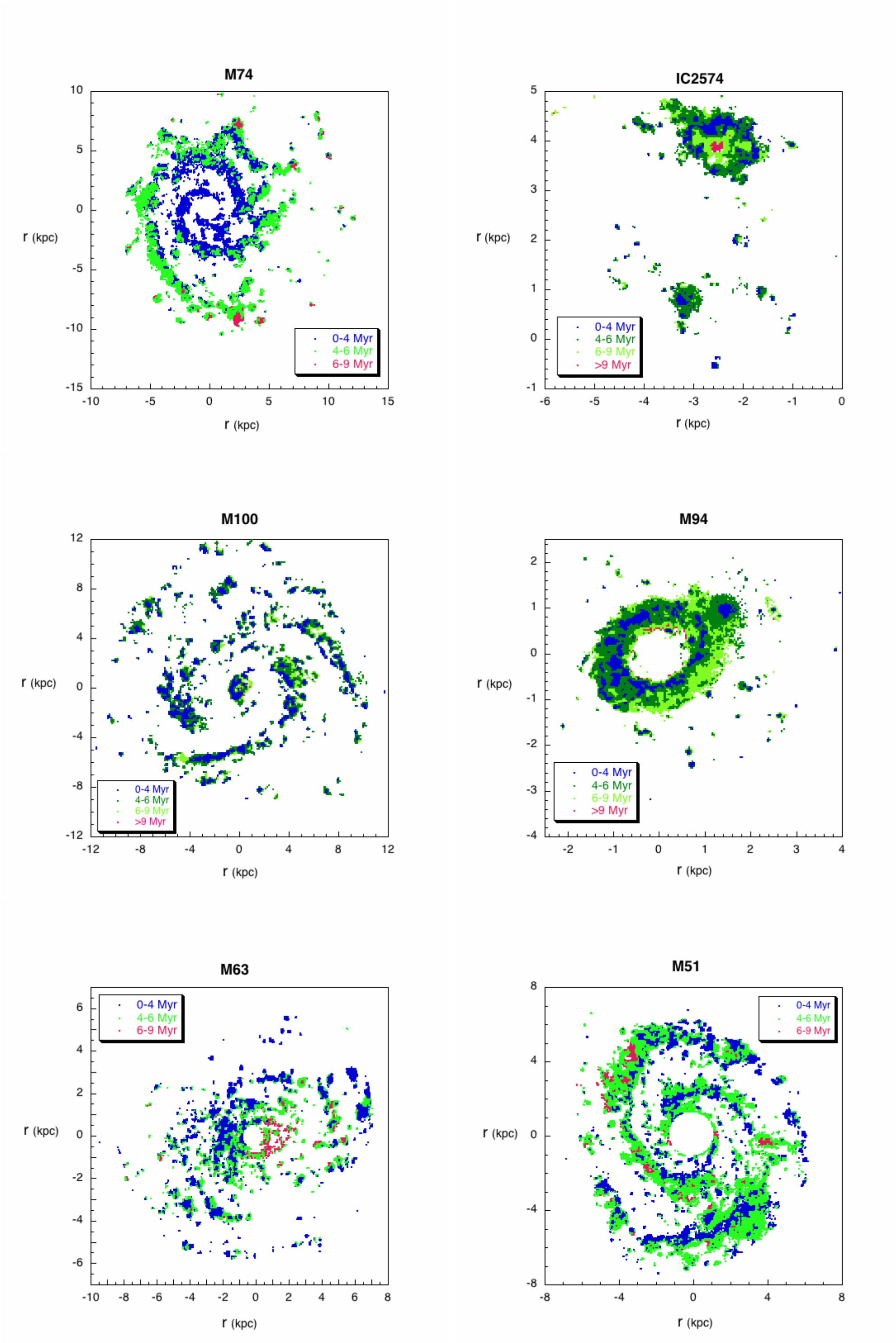

Figure 4.3: Age maps for the galaxies of our sample using the default model, with age denoted by colour as indicated in the key. Note that different colour schemes apply to those galaxies with only three age bins (M74, M63, and M51) and the remaining galaxies with four. The axes are in kpc and centred on each galaxy. North is up, east to the left.

case we assume solar metallicity, except for IC 2574 where an interpolation between $Z = 0.004$ and $Z = 0.008$ is applied. Radial oxygen abundances from Pilyugin *et al.* (2004) for all galaxies indicate that solar metallicity is representative of their mean abundances. In the case of IC 2574, Miller & Hodge (1996) give 12+log(O/H)$\sim$8.15, $\sim 30\%$ solar metallicity (8.69), which is why we have adopted the interpolated value $Z = 0.006$ for this object. The flux ratio is calibrated into SB99 model ages at ten intervals of 1 Myr, starting at 1 Myr. This age resolution is dictated by the internal precision of the flux ratio.

Figure 5.4 shows the age maps for all galaxies. Each pixel in the map is assigned a range rather than a single valued age, which is comparable to the photometric flux uncertainties and improves clarity. The maps are contoured in three or four age bins from the set $0 - 4$ Myr, $4 - 6$ Myr, $6 - 9$ Myr and older than 9 Myr. We discuss each galaxy in turn.

4.3.1 M74 (NGC 628)

M74 is a well-studied late-type SA(s)c spiral at a distance of around 11.4 Mpc (Table 4.1) with a pair of tight spiral arms($<$ 15 kpc) and no obvious bulge. Deep Hα imaging has revealed numerous HIIregions in two outer arms at 17 kpc (Lelièvre & Roy 2000). Cornett *et al.* (1994) found the star formation history of this galaxy to vary with radius, consistent with the observation by Natali *et al.* (1992) that M74 contains an inner stellar population ($<$ 1.5 Holmberg radii = 9$'$= 10 kpc) distinct from the outer disc. This separate nature of the inner disc is supported by kinematic data (Fathi *et al.* 2007) and Lick indices from the centermost region (Ganda *et al.* 2007).

M74 contains an extended envelope of HI gas (Kamphuis & Briggs 1992) while the radio continuum traces the spiral arms but not the bright central region (Braun *et al.* 2007). An elongated ring of HI ($\sim$ 2 Holmberg radii) is observed tilted relative to the main disc (Wakker & Adler 1995) and where the HI velocity field is warped. However, M74 is a relatively isolated galaxy with no nearby companions as the obvious cause of these disturbed components (see Fathi *et al.* 2007 for a discussion).

Figure 5.4 shows our age map for M74. The nucleus of the galaxy is small and bright and was saturated in our Hα maps, and so was masked. The age map shows, as a global feature, an increasing age gradient from the inner to the outer parts of the galaxy, in agreement with previous authors (Cornett *et al.* 1994, Lelièvre & Roy 2000). We find that the Hα luminosity decrease in radius is more pronounced in the inner 5 to 6 kpc, while the UV luminosity shows a shallower rate of change. Consequently, the Hα/FUV ratio decreases with radius indicating an age increases in the outward direction (Fig. 5.4). Cepa & Beckman (1990) locate the corotation radius at ~ 6 kpc, although this distance is too close to the outer limit of our data to allow any conclusions about the effect of corotation to be drawn (see also our discussion of M51 below).

On more local scales, the short arm that opens S-SW at 4 kpc shows a clear age gradient across it. The outer longer arm, that runs SE-S at $\sim$ 5 to 10 kpc, shows a less marked age gradient across its width. If the age gradients across spiral arms are a direct product of the spiral density wave, then the dilution of the gradient in this southern arm may be related to the weakness of the density wave or the approach to corotation. As discussed by Efremov (2009), the presence of a shock produced by the spiral density wave, (made visible by dust lanes along the spiral arms), is incompatible with the creation of star forming complexes, because of the absence of visible dust lanes in this arm, despite a chain of complexes along its length. The thickness of the longer arm is basically dominated by a single age range, and the youngest population located in the inner edge of the arm maps the location of the chain of complexes observed in this arm.[5]

An alternative method to gauge the impact of spiral density waves is to check the presence and distribution of an old stellar population in the far infrared. Fig. 4.4 is an colour composite of M74 in 3.6 μm (blue), 8.0 μm (green) and 24 μm (red) data from the SINGS[6] survey (Kennicutt *et al.* 2003, PASP, 115, 928). The 24 μm image maps the hot dust emission, whereas the 3.6 μm image shows the old stellar population. This shows how the nucleus, the circumnuclear region, and the inner spiral arms of M74 are all dominated by an old population. Cid Fernandes *et al.* (2004, 2005) and González Delgado *et al.* (2004) find the majority of the nuclear SED of M74 to be dominated by stars older than 1 Gyr. As is expected for a spiral density wave, the old stellar populations are distributed along the inner spiral arms. In contrast, the same 3.6 μm light is not seen along the outer longer southern arm, instead being dominate by the hot dust of star complexes. Without the influence of a spiral density wave, as outer arm evolves the stars disperse and as a result, the old stellar population is not uniformly distributed along the arm.

---

[5] Corresponding to some of these complexes, it is possible to see a bubble in expansion with a decreasing age distribution from the center.

[6] http://irsa.ipac.caltech.edu/data/SPITZER/SINGS

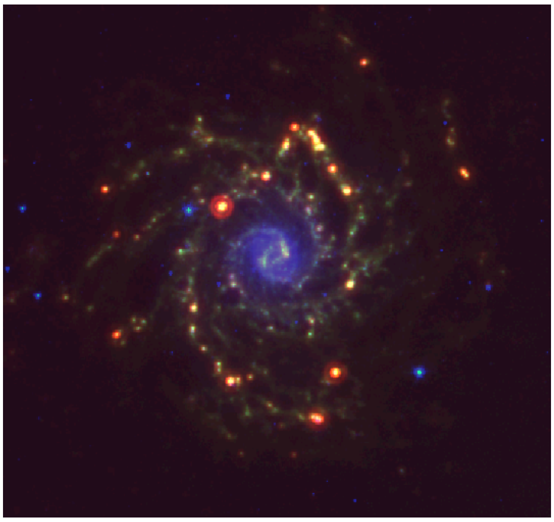

Figure 4.4: False colour composite of M74 in the far infrared, using 3.6 μm (blue), 8.0 μm (green) and 24 μm (red) data.

A circumnuclear ring of star formation (Wakker & Adler 1995, James & Seigar 1999) prompted speculation of a dust-enshrouded bar. Near-infrared imaging reveals an oval-shaped central distortion, that could be responsible for the circumnuclear ring, (Seigar 2002) and a weak bar, if any. These features are also seen in Fig. 4.4, and although the nuclear region is masked, the inner regions in the vicinity are within in the youngest age range, $<$ 4 Myr.

4.3.2 IC 2574

IC 2574 is a gas-rich dwarf galaxy and a member of the M81 group of galaxies It is classified as SAB(s)m given its HI structure showing two weak spiral arms. In contrast, its optical Hα and UV images show an irregular patchy pattern, which instead suggests a dwarf irregular classification (Weisz *et al.* 2009; Cannon *et al.* 2005; Walter & Brinks 1999; Walter *et al.* 1998). IC 2574 contains numerous HI expanding shells and holes in its interstellar medium. Walter & Brinks (1999) found 45 large expanding shell-like structures in neutral hydrogen, thought to be the combined result of supernova explosions and stellar winds produced by young stellar associations. The Hα emission is almost entirely concentrated NE of the galactic centre, the outstanding feature being a giant ($>$ 1 kpc) Hα complex (Fig. 5.4). This complex is associated with a peak in the HI emission (Martimbeau *et al.* 1994), and with one of the prominent expanding supergiant HI shells (Walter *et al.* 1998; Walter & Brinks 1999; Weisz *et al.* 2009).

Weisz *et al.* (2009) found evidence that stellar feedback created the supergiant HI shell with a recent SF episode interior to the shell, which peaked $\sim$ 25 Myr ago, and triggered secondary star formation (<10 Myr old) around its rim. This corresponds well to the structures seen in our age map of IC 2574 in Fig. 5.4. In the giant Hα complex, we also find that a younger star forming population surrounds an older one located at the center. Current star formation, as traced by Hα and mid-IR emission, is found along the rims of the larger HI holes, indicative of a propagating pattern of star formation as found by other authors (Walter *et al.* 1998), Walter & Brinks 1999, Cannon *et al.* 2005, Martimbeau *et al.* 1994). Sánchez Gil *et al.* (2009) find a similar giant star forming complex in NGC 6946 ($\sim$ 700 pc in diameter), where a central star formation event (a young and massive super star cluster) initiated the expansion of the shell, which swept up the gas and triggered secondary star formation at the rim of the shell.

4.3.3 M100 (NGC 4321)

M100 is a nearly face-on barred spiral in the Virgo Cluster 16.1 Mpc distant. The gas kinematics for this galaxy show an intriguing double bar in the gas kinematics. García-Burillo *et al.* (1998) used hydrodynamical cloud simulations to fit a two-bar model simultaneously to data in the visible, infrared, HI and CO. The two independent systems consist of (i) a nuclear bar (with fast pattern speed of $\Omega_f = 160$ km s^{-1}kpc^{-1} and corotation radius R$^F_{COR} = 1.2$ kpc), decoupled from (ii) an outer bar+spiral with slower pattern speed, ($\Omega_f = 23$ km s^{-1}kpc^{-1}, R$^S_{COR} = 8 - 9$ kpc). The M100 age map in Fig. 5.4 ends close to this value of the outer corotation radius and so is not seen in our data. The corotation of the fast pattern falls within the inner Lindblad resonance (ILR) of the slow pattern, allowing an efficient transfer of molecular gas towards the nuclear region.

Both the increased mass inflow rate and the overall higher gas density in the nuclear ring should be related to the age gradient detected in the circumnuclear ring of M100 (Ryder *et al.* 2001, Allard *et al.* 2006, Mazzuca *et al.* 2008). Allard *et al.* (2006) find a bipolar azimuthal age gradient from 10 Myr to 50 Myr using the equivalent width of Hβ in emission and Ryder *et al.* (2001) find an azimuthal age distribution 8 to 10 Myr using

Brγ and CO from IR spectroscopy. In our work, we find an azimuthal gradient for ages less than 10 Myr (Fig 5.4). These consistencies in the age gradients found through different diagnostics (sensitive to different age ranges) indicates that the circumnuclear region of M100 has experienced ongoing star formation for at least the past 50 Myr.

The circumnuclear region of M100 has been widely studied by Knapen and collaborators by means of detailed analyses of the optical and NIR morphology and kinematics (Knapen *et al.* 1995a, Knapen *et al.* 1995b, Ryder & Knapen 1999, Knapen *et al.* 2000). This nuclear ring hosts prominent massive star formation located near a pair of ILRs induced by the bar (Knapen *et al.* 1995a; Pierce 1986; Arsenault *et al.* 1988; Shlosman, Frank & Begelman 1989). The bar is visible only in the near-infrared (Pierce 1986), and fuels the starburst activity within the circumnuclear ring by channeling gas there at the median rate of $\sim 0.1 - 1$ M$_\odot$ yr^{-1} (Knapen *et al.* 1995b). This is sufficient to feed the star formation at an equivalent rate of $0.1 - 1$ M$_\odot$ yr^{-1} kpc^{-2} as measured from our Hα map. The presence of curved dust lanes bisecting the circumnuclear ring verifies the existence of large-scale shocks in this region, most likely driven by a bar-induced spiral density wave (Ryder, Knapen & Takamiya 2001). The bulk of the circumnuclear star formation events in M100 are best described by starburst models, with decay time-scales of ~1 Myr (Ryder, Knapen & Takamiya 2001), as we have used here.

In the Hα and UV M100 is asymmetric, with two bright dominant arms among others. These features are also seen in the age map (Fig. 5.4) which shows as well as the age gradients across the spiral arms, indicating the presence of a spiral density wave. The UV image has many bright and extended regions, indicating intense star-formation activity, as a majority of the stars have ages younger than 6 Myr.

4.3.4 M94 (NGC 4736)

M94 is an early-type, nearby (4.7 Mpc), spiral with a bright inner region composed of a bright circular bulge surrounded by a ring of active star-forming regions, about 1 kpc from the center (Wong & Blitz 2000).

The nucleus of M94 has been extensively studied and is classified as a LINER based on its optical emission (Heckman 1980; Ho *et al.* 1997). The presence of a compact non-thermal radio source in the nucleus coincident with an central x-ray point source and unresolved UV nucleus does not differentiate between the possibility of an active galactic nucleus or recent nuclear starburst (Turner & Ho 1994; Pellegrini *et al.* 2002; Maoz *et al.* 1995). In our Hα image, the spiral arms are too faint to be studied and the bulge is saturated and so it was masked out. A faint outer ring, about 5′ (6 kpc) in radius, is also seen in deep optical images (Sandage 1961). This outer ring is weak, diffuse and smooth (Chyży & Buta 2008). In our UV image a dim bulge and short spiral arms are visible, with a bright ring around the center of the galaxy. This ring is the main focus of our analysis.

The inner ring is a well-defined zone of intense active star formation visible in the optical, Hα (Pogge 1989), ultraviolet (Waller *et al.* 2001), and HI (Mulder & van Driel 1993), in addition to molecular (Gerin *et al.* 1991) and infrared and CO maps (Wong & Blitz 2000, Chyży & Buta 2008). The inner ring extends to a radial distance of 47″ (1.1 kpc, adopting a distance of 4.7 Mpc) around the LINER nucleus (Chyży & Buta 2008). Remarkably, most star formation in M94 is concentrated in this giant ring of young hot stars. This ring is the dominant feature in the age map of M94 (Fig. 5.4). A clear age gradient is observed across the ring, with the younger stars in the middle, surrounded by older ones both in the inner and outer rims. This young burst of star formation in the ring is also seen in Fig. 3 of Trujillo *et al.* (2009): the color luminosity profiles presented by these authors clearly show that the continuum is enhanced locally at the distance of the ring ($\sim 47''$) in the ultraviolet and blue bands, but not in the redder bands. Furthermore, the PAH emission bands (5.8, 8.0 and 24μ) are locally enhanced in the mid-infrared (MIR) luminosity profiles, but not the NIR or redder FIR bands corresponding to the older stars or colder dust. A cursory glance at the MIR Spitzer spectra indeed show the presence of strong PAH emission (see also Fig. 6 of Trujillo *et al.* 2009).

The star formation rate computed in the inner part of M94 is $\sim 0.1\ M_{\odot}$ yr^{-1}kpc^{-2}, and can be deduced from the data in Boissier *et al.* (2007, their Fig. 9.39, for HI $+$H$_2$) and Trujillo *et al.* (2009, for their 'bulge' inner region, from FUV data). From our Hα image the distribution of pixel- wise SFR is 0.1 $M_{\odot}$ yr^{-1}kpc^{-2} for pixels in the 85 percentile band. Wong & Blitz (2000) analyse CO, HI, and Hα data for this ringed galaxy, and conclude that the star formation rate is not determined solely by available gas mass, but rather that large-scale dynamics play a significant role in organizing and possibly triggering star formation.

M94 is not completely axisymmetric but has a large-scale, broad oval that may affect its internal dynamics (Kormendy & Kennicutt 2004). HIsynthesis observations (Bosma, van der Hulst, & Sullivan 1977) and optical and near-infrared imaging (Möllenhoff, Matthias, & Gerhard 1995) have demonstrated that the disk of the galaxy is nonaxisymmetric, and hence the rings may occur at the inner and outer Lindbland resonances (ILR and OLR) of an oval potential (Gerin, Casoli, & Combes 1991). Mulder & Combes (1996) found that the potential of M94 can be modeled well with an oval component at intermediate radii. These hydrodynamic simulations suggested that the rotating oval is indeed responsible for the 'rings' formation, revealing the formation of two rings, at 1.5 and 10 kpc radius, which correspond to the ILR and the OLR, with a pattern speed of 40 km s^{-1} kpc^{-1}. In addition, Möllenhoff, Matthias, & Gerhard (1995) have suggested that the inner ring may coincide with the OLR of a central stellar bar, $\sim 30''$ in extent, seen in optical and near-infrared isophotes. The rotation curve is consistent with a scenario in which the ring corresponds to the OLR of the nuclear bar and the ILR of the large-scale oval distortion. Such a coupling of nested bars may contribute to the accumulation of gas in the ring (Wong & Blitz 2000). Chyży & Buta (2008) have demonstrated that M94 has highly symmetric and strong magnetic spiral fields, not clearly associated with the shape of the distribution of star-forming regions or with spiral density waves.

4.3.5 M63 (NGC 5055)

M63 is a nearby, spiral galaxy and one of the prototype arm-class 3 flocculent galaxies (Elmegreen & Elmegreen 1987). It shows a regular, two-arm spiral structure to a radius of 4.0 kpc in the near-infrared (Luo *et al.* 2007). It has been studied extensively across the electromagnetic spectrum.

Luo *et al.* (2007) studied the *Chandra* properties of low- and-high mass x-ray binary populations, and concluded that the disk has undergone recent, strong starbursts that significantly increased the population of high-mass x-ray binaries (HMXB). Ongoing starbursts are also observed in the nu- clear region of M63. The LINER nucleus is UV bright and is surrounded by luminous young star clusters, showing clear stellar absorption signatures (Maoz *et al.* 1998; Leitherer *et al.* 2002).

In our Hα data the nucleus is saturated and was masked. The general appearance of the galaxy in Hα is flocculent, but it is significantly brighter in the E side than in the W.

An outstanding feature of the age map (Fig. 5.4) is in the inner ± 3 kpc where the W side is dominated by an older population ($6 - 9$ Myr), while the E side is dominated by a younger one (< 4 Myr). This aligns with the distribution of H? luminosity. In general, the pixels in the older age bin ($6 - 9$ Myr) are mostly located in the W half of the galaxy, the pixels in the intermediate age bin ($4 - 6$ Myr) are more evenly distributed throughout, and the pixels corresponding to the youngest age bin also occupy most of the galaxy but are weighted towards the E (particularly within the inner 3 kpc). This gives a peculiar somewhat bipolar east-west age distribution.

M63 has been studied in ^{12}CO (J=1-0) by Tosaki *et al.* (2003) and in HI by Battaglia *et al.* (2006). These authors note the regularity and symmetry of the galaxy, but a mild lopsidedness is noticeable, both in the distribution and the kinematics of the gas. These results point at two different dynamical regimes: an inner region dominated by the stellar disk and an outer one, dominated by a dark matter halo offset with respect to the disk. Tosaki *et al.* present high resolution ($\sim$4$''$) ^{12}CO (J$= 1 - 0$) mapping observations with high-velocity resolution ($\sim$ 2.6 km s^{-1}) towards the disk of M63, carried out with the Nobeyama Millimeter Array. This galaxy shows two weak spiral arms in near-infrared and CO observations, and a kinematic indication of a density wave. The map shows clumpy structures, mainly distributed along a spiral arm seen in near-infrared observations, although some are located in the interarm region. The arm consists of several clumpy structures whose typical size and mass are a few 100 pc and 10^6 M$_\odot$. They suggest that cloud formation and the ensuing star formation occur both in the arm and the interarm regions due to enhancement of gas by local fluctuations, since no clear systematic offset between the molecular gas and HIIregions is found, as neither are Giant Molecular Associations. Other near-infrared and CO observations show that there are long, continuous spiral arms though they are weaker than those of grand-design spiral arms, such as M63 (M51; Kuno *et al.* 1997; Thornley & Mundy 1997). They suggest the possibility that density waves of old stars exist in spiral galaxies universally, despite apparent differences in the strength. M63 also shows the presence of gas rotating with velocities lower than the rotational velocities of the disk. Such "anomalous" gas has already been detected in several other spiral galaxies seen at various inclination angles (e.g. Fraternali *et al.* 2002: Boomsma *et al.* 2005) and has been interpreted as gas residing in their halo regions (Swaters *et al.* 1997).

The inner < 3 kpc in M63 is conspicuously similar in its spatial structure to the dust distribution and to the velocity field. We have investigated several possible astrophysical causes for an asymmetric age distribution at larger radii. We do not find any possible mechanism that would relate the age map to the velocity field. We have also looked for a possible relation with the extinction correction, based on the appearance of the dust distribution in Fig. 12 of La Vigne *et al.* (2006). We correct for extinction by means of the FUV/TIR ratio. When this is plotted against the three age bins that span the age range under consideration, the difference of median value of this ratio is only 0.1 between the first and third age bins. This small difference translates to a negligible age increment, and thus the extinction pattern can be rejected as the source for the peculiar age pattern. In the third place we have looked into the polarization pattern as shown in Fig. 3 of Knapik *et al.* (2000). The polarization vectors are very uniformly distributed in the region where we find the age pattern, so this does not seem to be related either. We have also looked into the relationship with the molecular distribution, as presented by Thornley & Mundy (1997), but the CO distribution is fairly symmetrical both sides of the bulge at ± 2 kpc, so it does not provides any further information. Thornley & Mundy (1997) present a K image in their Fig. 3; and in this image there is a hint of the W side in the inner 2 kpc being brighter than the E side, what is consistent with the age difference we find in the age map of M63.

4.3.6 M51 (NGC 5194)

M51 is an interacting, grand-design, spiral galaxy and a member of the same group as M63. It is a metal-rich galaxy, 12+log(O/H)$\sim 8.7 - 8.9$ (Bresolin *et al.* 2004), with a weak metallicity gradient as a function of galactocentric distance (Zaritsky, Kennicutt, & Huchra 1994). Because of its large apparent size and luminosity it is possible to observe a wealth of detail in its arms and spiral structure. The age map that we compute is dominated by a young population of stars (<6 Myr). It shows an age structure with gradients across the arms, with the younger stars towards the inner edge while the stars in the older age bin are located towards the outer edges.

This age pattern is expected if star formation is trig- gered by gas shocked by the pass of a spiral density wave (Roberts 1969; Mart?ınez-Garc?ıa et al. 2009). If this is the case, we should observe the inverse age pattern outside co- rotation — that is, the youngest population preferentially located radially in the outer side of the arms. Determina- tions of the co-rotation radius for NGC 5194 are in the range 126 ″−161 ″(Vogel *et al.* 1993; Elmegreen *et al.* 1992; Knapen *et al.* 1992; García-Burillo *et al.* 1993). These estimates correspond to a distance of $\sim 4.9 - 6.3$ kpc; unfortunately our data falls just short of this range, so we are not able with this data set to confirm whether the age pattern switches at co-rotation.

Calzetti *et al.* (2005) present a panchromatic view, UV to FIR, of the star formation in M63 and the impact of dust extinction. In their Fig. 1 (left) they present an (R, G, B) = (24μ, Hα , FUV) image that further supports the age pattern across the arms that we find here. What the image shows is the same age pattern with the dust+Hα +FUV located towards the inside of the arms, while the outside is dominated by the FUV alone. As we have argued above, Calzetti *et al.* also state that the UV emission traces predominantly the evolved, non-ionizing stellar population, up to ages $\sim 50 - 100$ Myr. Thus the age pattern that we already see for the ongoing star formation, < 10 Myr, can be extended up to the recent past non-ionizing star formation, that follow in the outer part of the arms. What we are witnessing here is a clear age pattern along the spurs in the arms of the galaxy.

Scheepmaker *et al.* (2009) have studied the age distribution of 1580 resolved star clusters in M51 from HST UBVI photometry, and their spatial relation to the Hα and 20 cm radio-continuum emission. The positions of the youngest (< 10 Myr) clusters show the strongest correlation with the spiral arms, Hα , and the 20 cm emission, and these correlations decrease with age (their Figs. 16 and 17). The azimuthal distribution of clusters in terms of the kinematic age away from the spiral arms indicates that the majority of the clusters formed $4 - 20$ Myr before their parental gas cloud reached the centre of the spiral arm. The authors divide the sample in three age ranges, log(age) $< 7.0, 7.0 - 7.5, > 7.5$, and find (their Fig. 13) that the oldest clusters have older kinematic ages ($10 - 15$ Myr) compared to the intermediate age and to the youngest clusters.

4.4 Reliability and Robustness

The photometric uncertainty on the F$_{H\alpha}$/F$_{FUV}$ is dominated by the error on the FUV flux (15 to 25%) and not Hα ($<$ 5%). An additional error term comes from the use of Equation 5.12 for the FUV extinction correction, which depends on the uncertainties in the FIR. The uncertainties for the 24μm, 70μm and 160μm fluxes are 4%, 7% and 12% respectively

(Dale et al. 2007), implying 15% (upper limit) uncertainty overall in F$_{TIR}$ and 30% in the F$_{TIR}$/F$_{FUV}$ ratio. The latter are upper limits for the uncertainty, since these errors are also obtained pixel by pixel. With the application of the extinction correction the overall uncertainty in the F$_{H\alpha}$/F$_{FUV}$ flux ratio is more like 25%.

Photometric uncertainties aside, the age-dating technique is subject to a number of potential sources of systematic error. In this section we test the robustness of our results to systematics by varying the assumptions we have made over a plausible range of values. Specifically, the effects we examine are (i) the lowest limit on cluster mass allowable for our assumptions on ionizing flux, (ii) the effect of changing the spatial bin size, and (iii) the effect of changes to the metallicity and IMF assumptions in the model. We deal with each of these in turn.

4.4.1 Lowest Threshold Pixel Mass for a Fully Sampled IMF

When stellar clusters are modeled by simple stellar population synthesis (SPS) techniques over a relatively small spatial extent, incomplete sampling of the initial mass function is a concern. Cerviño *et al.* (2003) have established a threshold called the Lowest Luminosity Limit (LLL), above which, synthesis models can be applied to stellar clusters to relate ionizing flux to newborn stellar mass. The mass of a stellar system with a completely sampled IMF and luminosity equal to the LLL is M^{min}. The minimum mass depends on the metallicity, the age, the evolutionary tracks and model atmospheres used for the particular SPS model and Cerviño *et al.* (2003) publish these boundaries for SB99, as well as for their own models.

We have calculated the stellar masses of our pixels and compared with the values of M^{min} given by Cerviño *et al.* (2003). Mass is calculated based on the FUV luminosity, as a more reliable estimator of the underlying stellar population. The pixel stellar mass is a lower limit derived by comparing the linearly scaled extinction-corrected observed L$_{FUV}$ with the highest expected value from SB99, for a stellar population mass of 10^6 M$_\odot$ at the youngest cluster ages. The M^{min} for the SB99 models (with metallicities $Z =$ 0.02, 0.004 and 0.008) is less than 10^4 M$_\odot$ for the young stellar population, $<$ 9 Myr, as it is in our case (cf. Cerviño *et al.* 2003, their Fig. 5).

Figure 5.5 shows the pixel mass distributions for each galaxy compared to the 10^4 M$_\odot$

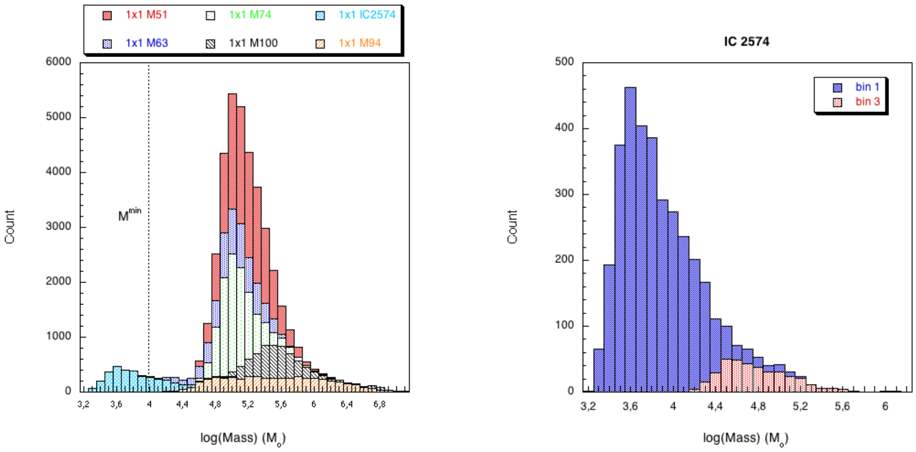

Figure 4.5: (left) The distribution of pixel stellar masses for all the galaxies of the sample, assuming the default 1 × 1 binning. The dotted line marks the limiting mass, M^{min}, corresponding to the Lowest luminosity Limit of Cerviño *et al.* (2003). (right) The same for IC 2574 only in two instances of binning: 1 × 1 (blue shading) and 3 × 3 (red).

mass limit, using the 1 × 1 binning applied to all galaxies for our main results. Individual pixels range from ∼ 10 to 50 pc on a side (Table 4.1). Save for the irregular IC 2574, all galaxies have pixel stellar masses greater than 10^4 $M_{\odot}$, and therefore lie beyond the threshold for incomplete sampling of the IMF. IC 2574 is less massive than the rest of spiral galaxies of the sample, as it is usual for irregular galaxies. In the right panel of Fig. 5.5 we show the effect of binning the IC 2574 data by 3 × 3 which puts the spatial sampling of IC 2547 above the threshold (cf. Fig. 5 of Cerviño *et al.* 2003). In the following section we show that the age map for IC 2574 is the same irrespective of whether 1 × 1 or 3 × 3 binning is used.

4.4.2 Spatial Binning Scale

We now examine the issue of whether the Hα /FUV age calibration is valid on spatial scales other than those used for our results (1 × 1 binning). This is to verify whether the amount of Hα and FUV flux in an individual pixel reflects the number of ionizing O and B stars within the same pixel. Our results should be independent of the geometry of individual HIIregions on the scales at which we sample the galaxies.

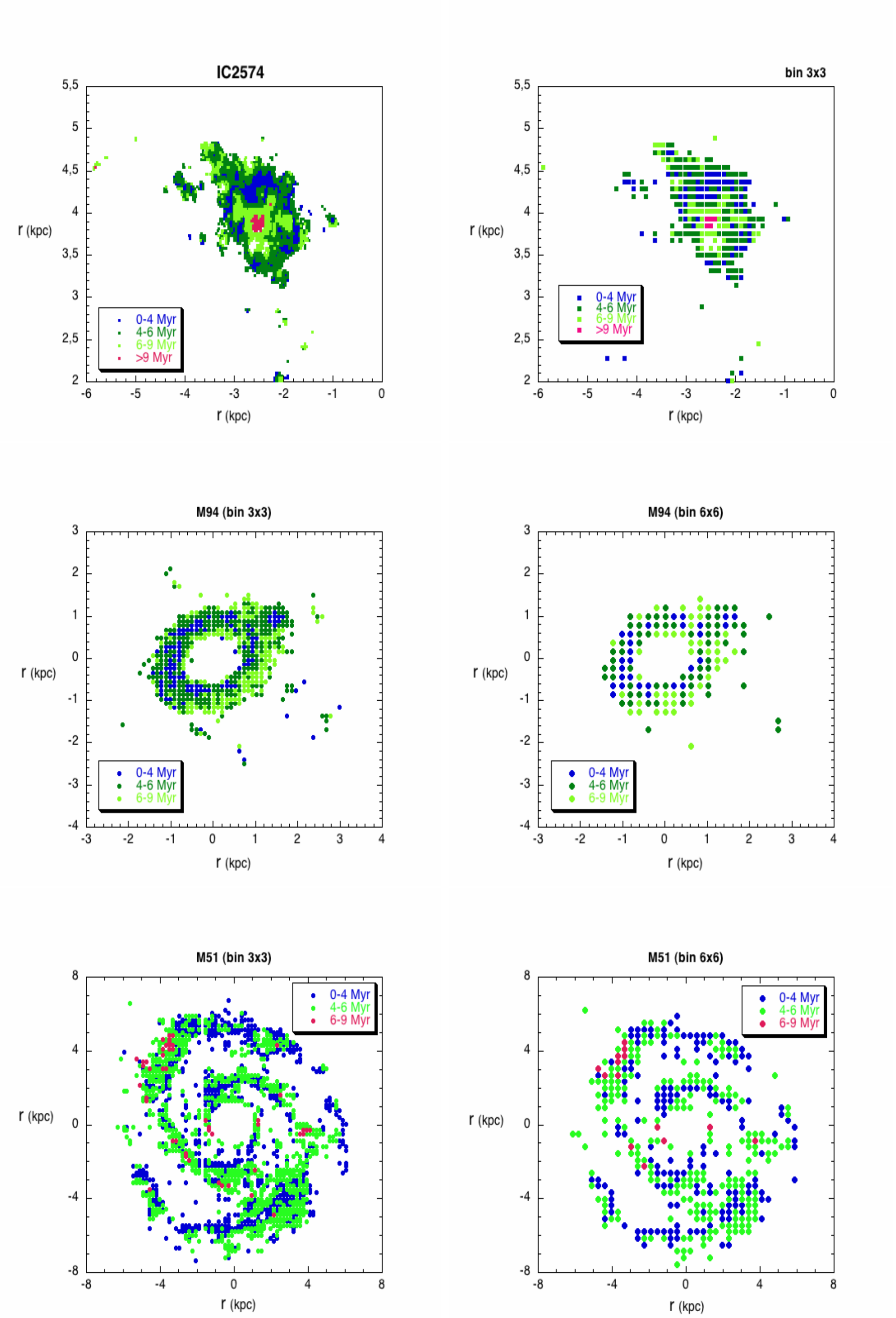

Figure 4.6: Agemaps obtained after binning the images of the galaxies. The axis are just the pixel position at the images. Top left plot is the pixel by pixel age map of IC 2574, zoomed at the northeastern stellar complex, and the top right plot is the age map after a 3×3 binning. The other two cases are, at left the agemaps after the 3×3 binning, with a pixel scale of 4.5"/px, and at the right the 6×6 binning with a pixel scale of 9"/px.

Figure 5.6 shows coarser resampling of three galaxies (IC 2574, M94, and M51) using 3 × 3 and 6 × 6 binning, (to compare to the 1 × 1 binning used in Fig. 5.4. The three galaxies we have chosen are representative of the range of morphologies encountered in the full sample: spiral arms, a stellar ring, and a giant star forming complex. In the case of IC 2574, we concentrate on the giant northeastern star forming complex at the original sampling and 3 × 3 binning; the size of this star forming region is too small to justify the 6 × 6.

As Fig. 5.6 shows, the age structures and gradients remain the same irrespective of binning scale used. This demonstrates the robustness of the pixel-by-pixel technique against systematics due to sampling. Furthermore, the resampling of the 24μm (1.5 arcsec), 70μm (4.5 arcsec) and 160μm (9 arcsec) SPITZER images to a common 1.5 arcsec plate scale has not affected our estimate of the total infrared flux nor its use in the dust corrections.

One of the galaxies in our test set, M51, has several independent flux measurements of its HIIregions in the literature, against which we can test the robustness of our own measurements to the effects of binning. Scoville *et al.* (2001) show the distribution of HIIdiameters in M51 in their Fig. 13. Our smaller 1.5 arcsec pixel size corresponds to 70 pc (using the distance in Scoville *et al.* 2001), a size that encloses some 95% of all M51 HIIregions. So even at the limit of our smallest sampling scale we have pixels that wholly contain the vast majority of HIIregions in that galaxy.

4.4.3 Metallicity and IMF Variation

The ages we have derived are dependent on assumed values for metallicity, as well as the adopted initial mass function (IMF). We have calculated age maps from the full range of plausible metallicity and IMFs and used the spread in resulting ages to assign a measure of confidence to the age maps we have derived earlier. We also incorporate flux measurement uncertainties into the estimate, $(log(F_{H\alpha}/F_{FUV})_0 \pm \Delta log(F_{H\alpha}/F_{FUV})_0)$. Each pixel age is computed for a grid of possible models spanning metallicity and IMF, and the mode of all ages, is chosen as the reference value. The confidence interval is calculated from the 3σ spread in computed ages from the modal age. Age values are binned in intervals of 0−4, 4−6, 6−9, and $>$ 9 Myr, for the sake of clarity.

Fig. 4.7 shows the confidence and uncertainty maps for M74, as well as the lower pixel threshold mass (as calculated in Section 4.4.1). We also show the modal age map across all computed ages, which is a useful point of reference for our final mass maps presented in Sect. 4.3. Figures 8 − 12 show the same statistical estimates for the other galaxies in our sample. The average confidence across galaxies is 64-70%, with around 80% of pixels having confidence values in excess of 50%. The average uncertainty in age is 1.4 ± 0.5 Myr, well below the youngest ages (4 Myr) across all possible models, notwithstanding flux ratio uncertainties. The youngest regions have the highest confidence values (in excess of $> 80\%$) and the lowest uncertainties. Examples of this are the inner ring in the stellar complex of IC 2574, the circumnuclear region of M94, or in the spiral arms of M100. Furthermore, we see that the mass maps do not show any effect of the mass in the age assignment. In M100 for example, there is a clear correspondence between the regions of high confidence with the most massive ones. But in M74 and M94 we find that there are regions of intermediate-high masses with lower confidence, probably due to a larger variability from the models.

4.5 Discussion and Summary

This work shows that a comparison of the Hα and FUV observations of nearby spiral galaxies is a relatively direct way to probe burst age variations in spirals. Age gradients are common features along or across the arms of grand-design spiral galaxies, as well as in circumnuclear (M94) and in irregular HIIregions (IC 2574). In cases such as M94 and IC 2574, secondary star formation is observed on the periphery of the primary site of star formation, and probably triggered by the latter. For M63, the age gradient occurs across the entire galactic disk, with the eastern side is marked by a younger population (< 4 Myr), while in the inner ±3 kpc of the western side an older population (6-9 Myr) dominates. Similarly in M74, there are age gradients across the spiral arms and an increasing age gradient from the inner to the outer parts of the galaxy. This corresponds with a very strong Hα emission in the inner part of this galaxy.

The age maps presented here provide a global view of the star formation processes taking place in the galactic disks. They relate the maximum scale of coherent star formation to other arge scale processes of star formation in galaxies, such as density waves and, in the case of M51, dynamics. However, it is beyond the scope of the present work to statistically

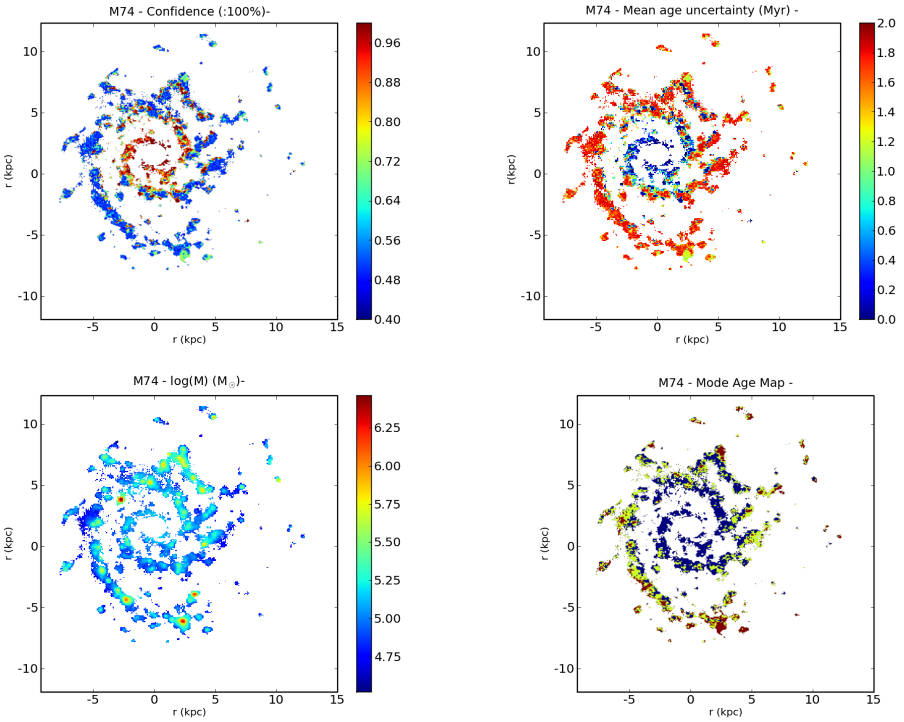

Figure 4.7: Statistical tests of the age map derived for the galaxy M74. *Top left:* Confidence map of age assignments, expressed as a probability and calculated from the full range of plausible SB99 models. It also includes flux ratio uncertainties. *Top right:* Map of age uncertainty, expressed in Myr. *Bottom left:* Map of lower pixel threshold mass, calculated in Sect. 4.4.1. *Bottom right:* Modal age map, in which each pixel age is the mode of all ages derived from full the range of plausible SB99 models and flux ratio uncertainties.

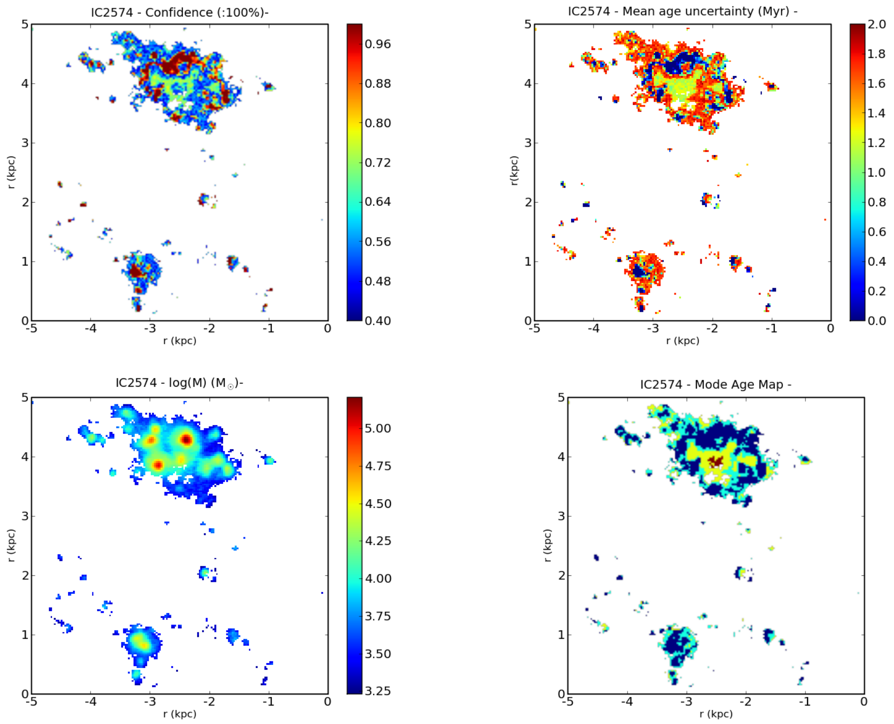

Figure 4.8: Same as Fig. 4.7 for the galaxy IC 2574.

favour one star formation mechanism over another given the extremely small sample size in hand.

One intriguing observational test recently proposed by Dobbs & Pringle (2010) predicts a different distribution of young star cluster ages depending on the mechanism for the excitation and maintenance of the spiral arms (see their Fig. 2). They suggest methods for age-dating clusters in nearby galaxies as a means of distinguishing between the various theoretical models for spiral arm formation. They consider four canonical galaxy models: (i) fixed pattern speed, (ii) galaxy with a bar, (iii) a flocculent spiral, and (iv) a tidally induced spiral. For each model in turn, they estimate the expected distribution of star clusters for ages ranging from $\sim$ 2 to 130 Myr. Although our data only cover the most recent star formation episodes up to 10 Myr, we find a spatial distribution of regions consistent with the predictions of Dobbs & Pringle (2010), as well as a similar age distribution. M74, and to a lesser degree, M100 show the expected distribution for a spiral with a fixed pattern speed and/or a bar, with a monotonic sequence of ages across the spiral arms from young to old, as predicted by standard density wave theory. In the case of our other grand design

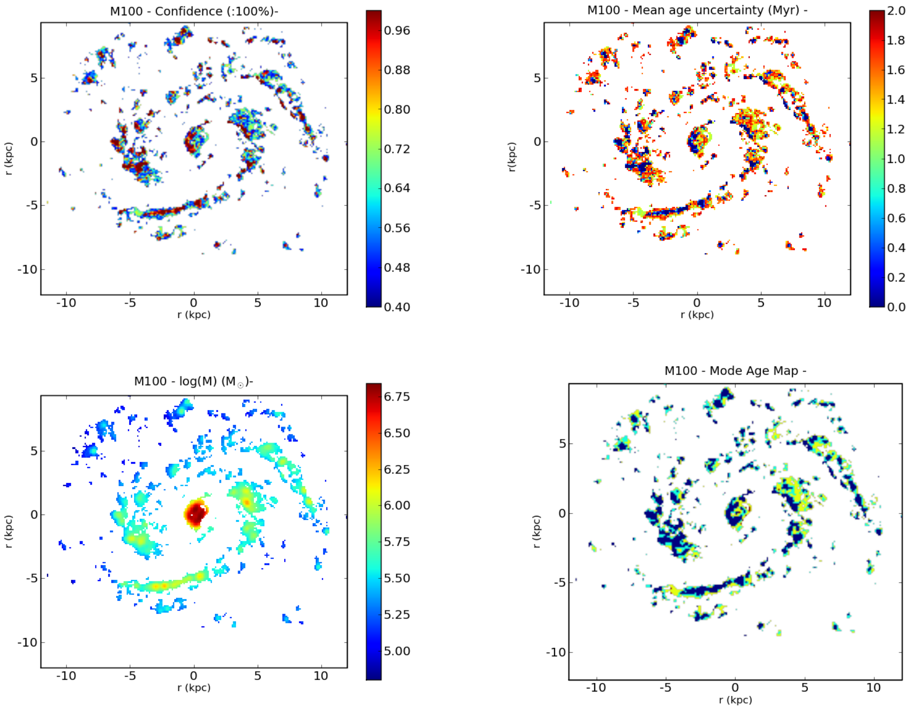

Figure 4.9: Same as Fig. 4.7 for the galaxy M100.

spiral, M51, there is no clear trend along the spiral arms, but rather a central chain of young HIIregions extending for the entire length of the arm, intertwined with older regions. With its nearby companion, M51 is typically modeled as a tidally induced spiral, undergoing a double interaction. However, its age distribution, from ∼ 2 Myr to around 130 Myr, does not show a clear trend with respect to the its interacting companion, NGC 5195, and the most recent episodes of star formation. This lends support to the model of Salo & Laurikainen (1999) that sees NGC 5195 having already undergone multiple encounters with the disk of M51, with no preferred specific site for recent star formation. Multiple encounters are also needed to explain the long tidal tail of M51 to its companion and its characteristic kink.

In the cases of IC 2574 and M94 it is difficult to identify a single possible mechanism for the triggering of star formation these galaxies. The age map for IC 2574 only shows local regions, like the giant northeastern HIIcomplex. Similarly for M94, the inner ring of intense active star formation dominates its age map. With observations of larger data sets

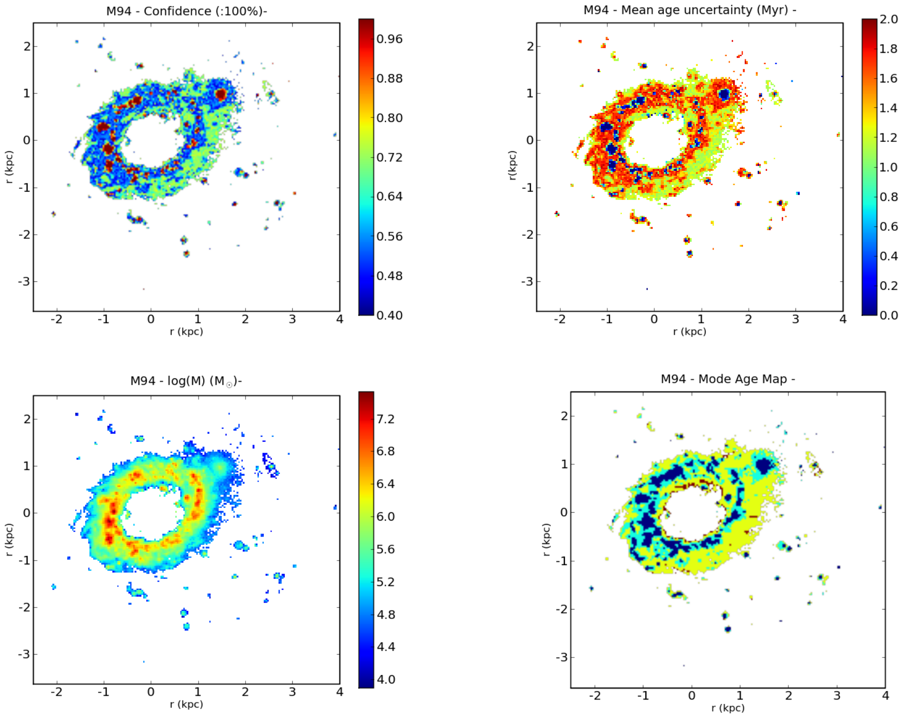

Figure 4.10: Same as Fig. 4.7 for the galaxy M94.

the method have developed here will be a powerful tool when applied to larger, statistically-significant samples of nearby star forming galaxies.

We have analyzed a sample of six star forming galaxies of a range of morphological types to study the recent history of their star formation. The study of the spatial distribution of recent and ongoing star formation provides key information about the evolutionary properties of gas-rich galaxies and the physical processes driving their evolution. Instances of star formation vary widely even among galaxies of the same morphological type (Grebel 2000) and differ as widely as the factors such as gas content, mass, or environment, that sustain it (Kennicutt, 1998).

In this chapter we have derived 2D age maps for each galaxy from a careful comparison of the UV and Hα emission on a pixel-by-pixel basis, using Starburst 99 models to calibrate the relative emission in each line as function of age. While the absolute ages derived from this method may be uncertain, its use as a *relative* age indicator appears to be relatively reliable and robust. The use of a pixel-wise age dating technique allows age mapping of

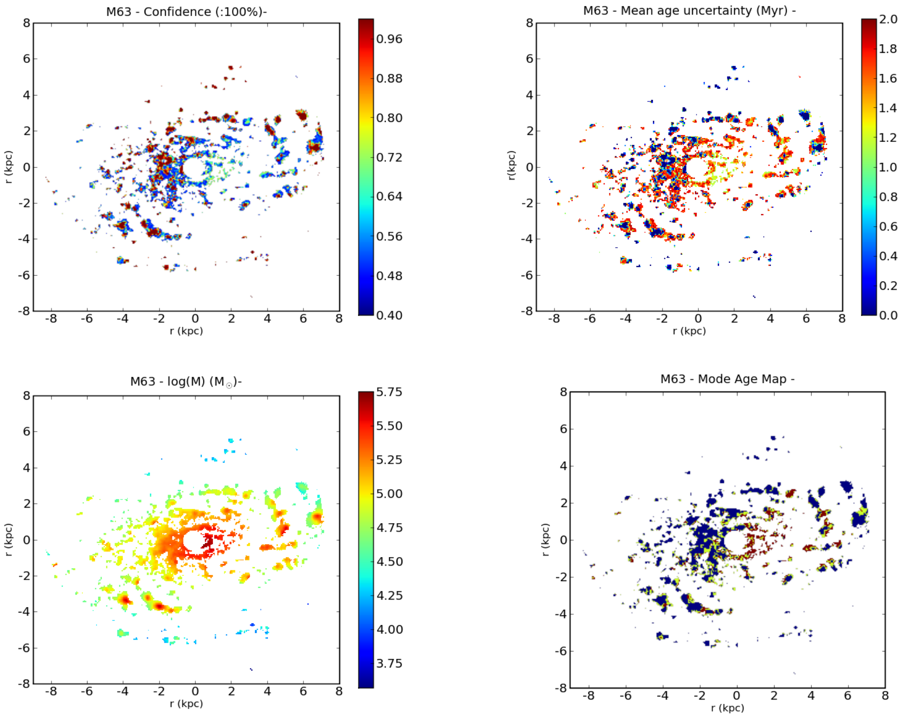

Figure 4.11: Same as Fig. 4.7 for the galaxy M63.

the youngest stellar population without prior assumptions about the spatial distribution of the star forming regions. The technique allows the spatial characterization of the age distribution which for HIIregions within a range of distance in the Local Volume through their spatially-integrated light. The far infrared flux is used to correct for extinction due to dust on pixel-scales and the flux uncertainties in $F_{H\alpha}$ and F_{FUV} are folded in throughout.

Derivations of star formation ages in this way are subject to a number of systematic factors that we have care- fully characterised to give confidence in our measurements. We have checked the validity of using a single stellar population model in pixel-sized regions by ensuring that our pixel-sized masses are well in excess of the minimum mass thresholds advocated by Cerviño *et al.* (2003). We have explored a range of different spatial binning scales to verify that undersampling does not affect the spatial distribution of ages. Finally, we have also run our models over a range of plausible IMFs and metallicities to yield confidence bounds on our derived ages. As a result of these tests, we have found that the average confidence in the age assignment is 64-70%, although in excess of 80% of regions have confidence values equal to or greater than this. We also find that the average

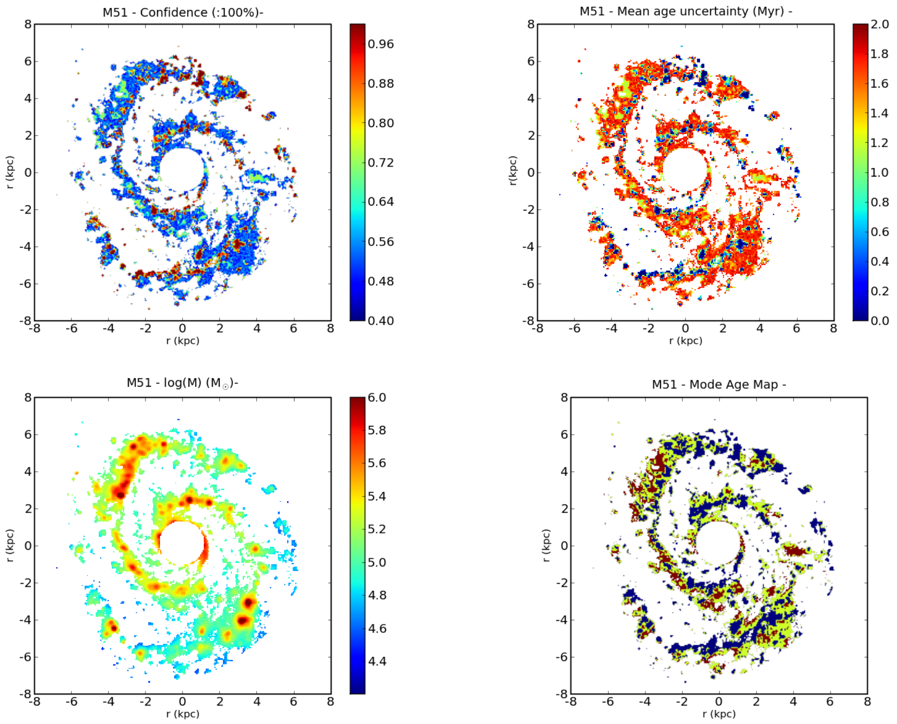

Figure 4.12: Same as Fig. 4.7 for the galaxy M51.

combined uncertainty on our ages is 1.4 ± 0.5 Myr, much less than the youngest age bin (4 Myr) adopted for our analysis.

The age maps for our six galaxies exhibit a range of circumstances. The grand design spirals M74 and M100 show evidence of age gradients along the spiral arms, with youngest to oldest running from centre to edge. This is consistent with star formation induced by spiral wave density theory. However, the spiral M51 does not show age gradients in its arms, suggesting that multiple encounters with its nearby companion NGC 5195 have destroyed any previous pattern in age. The flocculent spiral M63 shows a gradient from edge to edge rather than radially, suggesting that spiral density waves are not the dominant driver of star formation in such galaxies where the arms are more loosely wound and less well-defined.

5

Reddening analysis

Contents

5.1 Introduction 115
5.2 Dust extinction 116
5.3 Using empirical relations 119
  5.3.1 FUV extinction factor: A$_{FUV}$ 120
  5.3.2 Hα extinction factor: A(Hα) 121
  5.3.3 A(Hα) versus A$_{FUV}$ relation. 121
5.4 Using an extinction law 126
5.5 IRX-β relation 135

5.1 Introduction

We present a detailed analysis of the reddening correction that arose when it must be done in last Chapter 4, Section 4.2.2.

Dust that lies in our line of sight attenuates fluxes preferentially at shorter wavelengths and alters measurements of flux ratios, as it is the case here (F$_{H\alpha}$/F$_{FUV}$). Moreover, as we are studying extra-galactic objects both the dust within our own galaxy, and the dust within the object of study, must be accounted for.

In general, correcting the observational data for the effects of extinction requires extra measurements at specified wavelengths. However, the availability of this extra information limits how dust can be accounted for, and the amount of uncertainty in the correction.

The original sample of galaxies, to be studied throughout our age maps analysis in Chapter 4, was double than the final one. The original sample is summarized in table 5.1. The final selected sub-sample was the result of the reddening correction criteria, this is the availability of the required data at a specified wavelength, infra-red (IR) data. So only those galaxies with SPITZER data were corrected of extinction and remained in the final sample.

Along this Chapter the different approaches to realize the reddening correction are presented and discussed, as well as the reasons for choosing the applied reddening correction method in Chapter 4.

5.2 Dust extinction

The interstellar medium of a galaxy contains gas and dust: the gas consists of atoms, molecules and ions, while the dust contains small particulate matter made of various kind if ices, graphite, silicates and possibly metals (Mihalas & Binney 1981). The gas can be detected by the wavelengths of light it absorbs or emits, while dust is seen as dark absorbing nebulae, or reflection nebulae (where light from nearby stars is reflected by the dust grains). This interstellar medium causes absorption of light from the stars, reducing the intensity of the galaxy by about 1 magnitude kpc^{-1} (Mihalas & Binney 1981).

Dust both absorbs and scatters light from its original path. This is wavelength dependent, being the shorter wavelength of light the more strongly absorbed or scattered by dust, causing a reddening of the light from the object. In the far UV, the opacity is a factor of ∼2.5 greater than in the optical V band (Kuchinski *et al.* 2000).

Young, massive stars (O,B stars) provide the bulk of the UV emission, but their scale heights (i.e. mean distances along the rotation axis of the galaxy) from the plane of stars are smaller than that of the interstellar gas where they form, and so their light can be scattered and absorbed (Mihalas & Binney 1981). Older stars, with light dominating in

Table 5.1: Original sample – Galaxy Parameters[a]

Galaxy	RA (J2000) h m s	Dec. (J2000) $^{\circ}\ '\ ''$	Type	Redshift	Dist.[b] (Mpc)	Inclin.[c] (deg)	Dimensions (arcmin)	M_B
NGC628 (M74)	01 36 41.70	+15 46 59.4	SA(s)c	0.002192	11.4	5	10.5' x 9.5'	9.95
NGC1068	02 42 40.71	-00 00 47.8	(R)SA(rs)b	0.003793	14	40	7.1' x 6.0'	9.61
NGC2146	06 18 38.17	+78 21 21.6	SB(s)ab	0.002979	16	65	6.0' x 3.4'	11.38
IC2574	10 28 21.25	+68 24 43.2	SAB(s)m	0.000190	4.0	77	13.2' x 5.4'	10.80
UGC6697	11 43 49.1	+19 58 06	Im	0.022432	17	75	1.9' x 0.3'	14.08
NGC4321 (M100)	12 22 54.9	+15 49 21	SAB(s)bc	0.005240	16.1	30	7.4' x 6.3'	10.05
NGC4631	12 42 08.0	+32 32 26.0	SB(s)d	0.002021	9.0	85	15.5' x 2.7'	9.75
NGC4736 (M94)	12 50 53.06	+41 07 13.7	(R)SA(r)ab	0.001027	4.7	35	11.2' x9.1'	8.99
NGC5055 (M63)	13 15 49.25	+42 01 49.3	SA(rs)bc	0.001681	8.4	55.2	12.6' x 7.2'	9.31
NGC5194 (M51a)	13 29 52.71	+47 11 42.6	SA(s)bc pec	0.00154	8.1	20	11.2' x 6.9'	8.96
NGC5236 (M83)	13 37 00.78	-29 51 58.6	SAB(s)c	0.001721	4.1	23.9	12.9' x 11.5'	8.20
NGC5457 (M101)	14 03 12.48	+54 20 55.3	SAB(rs)cd	0.000804	7.4	18	28.8' x 26.9'	8.31

[a] Sourced from *NASA Extragalactic Database* : – Position reference – 20032MASX.C, 1991RC3.9C (M51a); – Redshift – Lu *et al.* (1993), Huchtmeier & Skillman(1998), Rand(1995), Mulder & van Driel (1993), 1991RC3.9C, Turner & Ho (1994), respectively for each galaxy.

[b] References : (M74) Tully, 1988, Nearby Galaxies Catalogue; (NGC1068, M77) Schinnerer *et al.* 2000; (NGC2146) Benvenuti *et al.* 1975; (IC 2574) Karachentsev *et al.* , 2002, A&A 383, 125; (UGC6697) Gavazzi *et al.* 2001; (M100) Paturel *et al.* , 2002, A&A 389, 19; (M94) Tonry *et al.* 2001, ApJ 546, 681; (M63,UGC6697) Kennicutt *et al.* 2003, PASP 115, 928; (NGC4631) Weliachew, Sancisi, Guélin 1978; Hummel Dettmar 1990; (M51) Feldmeier, Ciardullo, & Jacoby, 1997, ApJ 479, 231; (NGC1068) Bland-Hawthorn *et al.* 1997; (NGC2146) Gil de Paz *et al.* 2006.

[c] Martin & Kennicutt 2001; Dumke *et al.* 2008; K.T. Chyzy *et al.* 2008.

optical wavelengths, have scale heights greater than that of the interstellar dust layer, and so are less affected. Thus, a galaxy appears redder than it is intrinsically (Kuchinski *et al.* 2000).

Dust extinction can be measured in terms of magnitudes by considering *colour excesses* (Scheffler & Elsässer 1982). The colour index of an object is calculated by subtracting its longer wavelength band magnitude from its shorter wavelength band magnitude, e.g. $B - V$, $J - K$. For an object affected by dust extinction, its observed colour index will be greater than its intrinsic colour index, and this difference is the colour excess, e.g.

$$E_{B-V} = (B - V) - (B - V)_0,$$

where $(B - V)_0$ is the intrinsic colour for the spectral bands of interest. Colour excess is often given in this form, the difference between extinction factors in the blue (3600 Å– 5500 Å, denoted B) and visual (4800 Å– 6800 Å, denoted V) wavebands.

The extinction factor A_λ at a particular waveband λ adds to the apparent magnitude, i.e. reduces the flux:

$$m_\lambda = m_{\lambda,0} + A_\lambda$$

The colour excess can also be expressed in terms of the absorption, A_λ (which equals Δm_λ, the change in magnitude due to absorption), in each spectral band of interest, e.g.

$$E_{B-V} = (B - B_0) - (V - V_0) = A_B - A_V.$$

The intensity of an object is assumed to decrease exponentially with dust extinction, i.e. $I = I_0 e^{-\tau_\lambda}$, where τ_λ is the optical depth through the dust. This can be used to estimate a dust correction factor for a given spectral band:

$$A_\lambda = \Delta m_\lambda = -2.5 log(I/I_0)$$

$$A_\lambda = 2.5 \tau log(e) = 1.086\tau$$

Since dust affects shorter wavelengths more, the colour excess is a measure of the effect of dust, and can be used to predict extinction at other wavelengths. A conversion factor is required for each filter to translate the $E(B-V)$ value to an extinction factor for that filter, given by an extinction curve:

$$k_\lambda = \frac{A_\lambda}{E(B-V)}$$

Extinction curves are used to describe how dust affects light over a range of wavelengths. The observed fluxes, affected by dust extinction, can be expressed as:

$$F_\lambda = F_{\lambda,0} \times 10^{-0.4A_\lambda} \tag{5.1}$$

As we have the $F_{H\alpha}/F_{FUV}$ ratios, we need the extinction factors A(Hα) and A(FUV) to correct from extinction these ratios. Next sections show different methods to calculate these extinction factors.

5.3 Using empirical relations

Several methods have been developed in order to correct the emission-line spectra for the presence of dust. Perhaps the most widely used is based on the relative strengths of the lower Balmer lines. The Balmer decrement is a measure of the Hα-to-Hβ ratio, sensitive only to dust (Osterbrock, 1989), i,e. constant to first order in the absence of dust (Bell 2003). It gives an estimate of the attenuation of ionized gas emission, and not of the stellar continuum (Cortese *et al.* 2006). The extinction in the Balmer lines can be deduced from the comparison of the observed Hα-to-Hβ flux ratio with the theoretical value of 2.86 (Osterbrock, 1989) based on case B recombination, this is that all Lyman series photon (emitted upon transitions to n=1) are re-absorbed by other hydrogen atoms. An optically thick approximation.

But Hβ images were not available, so A(Hα) cannot be estimated just applying the Balmer decrement, a quite simple and direct method.

A first attempt to solve this difficulty was looking for some empirical relations that provide the extinction factors as functions of other values or parameters that can be obtained with the current data.

These relations are described below, both for the Hα, A(Hα), and for the FUV, A$_{FUV}$, extinction factors. The two extinction factors needed to correct for reddening the $F_{H\alpha}/F_{FUV}$ flux ratio.

5.3.1 FUV extinction factor: A$_{FUV}$

In Chapter 4, the internal extinction for the galaxy sample was calculated from equation 2 of Buat et al (2005),

$$A_{FUV} = -0.0333y^3 + 0.3522y^2 + 1.1960y + 0.4967, \tag{5.2}$$

relating A$_{FUV}$ extinction to the TIR-to-FUV flux ratio, $y = log(F_{\rm TIR}/F_{\rm FUV})$.

The total far-infrared flux was obtained by combining the archival SPITZER images at 24, 70, and 160 μm, according to the formula provided by Dale & Helou 2002:

$$F_{TIR} = \zeta_1 \nu F_\nu(24\mu m) + \zeta_2 \nu F_\nu(70\mu m) + \zeta_3 \nu F_\nu(160\mu m) \tag{5.3}$$

where [ζ_1,ζ_2,ζ_2] = [1.559, 0.7686, 1.347].

As it has been already commented, the F_{TIR}/F_{FUV} ratio appears to be much more robust and universal to trace the dust extinction, since this ratio, as a quantitative dust estimator, is found almost independent of the dust/stars geometry and of the dust properties provided that the galaxies are forming stars actively (Buat & Xu 1996: Buat *et al.* 1999; Gordon *et al.* 2000). Dust absorbs short wavelength UV radiation and thermally re-emits in the far-infrared (FIR) at 10$-$300 μm (Kennicutt 1998). IR emission is largely unaffected by dust, so the UV and FIR emission are complementary. The FIR is a measure of the amount of UV light attenuated by dust absorption. The FIR-to-UV flux ratio has a strong correlation with FUV attenuation and is often used as a robust measure of extinction to calibrate other potential estimators of extinction.

5.3.2 Hα extinction factor: A(Hα)

Cortese *et al.* (2006) provides an empirical relation between the Hα extinction factor and the ultraviolet slope β,

$$\beta = (0.37 \pm 0.07)A(H\alpha) - (1.15 \pm 0.08) \tag{5.4}$$

This relation is obtained for a sample of normal star-forming galaxies. They also obtain a fit for another sample of starbursts galaxies.

The ultraviolet slope, β, can be calibrated as defined by Kong *et al.* (2004):

$$\beta = \frac{log(f_{FUV}) - log(f_{NUV})}{log(\lambda_{FUV}) - log(\lambda_{NUV})} \tag{5.5}$$

where f_{FUV} and f_{NUV} are the FUV and NUV observed fluxes, in ergs^{-1}cm^{-2}Å^{-1}, and λ_{FUV} = 1520 Å, λ_{NUV} = 2310Å, are the effective wavelengths of the two GALEX filters respectively.

Cortese *et al.* (2006) also calculate a linear fit between β and log(F$_{TIR}$/F$_{FUV}$), the so called IRX-β relation:

$$log(\frac{L_{TIR}}{L_{FUV}}) = (0.70 \pm 0.06)\beta - (1.30 \pm 0.06) \tag{5.6}$$

In section 5.5 we present our own IRX-β relation, both for a linear and a non-linear relations, given the high amount of points, and so the good statistics that can be done.

5.3.3 A(Hα) versus A$_{FUV}$ relation.

Boissier *et al.* (2005) obtain a direct relation for M83 between the FUV extinction factor and A(Hα):

$$A_{FUV} = 1.4A(H\alpha) \tag{5.7}$$

This equation assumes the extinction curve of Pei (1992) and that the colour excess of the stellar continuum ($E(B-V)_{\rm S}$) relative to the gaseous emission ($E(B-V)_{\rm g}$) is $A_{FUV} = 8.87 E(B-V)_S$ (Calzetti 1994, 1997). It can be deduced as follows:

From the Calzetti (1994) and Calzetti *et al.* (1997) starburst reddening curve, $k(\lambda) = A(\lambda)/E(B-V)_S$ (S-stellar), we have that

$$A_{FUV} = 8.87 E(B-V)_S \tag{5.8}$$

Assuming the color excess of the stellar continuum is 0.44 times that of the gaseous emission (Calzetti *et al.* 1997, for starbursts galaxies),

$$E(B-V)_S = (0.44 \pm 0.3) E(B-V)_g \tag{5.9}$$

Then, applying the galactic extinction curve of Pei (1992) to relate E(B-V)$_g$ to A(Hα)

$$\frac{A(H\alpha)}{E(B-V)_g} = 2.26 \tag{5.10}$$

the equation 5.7 is obtained. Buat *et al.* (2002) give the relation A$_{FUV}$ $=$ 1.6 A(Hα) for starbursts galaxies.

Last relation is deduced for starbursts galaxies, and our sample is mostly formed by normal galaxies, except M83 and UGC6697. The question about the applicability of these relations to our sample of galaxies was discussed in Sections 4.2.3 and 4.3 of Chapter 4. As we assume that each pixel of the image corresponds with an HII region, it can be regarded as being under an starburst.

Method (A): This is the chosen reddening correction, the one applied in Chapter 4, due to the robustness and universality of the dust estimator F_{TIR}/F_{FUV}. This method obtains the FUV extinction factor from equation 5.2 (Buat *et al.* 2005), and the Hα extinction from last equation 5.7 (Boissier *et al.* 2005), that relates both extinction factors at these two different wavelengths.

Method (B): In this case A(Hα) is first obtained from the empirical equation 5.4 (Cortese *et al.* 2006), using the FUV and NUV data. And again equation 5.7 gives the other corresponding extinction factor, in this case A$_{FUV}$.

Figure 5.1 shows the resulting age maps from **Method (B)**, that can be compared with those obtained with **Method (A)** in Chapter 4, Figure 4.3.

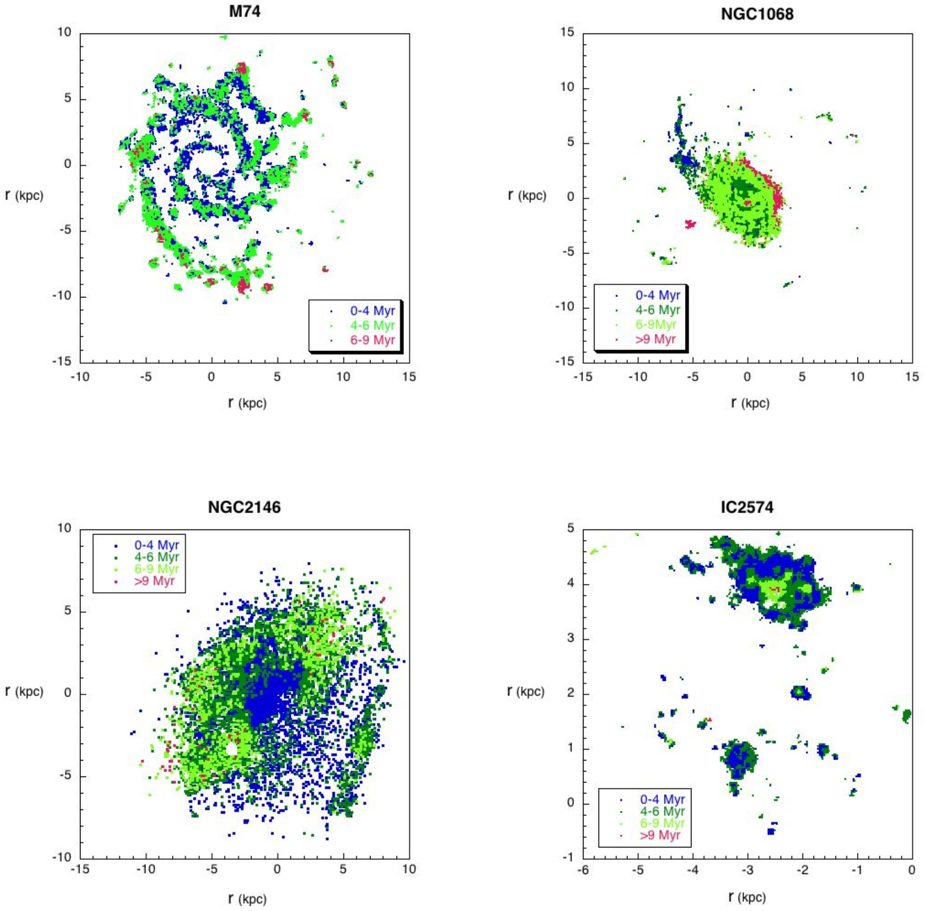

Figure 5.1: The age maps for the whole galaxy sample, where the model parameters are solar metallicity and Salpeter IMF ($\alpha = 2.35$, M$_{up}$ = 100M$_{\odot}$), and the empirical relations 5.4 and 5.7 are applied for the reddening correction. This is **Method (B)**, and no IR data are used as in Chapter 4.

Comparing these two methods we can study how the reddening correction can affect to the age calculation. Next section describes a third method for correcting from reddening,

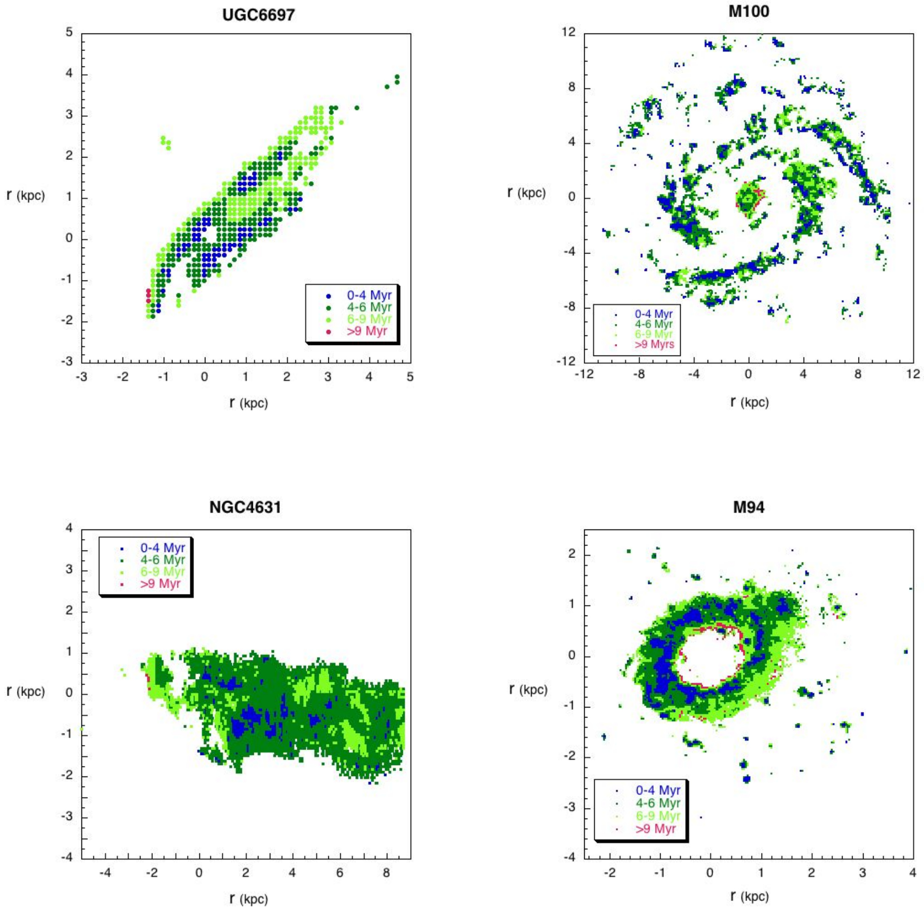

Figure 5.1: **b** –Continued–

using an extinction law, and the resulting and different age maps are compared in Figures 5.5 and 5.6.

However we find some restrictions in the β values range when we obtain A(Hα) from the Cortese *et al.* (2006) relation, equation 5.4. If $\beta <$ -1.15 the resulting A(Hα) factor is negative, and this has no physical meaning. But there are β values up to -3.7 in our galaxy sample, implying a loss of all those points in the obtained age map. Anyway, we have that $\bar{\beta}$ =-0.572 and σ_β =0.759 (statistics for the six galaxies with IR data), and so the amount of lost points is small.

Kong *et al.* 2004, Boissier *et al.* 2002 or Cortese *et al.* 2006 found minima β values

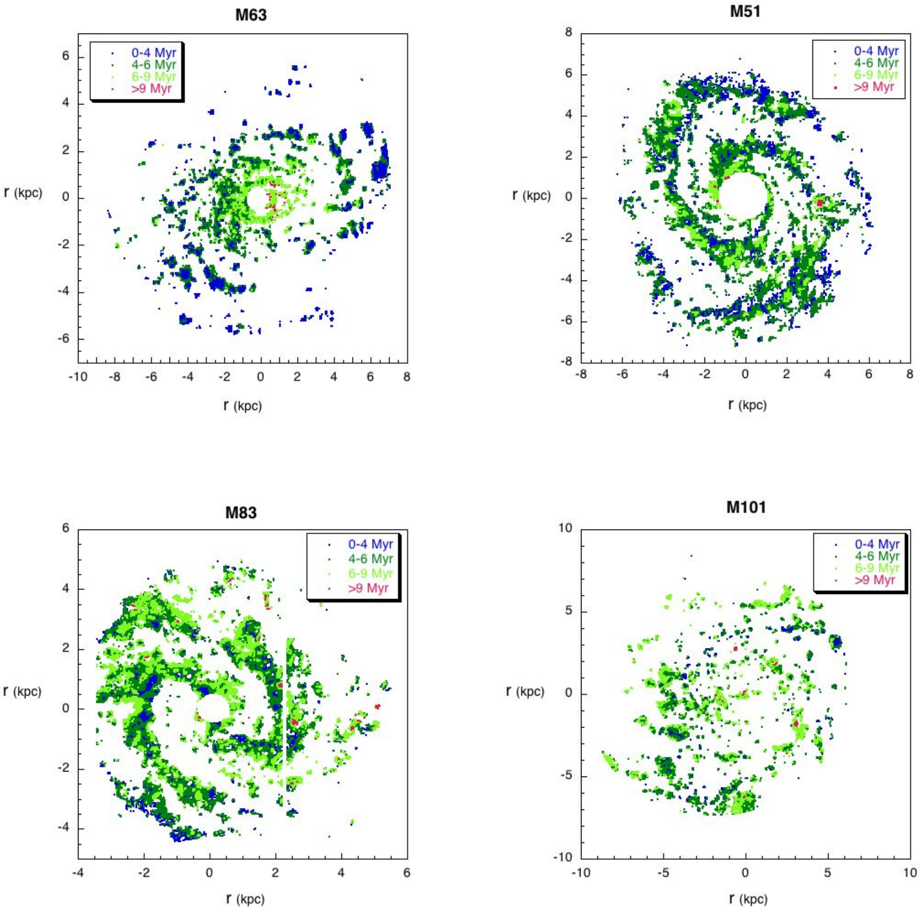

Figure 5.1: **c** –Continued–

around -2.5. Although the difference is that their samples consist of many galaxies, where each value represents the whole flux integrated over the galaxy.

In Meurer *et al.* (1999), they obtain a $\mathrm{IRX}_{1600} - \beta$ relationship (for starburst galaxies):

$$A_{1600} = 4.43 + 1.99\beta$$

where they specify "this fit implies the spectral slope in the absence of dust absorption is $\beta_0 = -2.23$". This is, where $A_{1600} = 0$, and they state that their result is consistent with what is spected for naked ionizing populations, which Leitherer & Heckman (1995) show to have $\beta_0 = -2.0$ to -2.6.

5.4 Using an extinction law

The extinction factors can be estimated also directly from an extinction law, or extinction curve:

$$A_\lambda = \phi_\lambda E(B-V) = \phi_\lambda \frac{A_V}{R_V} \tag{5.11}$$

where ϕ_λ is the extinction curve.

A first advantage applying an extinction law instead of the empirical relations should be the loss of points due to the restrictions found in β values when the latter are used.

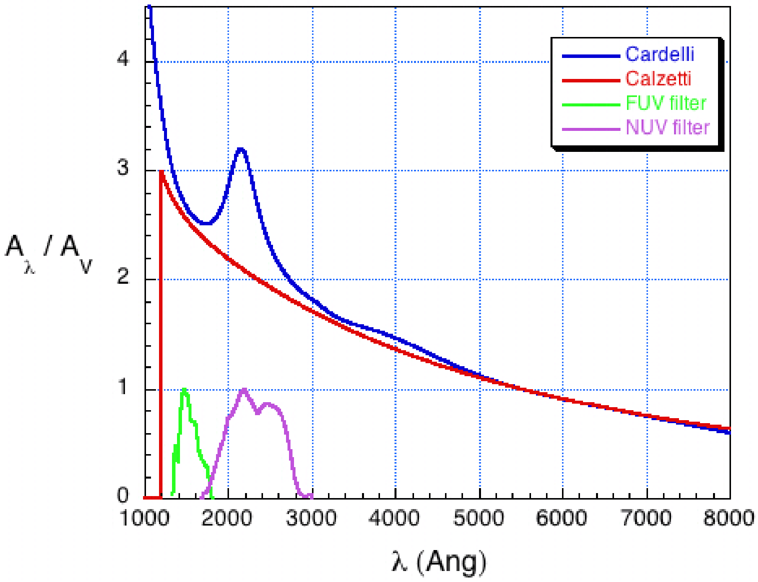

Figure 5.2: The Cardelli (1989) extinction curve, in blue color; Calzetti *et al.* (2000) extinction curve in red. The response curves of the FUV filter, green, and of the NUV filter, violet.

The question now is which extinction curve should be taken. An argument to use the Calzetti's extinction curve is that we are working with pixels interpreted as HII regions, and in that case the starburst extinction law may be suitable. In any case, the main difference between Cardelli and Calzetti curves is the "bump" in the NUV part, as it can be observed in Figure 5.2. The extinction curves, normalized, are parametrized as:

$$k_\lambda = \frac{A_\lambda}{A_V} = \frac{\phi_\lambda}{R_V} \tag{5.12}$$

The problem that arises at this point is that we do not have the optical color excess for our galaxies. But this limitation could be solved using the UV color excess, just applying again SB99 model to calculate the un-reddened ultraviolet slope, β_0, Figure 5.3 top left.

The calculation of β_0 is made from Kong *et al.* (2004) formula, equation 5.5 :

$$\beta_0 = \frac{log(f_{FUV}) - log(f_{NUV})}{log(\lambda_{FUV}) - log(\lambda_{NUV})} = \frac{log(f_{FUV}/f_{NUV})}{-0.182}$$

But this time the fluxes are those deduced from the SB99 model, not the observed ones. Figure 5.3, plot (a), shows the theoretical β_0 obtained from SB99 for different metallicity values and IMF. The theoretical luminosity for each GALEX filter, FUV and NUV, is obtained as :

$$L_{FUV,NUV} = \frac{\sum_{\lambda=\lambda_0}^{\lambda_N} F_{FUV,NUV}(\lambda) S(\lambda)}{\sum_{\lambda=\lambda_0}^{\lambda_N} F_{FUV,NUV}(\lambda)} \tag{5.13}$$

applying the synthetic spectral distribution (SED) given by SB99, S(λ) (erg s^{-1}), and the response curve for each filter, F$_{FUV}$ and F$_{NUV}$ (cm^2) respectively. λ_0 and λ_N are the spectral range for the corresponding filter (FUV: 1341 - 1809 Å, NUV: 1691 - 3009 Å). The modeled flux ratio is equivalent to the luminosity ratio, $f_{FUV}/f_{NUV} = L_{FUV}/L_{NUV}$, since the luminosity is defined as $L = 4\pi D^2 f$ (D - distance to the galaxy).

From the modeled β_0 with SB99 it is calculated its mean and median, $\bar{\beta_0}$, for ages less than 10 Myr, this is the age range that we are observing, and for each model metallicity value (with Salpeter IMF and upper mass limit of 100 M$\odot$). The calculation of a single value for each metallicity, averaged over the first 10 Myr, is based on the hypothesis that β_0 does not change with time (Meurer *et al.* 1995). In this way, with a simple linear fit, it is possible to interpolate a $\bar{\beta_0}$ value at any metallicity Z,

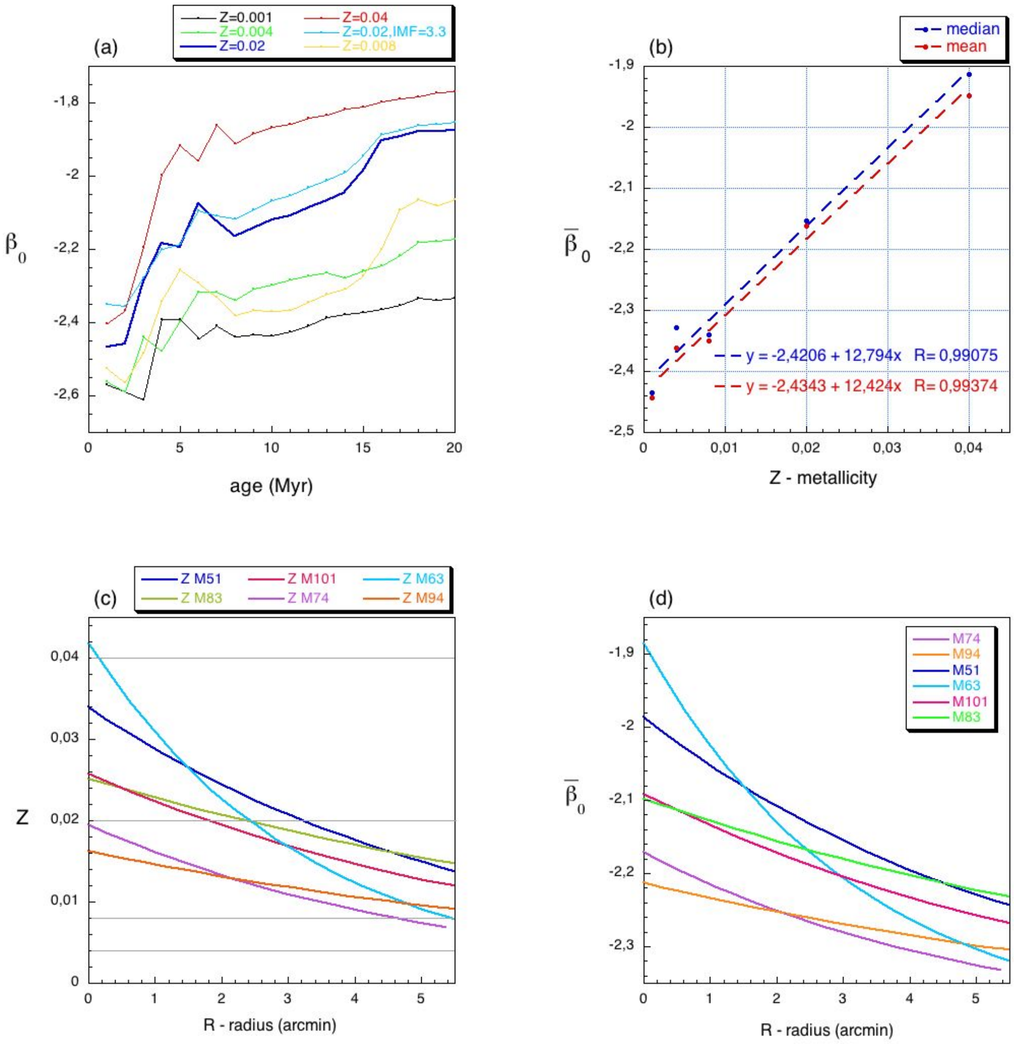

Figure 5.3: (a) Modeled β_0 by SB99, for different parameters of the model; (b) β_0 average on the first 10 Myr, for different metallicity values, and its linear fit to estimate a $\bar{\beta}_0$ at any metallicity, Eq. 5.14; (c) Metallicity gradients with the radius to the galaxy center, Pilyugin *et al.* (2004). Grey lines mark the model metallicities; (d) $\bar{\beta}_0$ *vs.* radius for some galaxies of the sample, derived from the latter metallicity gradients and Eq. 5.14.

$$\bar{\beta_0} = -2.4343 + 12.424\,\mathrm{Z} \tag{5.14}$$

At the top right of Figure 5.3, plot (b), $\bar{\beta_0}$ is plotted for each metallicity as well as its linear fit. It is checked that taking the mean (in red color) or the median (in blue) of β_0 the result is equivalent. This analysis could give an idea that how metallicity could affect the reddening correction.

Pilyugin *et al.* 2004 find metallicity gradients with distance to the nucleus for some of our spiral galaxies. These gradients are represented in plot (c), left bottom of Figure 5.3, as well as the SB99 metallicity values with horizontal grey lines (Z=0.04, 0.02,0.008 and 0.004). These metallicity gradients provide a criteria to select the best metallicity value of the model SB99 for this group of galaxies. The solar metallicity seems to be the best option for the majority of them. Except for the irregular galaxies that have smaller metallicity values, as it was the case of IC 2574 where an interpolation between Z=0.008 and Z=0.004 was taken, see Chapter 4.

From Equation 5.14, an equivalent $\bar{\beta_0}$ gradient with the radius for these galaxies can be obtained by replacing the corresponding metallicity value Z. This is represented in plot (d), right bottom of Figure 5.3. As we assume the hypothesis that β_0 doesn't change, its variability should be explained by the metalllicity gradient.

In Figure 5.4, the observed ultraviolet slope β, calculated with Equation 5.5 and the observed GALEX fluxes (FUV and NUV), is represented against the distance to the galaxy center for some galaxies of the sample (in blue color). The large number of points for each galaxy is due to the pixel by pixel technique. Each point represents an HII region in that galaxy. The black line is a linear fit that only shows the global trend of β with the radius. Whereas the red line is the β_0 gradient obtained as explained above, plot (d) of Figure 5.3. The remarkable result is that neither the metallicity gradient, nor the small variation of $\bar{\beta_0}$ with R, can explain the big gradient of the UV slope, β. So, we assume that only the internal reddening can explain it. This result also supports to take a single β_0 value in the reddening correction, since the dispersion of β is larger than the change in β_0 across the galaxy.

Once it is established a β_0 value, the UV color excess, E(β)= $\beta - \beta_0$, is directly obtained and we are able to apply a reddening correction using an extinction curve. The optical color

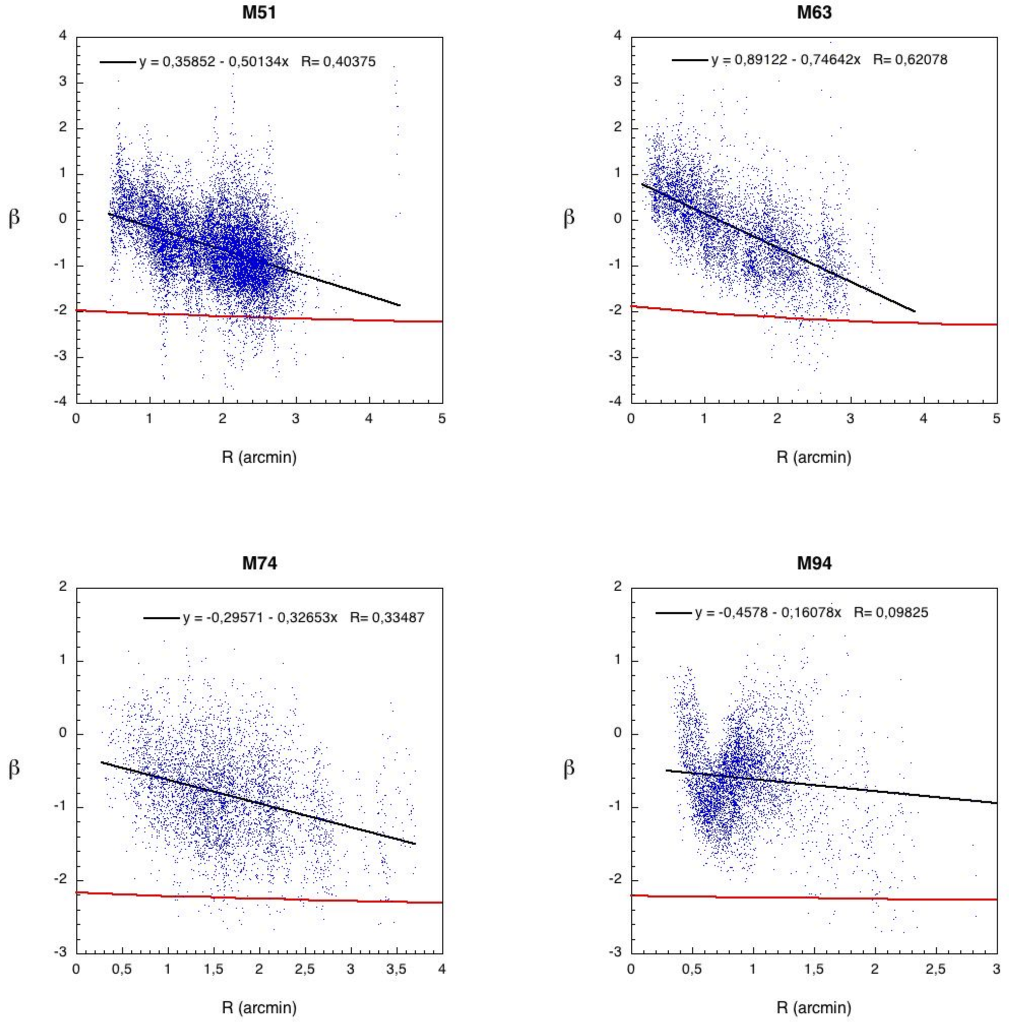

Figure 5.4: β *vs.* β_0 in front of the radius (arcmin), for some galaxies of the sample. The observed β, the blue points, is calculated with Eq. 5.5 and the observed FUV and NUV fluxes from GALEX, for each pixel in the image. The black line is a linear fit that shows the global trend of β with the radius. $\bar{\beta}_0$, plot (d) in Figure 5.3, is plotted with a red line. It is clear that neither the small variation of β_0 nor the metallicity can explain the big gradient of the observed UV slope β.

excess, E(B-V) $= A_V/R_V$, is required to use any extinction curve, as mentioned above. Although this value is not available, we have no data to get it for our galaxy sample, it can be deduced from the UV color excess E(β) as follows:

From the UV slope definition by Kong *et al.* (2004), equation 5.5, the observed flux affected by reddening, equation 5.1, and the extinction curve definition, equation 5.12, we have that

$$\begin{aligned}\beta = \frac{log(F_{FUV}) - log(F_{NUV})}{log(\lambda_{FUV}) - log(\lambda_{NUV})} &= \\ = \frac{(log(F_{FUV,0}) - 0.4A_{FUV}) - (log(F_{NUV,0}) - 0.4A_{NUV})}{-0.182} &= \\ = \frac{log(F_{FUV,0})) - log(F_{NUV,0})}{-0.182} + \frac{0.4(A_{FUV} - A_{NUV})}{0.182} &= \\ = \beta_0 + \frac{0.4A_V(k_{FUV} - k_{NUV})}{0.182} \qquad (5.15)\end{aligned}$$

Resulting then that the optical color excess, A$_V$, can be expressed as a function of the ultraviolet color excess, E(β)= $\beta - \beta_0$, as:

$$A_V = \frac{0.182E(\beta)}{0.4(k_{FUV} - k_{NUV})} \qquad (5.16)$$

Finally, the reddening correction applying directly an extinction curve and getting E(B-V) from E(β) should be as follows:

$$\begin{aligned}\left(\frac{F_{H\alpha}}{F_{FUV}}\right)_0 = \frac{(F_{H\alpha})_{obs} \times 10^{0.4A_{H\alpha}}}{(F_{FUV})_{obs} \times 10^{0.4A_{FUV}}} &= \\ = \left(\frac{F_{H\alpha}}{F_{FUV}}\right)_{obs} \times 10^{0.4(A_{H\alpha} - A_{FUV})} &= \\ = \left(\frac{F_{H\alpha}}{F_{FUV}}\right)_{obs} \times 10^{0.4A_V(k_{H\alpha} - k_{FUV})} &= \\ = \left(\frac{F_{H\alpha}}{F_{FUV}}\right)_{obs} \times 10^{0.182E(\beta)\frac{k_{H\alpha} - k_{FUV}}{k_{FUV} - k_{NUV}}} \qquad (5.17)\end{aligned}$$

This method is called as **Method (C)**. One important point that must be taken into account, to keep the consistency in all these calculations, is the resulting sign of A_V, or equivalently E(B-V), must be positive. In agreement with the assumption of the observable flux is less than the emitted one. From Equation 5.16 this translates to both E(β) and $k_{FUV} - k_{NUV}$) must be positive.

E(β) must be positive is also consistent with the fact that the reddening makes the UV slope flatter, this is $\beta > \beta_0$. Figure 5.4 shows that the majority of the pixels have β values higher than $\bar{\beta}_0$, so the loss of points that cannot be corrected with this method is small. The mean of β_0 for ages less than 10 Myr is -2.15, and most of the pixels have β values bigger than this limit. In comparison with **Method (B)**, where its application was restricted to pixels with $\beta > -1.15$, from Equation 5.4, we can correct from reddening more pixels than with the latter based on empirical relations.

In this regard, **Method (A)** should be more appropriate since there is no restrictions for correcting from reddening, and therefore no loss of points in the resulting age map.

On the other hand, Cardelli's (1989) extinction curve cannot be applied for this method because its bump. It just affects the NUV flux, making the difference $k_{FUV} - k_{NUV} < 0$ negative. Only with an extinction law without the "bump" in the NUV part of the spectrum, as the Calzetti's extinction law, the E(B-V) or A_V can be deduced from the UV color excess. Both extinction laws are plotted in Figure 5.2, together with the response curves of the FUV and NUV filters.

To finish this section we compare the resulting age maps, for M51 in Figure 5.5 and M63 in Figure 5.6, from the three different reddening correction methods. The age patterns are actually very similar, particularly between Methods (A) and (B). The striking difference is in the third Method (C), where we find a global "jump" in ages respect to the two latter. Those youngest pixels, with ages less than 4 Myr, in Methods (A) or (B), have moved to older age ranges, $4-6$ or $6-9$ Myr, and so on with the rest of age ranges.

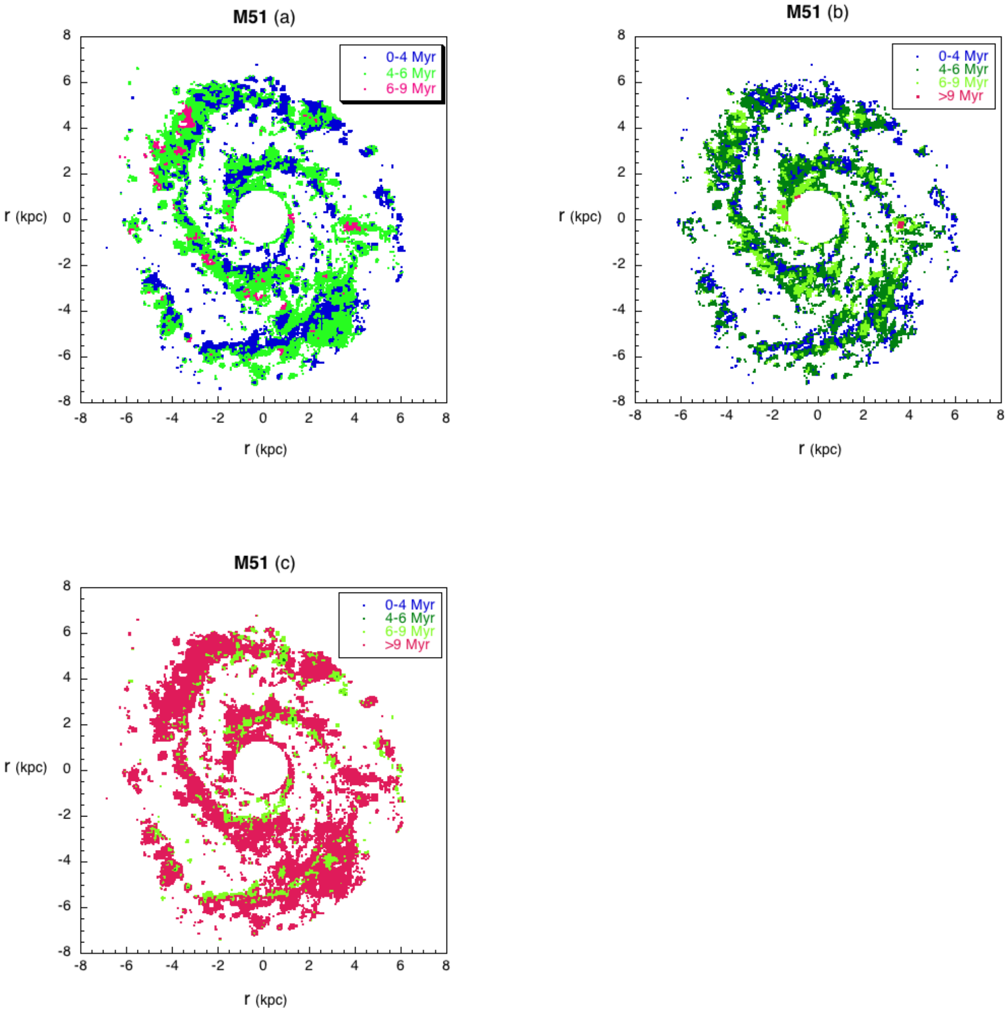

Figure 5.5: The resulting age maps for M51 applying the three different methods of reddening correction, Method (A), (B) and (C) respectively.

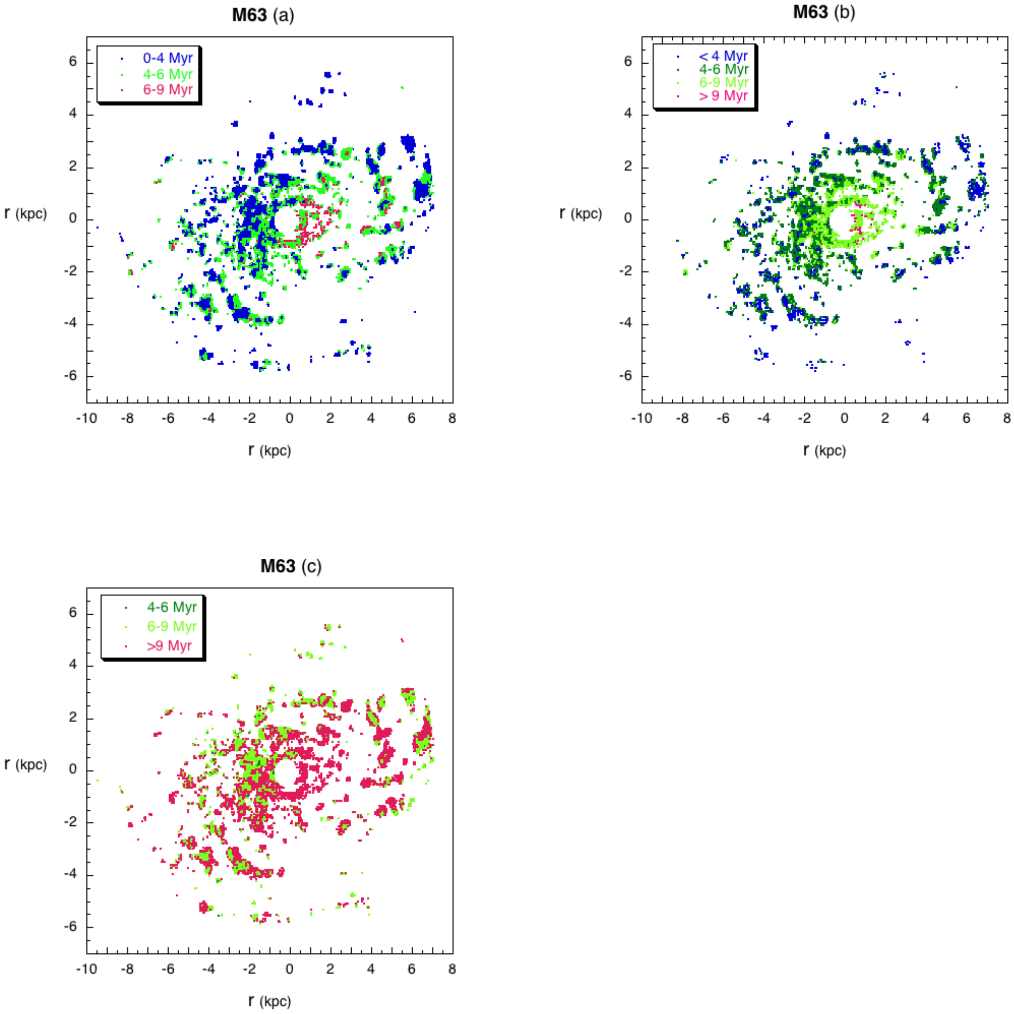

Figure 5.6: The resulting age maps for M63 applying the three different methods of reddening correction, Method (A), (B) and (C) respectively.

5.5 IRX-β relation

The IRX-β relation (Heckman *et al.* 1995, Meurer *et al.* 1999) relates the ultraviolet slope β to the ratio of total infrared to UV flux, (defined as $IRX = F_{TIR}/F_{FUV}$). It demonstrates that the UV light absorbed by dust is re-emitted as thermal emission in the far infrared, thereby allowing one to estimate the extinction in the UV from the slope. Here we independently derive our own IRX-β relation based on our pixel-by-pixel analysis of the six star forming galaxies in our sample.

Values of the UV spectral slope were derived per pixel for each of the six galaxies according to the definition of Kong *et al.* (2004),

$$\beta = \frac{log(f_{FUV}) - log(f_{NUV})}{log(\lambda_{FUV}) - log(\lambda_{NUV})} \tag{5.18}$$

where f_{FUV} and f_{NUV} are the far- and near-UV fluxes from the respective FUV and NUV GALEX filters (in ergs^{-1}cm^{-2}Å^{-1}). The central wavelengths of each bandpass are λ_{FUV} = 1520 Å, λ_{NUV} = 2310Å. The total far-infrared fluxes were calculated as described in Sect 4.2.

Cortese *et al.* (2006) use a linear fit between the log(IRX) and β,

$$log(IRX) = a + b\beta \tag{5.19}$$

although other authors (Kong *et al.* 2004, Boissier *et al.* 2007) have found that adding a non-linear term

$$IRX = 10^{a+b\beta} - c \tag{5.20}$$

produces a better fit to the data. We have fitted both linear and non-linear relations to our log(IRX)$-\beta$ relation and compared our results to these authors. Outliers were rejected if they were beyond 4-standard deviations from the mean. The linear fit was calculated using a classical ordinary least squares fit (OLS) of log(IRX) on β and vice versa. The final fit was taken as the bisector of the two OLS lines, resulting very similar to that given by Cortese *et al.* (2006) for an optically-selected sample of normal star-forming galaxies in nearby clusters. The upper left panel of Fig. 5.7 shows our fits to the full sample compared to those of Cortese *et al.* (2006) and the fit parameters are summarised in Table 5.2.

The upper right panel of Fig. 5.7 shows our non-linear fit to the same data compared to those of Kong *et al.* (2004) and Boissier *et al.* (2007). Our fit is closer to that of Kong *et al.* but shifted to higher values of β and with smaller slope, Kong *et al.* use a sample of 50 starburst galaxies, while Boissier *et al.* take a sample of 43 nearby, late-type galaxies. With the exception of the interacting M51, it can be argued that all the galaxies in our sample are normal quiescent star forming systems. However, because we consider emission on pixel scales (rather than on a galaxy-wide scale), each pixel ought to be considered as a HIIregion, in which case we would expect the behaviour to be closer to the starburst sample fitted by Kong *et al.* , as is seen in Fig. 5.7. Table 5.2 gives the parameters of each non-linear fit.

We use the Akaike Information Criterion (AIC; Akaike 1974) to choose the best fit between the linear and non-linear cases, defined as

$$AIC = -2ln(L) + 2K \tag{5.21}$$

where $ln(L)$ is the logarithm of maximized likelihood function, and K is the number of parameters in the model. In the case of least squares regression for normally distributed errors, (as it is the case here), it can be computed as

$$AIC = Nlog(\hat{\sigma}^2) + 2K \tag{5.22}$$

where $\hat{\sigma}^2$ is the variance and N is the sample size. The 'best' model is that with the lowest AIC among a set of specified models, and which best describes the data with the fewest number of free parameters.

Applying equation 5.22 to the fits from equations 5.19 and 5.20 reveal the non-linear relation to be the better fit of the two.

The pixel points in the upper left panel of Fig. 5.7 are colour-coded by galaxy and highlight the different regions occupied by each galaxy in the IRX$-\beta$ plane. The points of the irregular galaxy IC 2574 are confined to lower IRX and β values in contrast with the other spiral galaxies. We note that M51 exhibits the greatest scatter about its IRX$-\beta$ fit compared to the other spirals.

The lower panels of Fig. 5.7 show the curves of best fit for each galaxy compared to the overall fit for the sample, in both the linear (left panel) and non-linear (right panel) cases. While the non-linear case is a better fit to the sample as a whole, it would appear to be inappropriate in the case of individual galaxies. Notwithstanding our small sample size, the upper left panel of Fig. 5.7 suggest that different morphologies are reflected in varying ranges for IRX and β, and would explain the non-linear nature of the full sample. We would conclude that for a sufficiently restricted mix of morphological types and galaxy mass, the IRX$-\beta$ relation is linear, and that care should be exercised when fitting a sample that is not.

Table 5.3 lists the fit parameters to individual galaxies for both the linear and non-linear case.

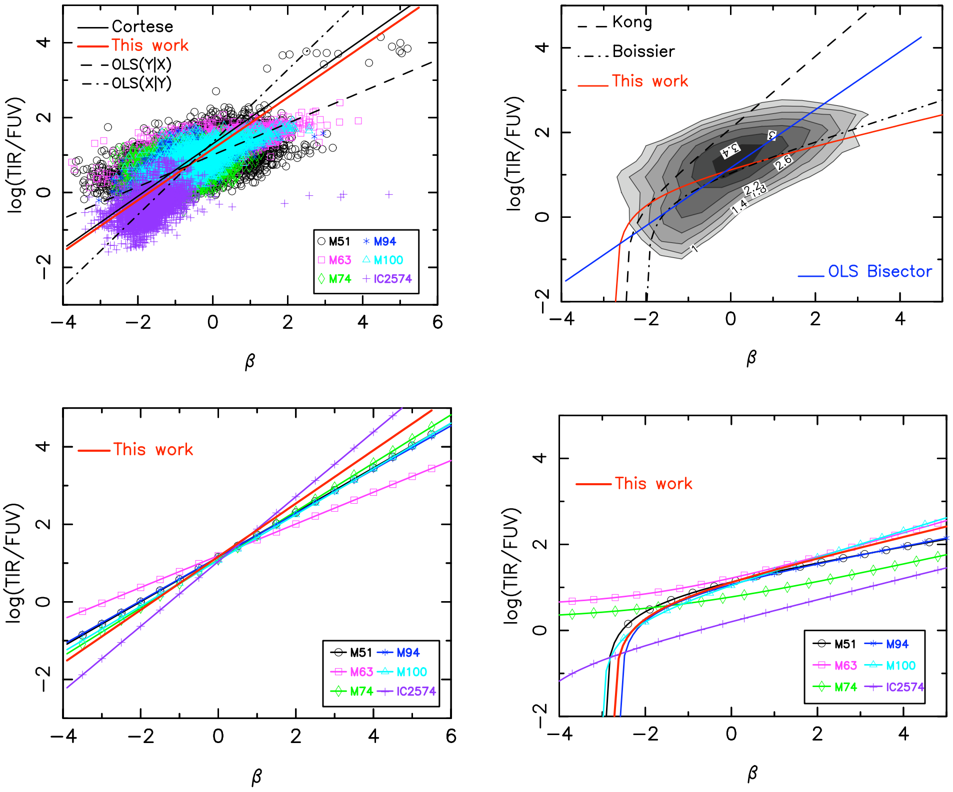

Figure 5.7: IRX$-\beta$ plots where each galaxy is represented by a different colour and symbol, as specified in the key. *upper left:* Linear fit for all points combined (red line) compared to that of Cortese *et al.* (2006) (black line). Also shown are the OLS (Ordinary Least Squares) bisectors OLS(Y|X) and OLS(X|Y) from which our full fit was derived. *upper right:* Non-linear fit for all points combined (red line) compared to those of Kong *et al.* (2004) (dashed line) and Boissier *et al.* (2007) (dot-dash line). In this case we have plotted our full sample as a density distribution with log contours. Also shown (blue line) is the linear fit from the upper left panel. *lower left:* Linear fits of the IRX$-\beta$ relation for individual galaxies, using identical colours and symbols to those in the upper left panel. *lower right:* Non-linear fits per galaxy showing the same colours and symbols as the other panels.

Table 5.2: IRX$-\beta$ fits for the full sample.

Fit		This paper	Literature
	OLS(Y|X)	log(IRX) $= 0.459(\pm 0.002)\beta + 1.001(\pm 0.002)$, R=0.662	
Linear fits	OLS(X|Y)	$\beta = 1.033(\pm 0.006) log(IRX) - 1.387(\pm 0.005)$, R=0.662	log(IRX) $= 0.7(\pm 0.06)\beta + 1.30(\pm 0.06)$(a)
	OLS bisector	log(IRX) $= 0.662(\pm 0.004)\beta + 1.151(\pm 0.004)$	
Non-linear fit		IRX $= 10^{1.225(\pm 0.009)+0.239(\pm 0.004)\beta} - 3.736(\pm 0.311)$, R=0.589	IRX $=10^{2.10+0.85\beta} - 0.95$(b) IRX $=10^{1.145+0.324\beta} - 3.136$(c)

(a) Cortese *et al.* 2006

(b) Kong *et al.* 2004

(c) Adapted from Boissier *et al.* 2007; The fit given is IRX $=10^{0.561+0.713(FUV-NUV)} - 3.136$, where FUV$-$NUV is the color between the two GALEX bands. The direct relation between β and the (FUV-NUV) is given by equation 5.18.

Table 5.3: IRX$-\beta$ by galaxy.

	Linear fit: log(IRX)$= \tilde{a}\beta + \tilde{b}$			Non-linear fit: IRX=$10^{a+b\beta}$$-$ c			
	$\tilde{a}$	$\tilde{b}$	R	a	b	c	R
M51	0.575±0.007	1.155±0.010	0.493	1.292±0.031	0.169±0.013	6.245±1.36	0.412
M63	0.409±0.008	1.191±0.009	0.659	1.107±0.027	0.288±0.014	-3.687±0.72	0.639
M74	0.623±0.015	1.090±0.014	0.357	0.631±0.078	0.223±0.054	-1.739±0.75	0.276
M94	0.564±0.009	1.156±0.011	0.673	1.241±0.033	0.185±0.016	5.79±1.28	0.672
M100	0.590±0.011	1.070±0.001	0.674	1.099±0.023	0.305±0.014	1.518±0.59	0.693
IC 2574	0.835±0.016	1.042±0.043	0.44	0.231±0.026	0.245±0.054	0.112±0.16	0.359

6

General Conclusions and Future perspectives.

> **”El ignorante afirma, el sabio duda y reflexiona.’**
>
> *Aristóteles.*

6.1 Summary

The scientific purpose for this thesis work is the stellar formation processes at different scales. One where small-scale turbulent motions dominates the physics of the system, which largest size is found to be around 1 kpc (Sánchez et al. 2010 for M33), and it corresponds with the giant stellar complex found in NGC 6946. The another regime is dominated by large-scale galactic dynamics, as the spiral arms or galactic disks analyzed in the age maps.

In one scale, the gas-star super complex located in the galaxy NGC 6946 is an excellent laboratory for the study of the interaction between the massive star formation and the gas cloud where the stars originated. The presence of a young and massive super star cluster ($\sim 10^6$ $M_\odot$, 20 Myr) appears to be the main source of ionizing photons able to generate an Hα bubble, or shell in expansion, near 730 pc in diameter.

We present for the first time the large-scale velocity field of both the approaching and receding walls of a bubble in expansion, which shows a complicated pattern with sub-bubbles forming at the walls of the largest structure, in a similar scheme to the formation 'a la Huygens', where some points on the surface of the previous bubble become the formation center of the second-generation bubbles. Moreover, it is found supports for the hypothesis of the bubble origin due to a sequence of supernova explosions, which would provide enough energy for such a large bubble. From diagnostic diagrams is deduced that most of the ionization arises from energetic photons from massive stars, although with some locations ionized by low-velocity shocks from stellar winds and/or supernova explosions, consistent with the supersonic velocity dispersion measured throughout the shell.

In a larger scale regime, for the spirals NGC 278, NGC 1058, NGC 2500 and UGC 3574, it is studied the systematic deviations above and below the galactic plane, or corrugations, of the velocity field showing characteristic sinus-wave like patterns.

Their existence have been already reported, (e.g. Alfaro et al. 2001, Matthews & Uson 2008), but we firstly report a systematic study on the velocity corrugations in a sample of nearly face-on spiral galaxies. Corrugations are closely link, as cause/effect, to the large scale star formation processes: density waves, tidal interactions, galactic bores, collisions of high velocity clouds with disk, etc. As this part of the thesis work is still in progress, no conclusions are obtained yet about their origin or mechanisms related with the disk corrugations. This is still an open problem.

The immediate work will be finishing this analysis, as studying the correlation between the Hα emission and V_Z peaks. It is interesting also determine whether there is a relation between their location in the DD and the kinematical behaviour found.

As a future plan would be also to get better spectroscopic data, since the spectra of NGC 2500 and UGC 3574 were not good enough for a more complete analysis. The Hα emission line wasn't fitted along the slits due to the low and faint emission in some regions. Other galaxies could be included as well. Moreover PPAK data for NGC 2500 is available, and certainly it will give additional and more complete kinematical information.

At large scales also, a sample of nearby, nearly face-on, spiral galaxies, with different morphological types, has been studied kinematical and photometrically, getting the star formation information both in local and large scales.

The calculation of age maps for nearby and nearly face on spiral galaxies gives some clues in the study of the star formation and the general validity of universal star formation laws. The star formation both at local and large scales can be visualized, as this method, based on the interaction of stars and gas as a probe of star formation mechanisms, helps understanding the star formation processes and its propagation.

These 2D age maps are obtained from the comparison between the UV and Hα emission in nearby and spatially resolved galaxies, providing a global view of the star formation processes taking place in the galactic disks, the maximum scale of coherent star formation, its relation with other large scale processes of star formation in galaxies, such as density waves and, as it is the case for M51, mapping the relationship between star formation and dynamics.

This work shows that a comparison of the Hα and FUV observations of nearby spiral galaxies is a relatively direct way to probe burst age variations in spirals, which flux ratio provides a robust measure of *relative* age across the disk which we discuss in terms of the large-scale dynamical motions

The use of a pixel-wise age dating technique allows age mapping of the youngest stellar population present at each pixel, without any a priori assumptions about the spatial distribution of the star forming regions. The technique allows the spatial characterization of the age distribution for HII regions within a range of distance in the Local Volume, that provide enough spatial resolution to infer the internal SFH processes.

The nature or origin and persistence of spiral structure in galaxies is still an open question. There are a few main theories. The spiral structure may be tidally driven by a companion, a central rotating bar, or orbiting dark matter clumps (e.g. Bottema 2003; Dubinski et al. 2008). A different possibility is that spirals are self-excited, where two different mechanisms are proposed. Spiral features could be the result of quasi-steady global modes of the underlying disk (Lin & Shu 1964; Bertin & Lin 1996), or they are short-lived, recurrent transient patterns from self-gravitational instabilities (Toomre 1964, 1990; Sellwood & Carlberg 1984).

The aim of this work is not to deal with such question, and the available data do not seem to be able to answer it. However, recently Dobbs & Pringle (2010), by means of numerical simulations of gas flow in spiral galaxy models, predict different distribution of clusters of different ages depending on the mechanism for the excitation and maintenance of the spiral arms (see their Fig. 2). They suggest methods for age-dating clusters in nearby galaxies as observational tests to distinguish between the various theoretical models for spiral arm formation.

They only consider four canonical galaxy models, a fixed pattern speed, a barred galaxy, a flocculent spiral and a tidally induced spiral. And then, for each model, they estimate the current positions of star clusters of a variety of ages, ranging from ~ 2 Myr to around 130 Myr.

Although our data only cover the most recent SF, up to 10 Myr, these ongoing star forming regions show some similarity in their spatial distribution with the wider ranging age distribution estimated by Dobbs & Pringle (2010).

M74, M100 and M51 show the expected distribution for a spiral with a fixed pattern speed and/or a bar, a monotonic sequence of ages across the spiral arms from youngest to oldest. Although M51 was modeled as a tidally induced spiral, undergoing a double interaction, and its age distribution, from ~ 2 Myr to around 130 Myr, do not show a clear trend. Rather a complex distribution, where clusters of different ages appear simultaneously in the same region. We obtain that the youngest stellar population does show the age gradients across the spiral arms, as predicted by standard density wave theory.

M63, with a peculiar somewhat bipolar east-west age distribution, seems to be also in agreement with the predictions by Dobbs & Pringle (2010). Where flocculent galaxies are expected to show individual spiral arm segments of similar age.

The age map for IC 2574 only shows local regions, like the giant northeastern HIIcomplex. Similarly for M94, the inner ring of intense active SF dominates its age map. Due to the lack of a global vision, any clue about the possible mechanism for the excitation of these galaxies could be obtained. The method we propose and develop here will be a powerful tool when applied to a larger sample with better signal to noise data sets.

For a future work we are interested in applying this technique to a larger number of galaxies, getting therefore the required Hα , FUV (GALEX) and TIR (SPITZER) images.

Moreover, thanks to the high amount of points obtained from the pixel-by-pixel technique, good statistics can be done getting our own IRX-β relationship (e.g. Heckman et al. 1995; Meurer et al. 1999). Statistical techniques applied for these purposes are simple linear and non-linear regressions between the IRX and $beta$ variables, and to discriminate among several statistical models criteria. The Akaike's Information Criterion was selected to compare between the linear and non-linear fits as the chosen model for the IRX-β relationship.

The techniques developed for this work have been long-slit spectroscopy and imaging, specifically optical tunable filter data, and ultraviolet and infrared archival images. The reduction of long-slit spectra as well as tunable filter images have been required, using the IRAF techniques for these purposes.

6.2 Conclusiones

De los estudios realizados en esta tesis se pueden derivar las siguientes conclusiones:

1. La formación estelar en el super-complejo de NGC6946 se ha propagado a partir de la formación estelar del cúmulo masivo localizado en su centro, con una velocidad estimada entre 36 y 51 km/s
2. Se ha obtenido por primera vez un modelo de la propagación de la formación estelar en este complejo
3. Se ha obtenido por primera vez el campo de velocidad del movimiento de recesión de la burbuja.
4. La mayor parte de la pared de la burbuja muestra el gas ionizado por foto-disociación, es decir por fotones ultravioletas provenientes de las estrellas masivas jóvenes. Algunas localizaciones de la pared parecen haber sido ionizadas por choques de baja velocidad producidos por los vientos estelares o explosiones de supernova.
5. Este último resultado es consistente con la dispersión de velocidad supersónica medida a lo largo de la burbuja.
6. Se ha implementado un protocolo para determinar la edad de la población estelar joven en una galaxia a partir de la emisión en H? y FUV, corregida de extinción a partir de los datos de FIR.

7. Este protocolo se ha aplicado pixel a pixel, lo que evita la necesidad de detectar y definir “a priori” las regiones de formación de la galaxia.

8. Se han diseñado y aplicado diferentes tipos de tests para evaluar la robustez y fiabilidad de la metodología.

9. La aplicación de estos tests demuestra que, aunque la calibración absoluta en edad puede depender de los modelos seleccionados, los patrones de edad encontrados permanecen inalterables.

10. Los patrones de edad obtenidos para las seis galaxias de la muestra, indican la gran diversidad de mecanismos físicos que parecen actuar en la modelización del proceso de formación estelar a gran escala.

11. La comparación de los patrones de edad obtenidos con los predichos por Dobbs Pringle (2010) para la distribución de cúmulos jóvenes nos permite conjeturar acerca de los diferentes mecanismos físicos que excitan y mantienen los brazos espirales.

12. La casuística es variada: M100, M74 y M51 muestran signos de que la formación estelar en los brazos espirales está principalmente inducida por ondas de densidad, aunque los brazos espirales externos de M74 no muestren gradientes de edad perpendiculares y toda la galaxia parezca estar afectada por un gradiente radial de edad. M94 presenta una formación estelar especialmente relevante en un anillo central de 4 kpc de diámetro y 500 pc de anchura que muestra un gradiente de edad con las estrellas más jóvenes definiendo el anillo interno. La existencia de una barra parece ser la principal responsable de esta estructura. La característica principal de M63 es un gradiente de edad que afecta a toda la galaxia yendo de Oeste a Este, mientras que la formación estelar en IC 2574 está dominada por dos regiones HII, una de la cuales con un diámetro aparente del orden de 2 kpc que ha merecido un análisis singularizado.

13. La región HII gigante coincide con una burbuja de HI en expansión. Al igual que en NGC6946 esta estructura parece haber sido originada por la formación de un cúmulo masivo en su centro hace unos 11 millones de años. La velocidad de propagación de la formación estelar se estima en 50 km/s , similar a la velocidad máxima encontrada para NGC6946.

14. Se ha analizado de forma sistemática el campo de la componente vertical de la velocidad del gas ionizado en una muestra de galaxias espirales de cara. En particular se ha estudiado la relación entre densidad del gas ionizado y amplitud de la corrugación en velocidad. De esta forma se han encontrado dos grandes grupos. En uno de ellos la velocidad y la densidad de del gas muestran una correlación desfasada por una distancia de unos pocos cientos de pc. La otra clase no parece mostrar un patrón bien definido. Estas dos clases muestran diferentes propiedades físicas del gas ionizado definidas a partir de diferentes diagramas de diagnóstico.

15. Aparte de los resultados puramente científicos, en esta tesis he obtenido también otros logros educativos y de experiencia investigadora. Me he familiarizado con diferentes técnicas de reducción de datos espectroscópicos y fotométricos. He trabajado con imágenes y datos en diferentes rangos de longitudes de onda tomadas desde archivo. He llevado adelante el liderazgo en la escritura de tres de los cuatro artículos actualmente publicados o en prensa relacionados con esta tesis. He trabajado en colaboración directa con distinto grupos internacionales durante mis estancias en Australia y , vía Internet, con otros colaboradores en Rusia y Reino Unido. He presentado contribuciones orales de mis resultados en diferentes congresos nacionales e internacionales.

Bibliography

[1] Abraham, R. G., Ellis, R. S., Fabian, A. C., Tanvir, N. R., & Glazebrook, K. 1999, MNRAS, 303, 641

[2] Akaike, H. 1974, IEEE Transactions on Automatic Control, 19, 716

[3] Alfaro, E. J., Cabrera-Cano, J., & Delgado, A. J. 1991, ApJ, 378, 106

[4] Alfaro, E. J., & Efremov, Y. N. 1996, Revista Mexicana de Astronomia y Astrofisica Conference Series, 4, 1

[5] Alfaro, E. J., Pérez, E., González Delgado, R. M., Martos, M. A., & Franco, J. 2001, ApJ, 550, 253

[6] Alfaro, E., & Elías, F. 2006, Lecture Notes and Essays in Astrophysics, vol. 2, p. 111-126., 2, 111

[7] Alfaro, E. J., García-Lorenzo, B., Efremov, Y. N., & Muñoz-Tuñón, C. 2007, Astrophysics and Cosmology After Gamow, 437

[8] Allard, E. L., Knapen, J. H., Peletier, R. F., & Sarzi, M. 2006, MNRAS, 371, 1087

[9] Arsenault, R., Boulesteix, J., Georgelin, Y., & Roy, J.-R. 1988, A&A, 200, 29

[10] Baldwin, J. A., Phillips, M. M., & Terlevich, R. 1981, PASP, 93, 5

[11] Battaglia, G., Fraternali, F., Oosterloo, T., & Sancisi, R. 2006, A&A, 447, 49

[12] Battinelli, P., Capuzzo-Dolcetta, R., Hodge, P. W., Vicari, A., & Wyder, T. K. 2000, A&A, 357, 437

[13] Beck, R. 1991, A&A, 251, 15

[14] Bekki, K., & Chiba, M. 2006, ApJL, 637, L97

[15] Benvenuti, P., Capaccioli, M., & D'Odorico, S. 1975, A&A, 41, 91

[16] Bertin, E., & Arnouts, S. 1996, A&AS, 117, 393

[17] Bertin, G., & Lin, C. C. 1996, Spiral structure in galaxies a density wave theory, Publisher: Cambridge, MA MIT Press, 1996 Physical description x, 271 p. ISBN0262023962,

[18] Blais-Ouellette, S., Carignan, C., Amram, P., & Côté, S. 1999, AJ, 118, 2123

[19] Blais-Ouellette, S., Amram, P., Carignan, C., & Swaters, R. 2004, A&A, 420, 147

[20] Bland-Hawthorn, J., & Jones, D. H. 1997, The Hubble Space Telescope and the High Redshift Universe, 121

[21] Boissier, S., et al. 2005, ApJL, 619, L83

[22] Boissier, S., et al. 2007, ApJS, 173, 524

[23] Böker, T., Laine, S., van der Marel, R. P., Sarzi, M., Rix, H.-W., Ho, L. C., & Shields, J. C. 2002, AJ, 123, 1389

[24] Boomsma, R., Oosterloo, T. A., Fraternali, F., van der Hulst, J. M., & Sancisi, R. 2005, Extra-Planar Gas, 331, 247

[25] Boomsma, R. 2007, Ph.D. Thesis,

[26] Boomsma, R., Oosterloo, T. A., Fraternali, F., van der Hulst, J. M., & Sancisi, R. 2008, A&A, 490, 555

[27] Bonnarel, F., Boulesteix, J., & Marcelin, M. 1986, A&AS, 66, 149

[28] Bonnarel, F., Boulesteix, J., Georgelin, Y. P., Lecoarer, E., Marcelin, M., Bacon, R., & Monnet, G. 1988, A&A, 189, 59

[29] Bosma, A., van der Hulst, J. M., & Sullivan, W. T., III 1977, A&A, 57, 373

[30] Bottema, R. 2003, MNRAS, 344, 358

[31] Braun, R., Oosterloo, T. A., Morganti, R., Klein, U., & Beck, R. 2007, A&A, 461, 455

[32] Buat, V., & Xu, C. 1996, A&A, 306, 61

[33] Buat, V., Donas, J., Milliard, B., & Xu, C. 1999, A&A, 352, 371

[34] Buat, V., et al. 2005, ApJL, 619, L51

[35] Bushouse, H. A., Werner, M. W., & Lamb, S. A. 1988, ApJ, 335, 74

[36] Calzetti, D., Kinney, A. L., & Storchi-Bergmann, T. 1994, ApJ, 429, 582

[37] Calzetti, D. 1997, American Institute of Physics Conference Series, 408, 403

[38] Calzetti, D., et al. 2005, ApJ, 633, 871

[39] Cannon, J. M., et al. 2005, ApJL, 630, L37

[40] Cardelli, J. A., Clayton, G. C., & Mathis, J. S. 1989, ApJ, 345, 245

[41] Cepa, J., & Beckman, J. E. 1990, ApJ, 349, 497

[42] Cerviño, M., Luridiana, V., Pérez, E., Vílchez, J. M., & Valls-Gabaud, D. 2003, A&A, 407, 177

[43] Chyży, K. T., & Buta, R. J. 2008, ApJL, 677, L17

[44] Cianci, S. 2003, Anglo-Australian Observatory Epping Newsletter, 102, 4

[45] Cid Fernandes, R., et al. 2004, ApJ, 605, 105

[46] Cid Fernandes, R., González Delgado, R. M., Storchi-Bergmann, T., Martins, L. P., & Schmitt, H. 2005, MNRAS, 356, 270

[47] Cornett, R. H., et al. 1994, ApJ, 426, 553

[48] Cortese, L., et al. 2006, ApJ, 637, 242

[49] Dale, D. A., et al. 2000, AJ, 120, 583

[50] Dale, D. A., & Helou, G. 2002, ApJ, 576, 159

[51] Dale, D. A., et al. 2007, ApJ, 655, 863

[52] Dobbs, C. L., & Pringle, J. E. 2010, MNRAS, 1391

[53] Dodorico, S. 1978, Memorie della Societa Astronomica Italiana, 49, 485

[54] Dopita, M. A. 1977, ApJS, 33, 437

[55] Dopita, M. A. 1978, ApJS, 37, 117

[56] Dopita, M. A., & Sutherland, R. S. 1996, ApJS, 102, 161

[57] Dubinski, J., Gauthier, J.-R., Widrow, L., & Nickerson, S. 2008, Astronomical Society of the Pacific Conference Series, 396, 321

[58] Dumke, A., Spiegel, M., Schmidt, R., & Neukum, G. 2008, Lunar and Planetary Institute Science Conference Abstracts, 39, 1910

[59] Edelsohn, D. J., & Elmegreen, B. G. 1997, MNRAS, 287, 947

[60] Efremov, Y. N. 1999, Astronomy Letters, 25, 100

[61] Efremov, Y. N. 2001, Astronomy Reports, 45, 769

[62] Efremov, Y. N., et al. 2002, A&A, 389, 855

[63] Efremov, Y.N., Alfaro, E., Hodge, P., Larsen, S., & Muñoz-Tuñón, C. 2004, Astronomical and Astrophysical Transactions, 23, 95

[64] Efremov, Y. N., et al. 2007, MNRAS, 382, 481

[65] Elmegreen, B. G., & Lada, C. J. 1977, ApJ, 214, 725

[66] Elmegreen, B. G., Efremov, Y. N., & Larsen, S. 2000, ApJ, 535, 748

[67] Epinat, B., et al. 2008, MNRAS, 388, 500

[68] Fathi, K., Beckman, J. E., Zurita, A., Relaño, M., Knapen, J. H., Daigle, O., Hernandez, O., & Carignan, C. 2007, A&A, 466, 905

[69] Feitzinger, J. V., & Spicker, J. 1986, PASJ, 38, 485

[70] Feldmeier, J. J., Ciardullo, R., & Jacoby, G. H. 1997, ApJ, 479, 231

[71] Ferguson, A., Wyse, R., Gallagher, J., & Hunter, D. 1995, Stellar Populations, 164, 425

[72] Ferguson, A. M. N., Wyse, R. F. G., Gallagher, J. S., & Hunter, D. A. 1998, ApJL, 506, L19

[73] Ferguson, A. M. N., Gallagher, J. S., & Wyse, R. F. G. 1998, AJ, 116, 673

[74] Florido, E., Battaner, E., Sanchez-Saavedra, M. L., Prieto, M., & Mediavilla, E. 1991, MNRAS, 251, 193

[75] Franco, J., Tenorio-Tagle, G., Bodenheimer, P., Rozyczka, M., & Mirabel, I. F. 1988, ApJ, 333, 826

[76] Franco, J., Kim, J., Alfaro, E. J., & Hong, S. S. 2002, ApJ, 570, 647

[77] Fraternali, F., Oosterloo, T. A., Sancisi, R., van Moorsel, G., & Cappi, M. 2002, Seeing Through the Dust: The Detection of HI and the Exploration of the ISM in Galaxies, 276, 419

[78] Ganda, K., et al. 2007, MNRAS, 380, 506

[79] Garcia-Burillo, S., Combes, F., & Gerin, M. 1993, A&A, 274, 148

[80] Garcia-Burillo, S., Sempere, M. J., Combes, F., & Neri, R. 1998, A&A, 333, 864

[81] Gavazzi, G., Marcelin, M., Boselli, A., Amram, P., Vílchez, J. M., Iglesias-Paramo, J., & Tarenghi, M. 2001, A&A, 377, 745

[82] Gerin, M., Casoli, F., & Combes, F. 1991, A&A, 251, 32

[83] Giovanelli, R., & Haynes, M. P. 2002, ApJL, 571, L107

[84] Glazebrook, K., Blake, C., Economou, F., Lilly, S., & Colless, M. 1999, MNRAS, 306, 843

[85] Gomez de Castro, A., & Pudritz, R. E. 1992, ApJ, 395, 501

[86] Gomez, G. C., & Cox, D. P. 2002, Disks of Galaxies: Kinematics, Dynamics and Peturbations, 275, 363

[87] Gómez, G. C., & Cox, D. P. 2004, ApJ, 615, 758

[88] Gómez, G. C., & Cox, D. P. 2004, ApJ, 615, 744

[89] González Delgado, R. M., Cid Fernandes, R., Pérez, E., Martins, L. P., Storchi-Bergmann, T., Schmitt, H., Heckman, T., & Leitherer, C. 2004, ApJ, 605, 127

[90] Gordon, K. D., Clayton, G. C., Witt, A. N., & Misselt, K. A. 2000, ApJ, 533, 236

[91] Grebel, E. K. 2000, Star Formation from the Small to the Large Scale, 445, 87

[92] . Akaike, "A new look at the statistical model identification" *IEEE Transactions on Automatic and Control*, vol.19, pp. 716-723, 1974.

[93] Heald, G. H., Rand, R. J., Benjamin, R. A., Bershady, M. A., 2006, ApJ, 647, 1018

[94] Heckman, T. M. 1980, A&A, 87, 152

[95] Heckman, T., et al. 1995, ApJ, 452, 549

[96] Ho, L. C., Filippenko, A. V., & Sargent, W

[97] Ho, L. C., Filippenko, A. V., & Sargent, W. L. W. 1997, ApJS, 112, 315

[98] Hodge, P. W. 1967, PASP, 79, 29

[99] Hummel, E., & Dettmar, R.-J. 1990, A&A, 236, 33

[100] Iglesias-Páramo, J., Boselli, A., Gavazzi, G., & Zaccardo, A. 2004, A&A, 421, 887

[101] James, P. A., & Seigar, M. S. 1999, A&A, 350, 791

[102] James, P. A., et al. 2004, A&A, 414, 23

[103] Jones, D. H., Shopbell, P. L., & Bland-Hawthorn, J. 2002, MNRAS, 329, 759

[104] Kamphuis, J., & Briggs, F. 1992, A&A, 253, 335

[105] Kamphuis, J. 1993, Star Formation, Galaxies and the Interstellar Medium, 105

[106] Karachentsev, I. D., et al. 2002, A&A, 383, 125

[107] Kennicutt, R. C., Jr. 1983, ApJ, 272, 54

[108] Kennicutt, R. C., Jr. 1998, ApJ, 498, 541

[109] Kennicutt, R. C., Jr., et al. 2003, PASP, 115, 928

[110] Kim, J., Hong, S. S., & Ryu, D. 1997, ApJ, 485, 228

[111] Knapen, J. H., Stedman, S., Bramich, D. M., Folkes, S. L., & Bradley, T. R. 2004, A&A, 426, 1135

[112] Knapen, J. H., Shlosman, I., Heller, C. H., Rand, R. J., Beckman, J. E., & Rozas, M. 2000, ApJ, 528, 219

[113] Knapen, J. H. 1998, MNRAS, 297, 255

[114] Knapen, J. H., Beckman, J. E., Heller, C. H., Shlosman, I., & de Jong, R. S. 1995, ApJ, 454, 623

[115] Knapen, J. H., Beckman, J. E., Shlosman, I., Peletier, R. F., Heller, C. H., & de Jong, R. S. 1995, ApJL, 443, L73

[116] Knapen, J. H., Beckman, J. E., Cepa, J., van der Hulst, T., & Rand, R. J. 1992, ApJL, 385, L37

[117] Knapik, J., Soida, M., Dettmar, R.-J., Beck, R., & Urbanik, M. 2000, A&A, 362, 910

[118] Kong, X., Charlot, S., Brinchmann, J., & Fall, S. M. 2004, MNRAS, 349, 769

[119] Kormendy, J., & Kennicutt, R. C., Jr. 2004, , 42, 603

[120] Kuno, N., Tosaki, T., Nakai, N., & Nishiyama, K. 1997, PASJ, 49, 275

[121] La Vigne, M. A., Vogel, S. N., & Ostriker, E. C. 2006, ApJ, 650, 818

[122] Lanyon-Foster, M. M., Conselice, C. J., & Merrifield, M. R. 2007, MNRAS, 380, 571

[123] Larsen, S. S., & Richtler, T. 1999, A&A, 345, 59

[124] Larsen, S. S., Brodie, J. P., Elmegreen, B. G., Efremov, Y. N., Hodge, P. W., & Richtler, T. 2001, ApJ, 556, 801

[125] Larsen, S. S., Efremov, Y. N., Elmegreen, B. G., Alfaro, E. J., Battinelli, P., Hodge, P. W., & Richtler, T. 2002, ApJ, 567, 896

[126] Larsen, S. S., Origlia, L., Brodie, J. P., & Gallagher, J. S. 2006, MNRAS, 368, L10

[127] Lee, J. C., et al. 2009, ApJ, 706, 599

[128] Leitherer, C., et al. 1999, ApJS, 123, 3

[129] Leitherer, C., Li, I.-H., Calzetti, D., & Heckman, T. M. 2002, ApJS, 140, 303

[130] Lelièvre, M., & Roy, J.-R. 2000, AJ, 120, 1306

[131] Lin, C. C., & Shu, F. H. 1964, ApJ, 140, 646

[132] López-Martín, L., et al. 2002, A&A, 388, 652

[133] Luo, B., Chen, J.-Y., Zhang, Z.-L., Wang, Y., Wang, J.-Y., & Xu, H.-G. 2007, Chinese Journal of Astronomy and Astrophysics, 7, 335

[134] Madau, P., Ferguson, H. C., Dickinson, M. E., Giavalisco, M., Steidel, C. C., & Fruchter, A. 1996, MNRAS, 283, 1388

[135] Malhotra, S., & Rhoads, J. E. 1995, The Formation of the Milky Way, 87

[136] Malhotra, S., et al. 2001, ApJ, 561, 766

[137] Maoz, D., Filippenko, A. V., Ho, L. C., Rix, H.-W., Bahcall, J. N., Schneider, D. P., & Macchetto, F. D. 1995, ApJ, 440, 91

[138] Martimbeau, N., Carignan, C., & Roy, J.-R. 1994, AJ, 107, 543

[139] Martin, C. L. 1997, ApJ, 491, 561

[140] Martin, M. C. 1998, A&AS, 131, 73

[141] Martin, M. C. 1998, VizieR Online Data Catalog, 413, 10073

[142] Martin, C. L., & Kennicutt, R. C., Jr. 2001, ApJ, 555, 301

[143] Martos, M. A., & Cox, D. P. 1998, ApJ, 509, 703

[144] Martos, M., Allen, C., Franco, J., & Kurtz, S. 1999, ApJL, 526, L89

[145] Maoz, D., Koratkar, A., Shields, J. C., Ho, L. C., Filippenko, A. V., & Sternberg, A. 1998, AJ, 116, 55

[146] Matthews, L. D., & Uson, J. M. 2008, ApJ, 688, 237

[147] Mazzuca, L. M., Knapen, J. H., Veilleux, S., & Regan, M. W. 2008, ApJS, 174, 337

[148] Meurer, G. R., Heckman, T. M., & Calzetti, D. 1999, ApJ, 521, 64

[149] Meurer, G. R., et al. 2009, ApJ, 695, 765

[150] Miller, B. W., & Hodge, P. 1996, ApJ, 458, 467

[151] Moellenhoff, C., Matthias, M., & Gerhard, O. E. 1995, A&A, 301, 359

[152] Moustakas, J., & Kennicutt, R. C., Jr. 2006, ApJS, 164, 81

[153] Mulder, P. S., & van Driel, W. 1993, A&A, 272, 63

[154] Mulder, P. S., & Combes, F. 1996, A&A, 313, 723

[155] Muñoz-Tuñón, C., Tenorio-Tagle, G., Castañeda, H. O., & Terlevich, R. 1996, AJ, 112, 1636

[156] Natali, G., Pedichini, F., & Righini, M. 1992, A&A, 256, 79

[157] Oke, J. B. 1990, AJ, 99, 1621

[158] Osterbrock, D. E. & G. Ferland. 2006. Astrophysics of Gaseous Nebulae and Active Galactic Nuclei, Science University Press.

[159] Pasquali, A., et al. 2008, ApJ, 687, 1004

[160] Paturel, G., Teerikorpi, P., Theureau, G., Fouqué, P., Musella, I., & Terry, J. N. 2002, A&A, 389, 19

[161] Pei, Y. C. 1992, ApJ, 395, 130

[162] Pellegrini, S., Fabbiano, G., Fiore, F., Trinchieri, G., & Antonelli, A. 2002, A&A, 383, 1

[163] Petric, A. O., & Rupen, M. P. 2007, AJ, 134, 1952

[164] Phillips, J. P., & Cuesta, L. 1999, AJ, 118, 2919

[165] Pierce, M. J. 1986, AJ, 92, 285

[166] Pilyugin, L. S., Vílchez, J. M., & Contini, T. 2004, A&A, 425, 849

[167] Pogge, R. W. 1989, ApJS, 71, 433

[168] Riesgo, H., & López, J. A. 2006, Revista Mexicana de Astronomia y Astrofisica, 42, 47

[169] Rozas, M., Zurita, A., Heller, C. H., & Beckman, J. E. 1999, A&AS, 135, 145

[170] Rozas, M., Zurita, A., Cardwell, A., & Beckman, J. E. 2000, Cosmic Evolution and Galaxy Formation: Structure, Interactions, and Feedback, 215, 230

[171] Rozas, M., Zurita, A., & Beckman, J. E. 2000, A&A, 354, 823

[172] Ryder, S. D., & Knapen, J. H. 1999, MNRAS, 302, L7

[173] Ryder, S. D., Knapen, J. H., & Takamiya, M. 2001, MNRAS, 323, 663

[174] Sabbadin, F., Minello, S., & Bianchini, A. 1977, A&A, 60, 147

[175] Salo, H., & Laurikainen, E. 1999, , 269, 663

[176] Sánchez Gil, M. C., Alfaro, E. J., & Pérez, E. 2009, ApJ, 702, 141

[177] Sandage, A. 1961, Washington: Carnegie Institution, 1961,

[178] Sandage, A., & Tammann, G. A. 1974, ApJ, 194, 559

[179] Sandage, A., & Bedke, J. 1994, The Carnegie Atlas of Galaxies. Volumes I, II., by Sandage, A.; Bedke, J.. Carnegie Institution of Washington Publ., No. 638,,

[180] Sanders, D. B., Mazzarella, J. M., Kim, D.-C., Surace, J. A., & Soifer, B. T. 2003, AJ, 126, 1607

[181] Santillán, A., Franco, J., Martos, M., & Kim, J. 1999, ApJ, 515, 657

[182] Santillán, A., Kim, J., Franco, J., Martos, M., Hong, S. S., & Ryu, D. 2000, ApJ, 545, 353

[183] Scheepmaker, R. A., Lamers, H. J. G. L. M., Anders, P., & Larsen, S. S. 2009, A&A, 494, 81

[184] Schinnerer, E., Eckart, A., Tacconi, L. J., Genzel, R., & Downes, D. 2000, ApJ, 533, 850

[185] Schlegel, D. J., Finkbeiner, D. P., & Davis, M. 1998, ApJ, 500, 525

[186] Scoville, N. Z., Polletta, M., Ewald, S., Stolovy, S. R., Thompson, R., & Rieke, M. 2001, AJ, 122, 3017

[187] Seigar, M. S. 2002, A&A, 393, 499

[188] Sellwood, J. A., & Carlberg, R. G. 1984, ApJ, 282, 61

[189] Shlosman, I., Frank, J., & Begelman, M. C. 1989, , 338, 45

[190] Sofue, Y. 1997, PASJ, 49, 17

[191] Sofue, Y., Tutui, Y., Honma, M., Tomita, A., Takamiya, T., Koda, J., & Takeda, Y. 1999, ApJ, 523, 136

[192] Stecher, T. P., et al. 1992, ApJL, 395, L1

[193] Stecher, T. P., et al. 1997, PASP, 109, 584

[194] Swaters, R. A., Sancisi, R., & van der Hulst, J. M. 1997, ApJ, 491, 140

[195] Swaters, R. 1999, Galaxy Dynamics - A Rutgers Symposium, 182, 369

[196] Tenorio-Tagle, G., Silich, S., Rodríguez-González, A., & Muñoz-Tuñón, C. 2005, ApJ, 620, 217

[197] Thornley, M. D., & Mundy, L. G. 1997, ApJ, 484, 202

[198] Tonry, J. L., Dressler, A., Blakeslee, J. P., Ajhar, E. A., Fletcher, A. B., Luppino, G. A., Metzger, M. R., & Moore, C. B. 2001, ApJ, 546, 681

[199] Toomre, A. 1964, ApJ, 139, 1217

[200] Trujillo, I., Martinez-Valpuesta, I., Martínez-Delgado, D., Peñarrubia, J., Gabany, R. J., & Pohlen, M. 2009, ApJ, 704, 618

[201] Tosaki, T., Shioya, Y., Kuno, N., Nakanishi, K., & Hasegawa, T. 2003, PASJ, 55, 605

[202] Tully, R. B. 1988, Cambridge and New York, Cambridge University Press, 1988, 221 p.,

[203] Turner, J. L., & Ho, P. T. P. 1994, ApJ, 421, 122

[204] Tzanavaris, P., & Georgantopoulos, I. 2007, A&A, 468, 129

[205] van den Bosch, F. C., Robertson, B. E., Dalcanton, J. J., & de Blok, W. J. G. 2000, AJ, 119, 1579

[206] Vázquez, G. A., & Leitherer, C. 2005, ApJ, 621, 695

[207] Veilleux, S., & Osterbrock, D. E. 1987, ApJS, 63, 295

[208] Vogel, S. N., Rand, R. J., Gruendl, R. A., & Teuben, P. J. 1993, PASP, 105, 666

[209] Wakker, B. P., & Adler, D. S. 1995, AJ, 109, 134

[210] Walborn, N. R., & Parker, J. W. 1992, ApJL, 399, L87

[211] Waller, W. H., et al. 2001, AJ, 121, 1395

[212] Walter, F., Kerp, J., Duric, N., Brinks, E., & Klein, U. 1998, ApJL, 502, L143

[213] Walter, F., & Brinks, E. 1999, AJ, 118, 273

[214] Weinberg, M. D. 1991, ApJ, 373, 391

[215] Weisz, D. R., Skillman, E. D., Cannon, J. M., Walter, F., Brinks, E., Ott, J., & Dolphin, A. E. 2009, ApJL, 691, L59

[216] Wong, T., & Blitz, L. 2000, ApJ, 540, 771

[217] Weliachew, L., Sancisi, R., & Guelin, M. 1978, A&A, 65, 37

[218] Zimmer, P., Rand, R. J., & McGraw, J. T. 2004, ApJ, 607, 285 w

[219] Zurita, A., Cardwell, A., Beckman, J. E., & Rozas, M. 2001, Galaxy Disks and Disk Galaxies, 230, 335